Superconducting Tunnel Junctions as Single Photon X-Ray Detectors

A Dissertation
Presented to the Faculty of the Graduate School
of
Yale University
in candidacy for the degree of
Doctor of Philosophy

by
Michael Christopher Gaidis
November 1994

ABSTRACT

Superconducting Tunnel Junctions as Single Photon X-Ray Detectors

Michael Christopher Gaidis
Yale University
1994

Compared with existing semiconducting *p-n* junction x-ray detectors, superconducting tunnel junctions offer superior energy resolution in the detection of single photons. Such superconducting detectors are desirable for x-ray astronomy applications, where the photon flux is low and high energy resolution is required. Progress is reported on the development of Nb-Ta-Al-AlOx-Al tunnel junction structures for the observation of celestial x-ray sources. These devices use superconductor "bandgap engineering" for quasiparticle trapping to enhance performance. Experimental results at 0.3 K are presented, showing energy resolution better than 200 eV full-width-half-maximum for 6 keV x-rays. The absorption efficiency of these devices is better than 25%, with active areas of $\approx$ 100 µm x 100 µm. The devices are designed to easily scale to larger areas and absorption efficiencies. Significant improvement in the device energy resolution appears possible with only minor modifications.

Acknowledgements

My accomplishments at Yale in the last five years would be far fewer if it were not for the aid and guidance of my colleagues. I would like to thank here those who were instumental in the completion of this thesis.

My principal advisor, Dan Prober, made my education at Yale everything I could have hoped for. His unique style and deep phenomenological understanding of solid state physics never ceases to impress me. Personal discussions with Dan always taught me something, whether it be physics, or how best to interact with people. I will continue to use Dan as a role model in my future endeavors.

I am also appreciative of my other advisory committee members: Bob Wheeler, Vic Henrich, and Pete Kindlmann. I believe my many fruitful discussions with each of these professors helped me in the way that the advisory committee was originally intended to. Our collaborators at NASA, Andy Szymkowiak and Harvey Moseley, were indispensible to me. Without their knowledge, experience, and advice, I would not have a Chapter 7.

The graduate students at Yale formed the basis of a good deal of my education. I would particularly like to thank Hodge Worsham and Rich Steinberg for their generous contribution of time and wisdom. Stephan Friedrich has also taught me much, and forced me to slow down and take a look within. I have enjoyed many discussions (arguments) with him, and believe he will form a good match with Ken Segall in the continuation of this project.

I would also like to thank the support staff: Jim, Curt, Oded, Dag, Mark, Anurag, Stanley, and George, for keeping me (in)sane as I tried to get the *&^$#% equipment to work. Pat Brodka and Jayne Miller were always helpful, and a refreshing break from all of the intense science on the 4th floor of Becton. I must also thank the State of Connecticut, NASA GSFC, and AT&T for their monetary support. Without this aid, graduate student life would have been miserable.

Most importantly, I would like to thank my family. Without my parents' example, love, and support, I would not be here today. My in-laws were always quick to lift my spirits, and I am glad to be able to call them a part of my family. Erin

has been a tremendous source of happiness for me in the last two years. She always gives me a smile, and immediately makes me forget any troubles at work. Perhaps this thesis will inspire her to reach high for her goals -- and succeed. My wife Denise has always been a source of strength and vision for me. As much effort as I put into this thesis, my life would be empty without her. I would like to thank Denise for her love, devotion, and friendship. This thesis is dedicated to her.

Table of Contents

Acknowledgements ii
List of Symbols and Abbriviations vii

1. Introduction & Motivation 1
2. SIS Tunnel Junction Detectors: An Overview 5
    - 2.1 SIS Junction Response to X-Ray Absorption 5
    - 2.2 Important Processes in STJ Detectors 7
        - 2.2.1 Quasiparticle Generation Region 8
        - 2.2.2 Quasiparticle Recombination 11
        - 2.2.3 Phonon Trapping 16
        - 2.2.4 Quasiparticle Tunneling 18
        - 2.2.5 Quasiparticle Outdiffusion 20
        - 2.2.6 Quasiparticle Backtunneling 23
        - 2.2.7 Quasiparticle Outdiffusion (from the Counterelectrode) 24
    - 2.3 Discussion 25
3. Superconductor Bandgap Engineering 26
    - 3.1 Device Requirements 26
    - 3.2 Quasiparticle Trapping 28
    - 3.3 The Absorber – Trap Interface 32
        - 3.3.1 Proximity Effect 32
        - 3.3.2 Poor Quality Interfaces 36
    - 3.4 Increased Signal Due to Bandgap Engineering 37
        - 3.4.1 Ta Subgap Phonons 38
        - 3.4.2 Multiplication upon Trapping 40
    - 3.5 Discussion 42
4. Electronic Circuitry 44
    - 4.1 Charge Preamplifier 45
        - 4.1.1 Charge Amplifier Signal Response 46
        - 4.1.2 Electronic Noise in the Charge Amplifier 54
        - 4.1.3 Stability of the Charge Amplifier 56
    - 4.2 DC Junction Biasing 57
        - 4.2.1 Applied Magnetic Fields 58

4.2.2 Tunnel Junction Shaping 59
4.2.3 Fiske Modes..61
4.3 Discussion 63
5. Device Design and Fabrication..64
5.1 The Substrate 65
5.2 The X-Ray Absorber 69
5.2.1 BCC Ta Film Growth..69
5.2.2 Stress Minimization and Columnar Growth..71
5.3 Absorber Wiring 73
5.4 The Tunnel Junction Region..74
5.4.1 The Tunnel Barrier 74
5.4.2 The Trap 76
5.4.3 The Counterelectrode..77
5.4.4 The SiO Passivation..78
5.4.5 The Al Wiring..78
5.5 Discussion 79
6. DC Device Characterization 80
6.1 Interface Characterization 80
6.2 Magnetic Field Suppression of Pair Currents..83
6.3 DC Junction Current–Voltage Characteristics 87
6.4 Discussion 91
7. X-Ray Detection..92
7.1 Cryogenic Testing..92
7.2 Pulse Shapes..93
7.3 X-Ray Energy Spectra..96
7.4 X-Ray Energy Spectra with Trap Masking 100
7.5 Substrate Absorptions 104
7.6 Extended Trap Devices 106
7.7 Investigation of Backtunneling 110
7.8 Discussion 116
8. Computer Simulations of Junction Response 120
8.1 The Equations of State..120
8.2 Comparison with Experimental Pulses 121
8.3 Quasiparticles and Phonons in the STJ Detector 122
8.4 Effects of Amplifier Electronics 124
8.5 Discussion 126

9. Conclusion 127
9.1 Comparison with Other Work 127
9.2 Suggestions for Future Work 130
Appendix 1: Device Fabrication Procedure 133
A1.1 Wafer Preparation 133
A1.2 Tantalum Absorber Deposition and Definition 133
A1.3 Niobium Contact Deposition and Definition 134
A1.4 Aluminum Trilayer Deposition 135
A1.5 Aluminum Trilayer Patterning 135
A1.6 SiO Deposition and Patterning 136
A1.7 Aluminum Wiring Deposition and Patterning 136
Appendix 2: Summary of Device Characteristics 138
A2.1 X-C93 138
A2.2 X-N93 139
A2.3 X-D94 140
References 141

List of Symbols and Abbreviations

α	Phonon transmission coefficient between two materials
a	Series input noise power in charge amplifier
A	Superconducting film area, and DC open loop gain of op-amp
A_{OL}	Frequency–dependent open loop gain of op-amp
β-Ta	The tetragonal phase of tantalum
b	Parallel input noise power in charge amplifier
B	Noise bandwidth of charge amplifier, also magnetic field
BCS	Bardeen-Cooper-Scrieffer [Bardeen, 57] superconductivity theory
c_s	Average phonon velocity
C_{block}	DC blocking capacitance in charge amplifier
C_f	Feedback capacitance in charge amplifier
C_f^*	Effective feedback capacitance in charge amplifier
C_{FET}	Input capacitance of charge amplifier input stage FET
C_{jn}	Input capacitance in charge amplifier (includes junction, wiring, FET)
Δ	Superconducting energy gap
$\Delta(0)$	Superconducting energy gap at zero temperature
d	Superconductor film thickness
D	Diffusion constant for quasiparticle transport
DC	Very low frequency (< 1 Hz)
ε	Average x-ray energy per single charge created
e	Elementary charge (=+1.6 x 10^{-19} C)
e_n	Series input noise voltage in charge amplifier
E_{FWHM}	Full width at half maximum of a spectral line (= Energy resolution)
E_{qp}	Energy of quasiparticle (= Δ at the gap edge)
E_x	Energy of incident x-ray
EMI	Electro-magnetic interference
F	Fano factor
$f(E_{qp})$	Fermi function for quasiparticle energy E_{qp}
γ	Phonon loss rate from superconductors by decay or to the substrate
Γ_r	Quasiparticle loss rate due to recombination
$\Gamma_{r,self}$	Quasiparticle loss rate due to self recombination (among N_x only)
$\Gamma_{r,thermal}$	Quasiparticle loss rate due to thermal background recombination
g_m	Transconductance of charge amplifier input stage FET

h	Planck's constant
I	Current through the tunnel junction
I_{bias}	DC bias current of the tunnel junction
I_c	Junction critical current at zero voltage
I_{co}	Junction critical current at zero voltage and zero magnetic field
I_{cB}	Junction critical current at zero voltage and finite magnetic field, B
I_{Cf}	Current through the charge amplifier's feedback capacitance
I_{in}	Current entering the charge amplifier's feedback loop
I_{jn}	Total current through the tunnel junction
I_{Rf}	Current through the charge amplifier's feedback resistance
I_x	Current produced in tunnel junction by an x-ray absorption
J_c	Junction critical current density
k	Quasiparticle wavevector
k_B	Boltzmann's constant
Λ	Phonon mean free path against pair breaking
l	Quasiparticle mean free path
L	Junction length, as presented to the magnetic field
L_D	Diffusion length of quasiparticles
n	Density of quasiparticles
n_{th}	Density of quasiparticles due solely to thermal generation
N	Number of quasiparticles
N_{abs}	Number of x-ray produced quasiparticles in the absorber
$N(E_{qp})$	Quasiparticle density of states for quasiparticle energy E_{qp}
N_o	Single spin density of states for electrons at the Fermi level
N_{tr}, N_{trap}	Number of x-ray produced quasiparticles in the trap
$N_{\Omega tr}$	Number of $> 2\Delta_{tr}$ phonons in the trap
N_x	Number of quasiparticles produced by the incident x-ray
NIS	Normal metal–insulator–superconductor
q	Charge of quasiparticle, taken as -1.6×10^{-19} C
Q	Charge on the feedback capacitor
qp	Quasiparticle
Q_x	Total charge delivered to charge amplifier due to an incident x-ray
ρ	Material density
R	Recombination rate per unit density of quasiparticles
R_{dyn}	Tunnel junction dynamic resistance at DC bias point
R_f	Feedback resistance in charge amplifier

R_f^*	Effective feedback resistance in charge amplifier
R_{nn}	Junction resistance for bias voltages much larger than 2Δ
R_{pe}	Range of primary photoelectron
RIE	Reactive ion etching
RRR	Residual resistance ratio of a film ($\approx R_{300K} / R_{10K}$)
s	Complex frequency used in Laplace transform ($= j\omega$)
S1	Absorber film
S2	Trap film
S3	Absorber wiring film
SIS	Superconductor–insulator–superconductor
STJ	Superconducting tunnel junction
τ_{bt}	Characteristic time to backtunnel
τ_E	Decay time of x-ray induced integrated charge pulse
τ_{esc}	Phonon escape time from the trap
τ_f^*	Effective electronic charge pulse decay time ($= R_f^* C_f^*$)
τ_{fall}	Decay time of x-ray induced current pulse
τ_l	Quasiparticle loss time due to recombination and outdiffusion
τ_{loss}	Quasiparticle loss time from trap, due to tunneling and recombination
τ_{loss}^*	Adjusted quasiparticle loss time from the trap
τ_o	Characteristic time describing strength of electron-phonon coupling
τ_{pb}	Phonon pair-breaking time
τ_r	Quasiparticle recombination time
τ_r^*	Quasiparticle recombination time lengthened by phonon trapping
τ_{rise}	Risetime of x-ray induced current pulse
τ_{rise}^{amp}	Charge amplifier intrinsic risetime
τ_{ro}	Quasiparticle recombination time with no external perturbations
τ_{rt}	Characteristic time to reverse tunnel
τ_s	Quasiparticle scattering time to emit a phonon
τ_t	Tunneling time
τ_{trap}	Quasiparticle trapping time
τ_{trap}^*	Adjusted quasiparticle trapping time
θ_D	Debye temperature
t	Time
t_{max}	Time at which the x-ray induced current pulse is a maximum
T	Temperature
T_c	Superconducting critical temperature

T_{dep}	Film deposition temperature
T_m	Melting temperature
UHV	Ultra high vacuum (< 10^{-9} torr)
v	Quasiparticle velocity
v_F	Fermi velocity (for electrons)
V	Volume of superconducting film; also voltage across tunnel junction
V^-	Voltage at op-amp inverting terminal
V_{abs}	Volume of absorber film in the STJ detector
V_{bias}	DC bias voltage across the tunnel junction
V_n	Charge amplifier output voltage noise (rms)
V_{out}	Charge amplifier output voltage
V_{trap}	Volume of trap film in the STJ detector
ω	Angular frequency of electronic signal ($= 2\pi f$)
ω_o	Break frequency of op-amp open loop gain
w	Width of junction wiring lead
Ω	Phonon energy
ξ	Superconducting coherence length
Z_f	Charge amplifier feedback impedance
Z_{jn}	Junction effective impedance
Z_p	Effective impedance seen from charge amplifier inverting terminal

1. Introduction & Motivation

Many areas of research in physics rely on the detection of single particles or photons. The introduction of improved detectors frequently leads to exciting discoveries. This thesis describes one of a new breed of low temperature detectors. These new detectors rely on the collection of either phonons or superconducting quasiparticles produced by incident particles. Because of the very small excitation energies possible in the phonon and quasiparticle systems, great sensitivities can be achieved.

Improvement of existing single particle detectors will have *immediate* application in the fields of astrophysics, nuclear physics, and particle physics. Long term development could lead to profitable applications in industry or biomedical imaging.[Sadoulet, 88; Fiorini, 91] Table 1 provides a sampling of the vast global effort in developing such improved detectors. A large number of related conference proceedings is available, describing many of these, and other projects as well.[Barone, 88; Waysand, 89; Barone, 90; Brogiato, 90; Booth, 92; Labov, 93] Note that most of the work in this field has been performed within the last ten years; this is truly a fresh, exciting area of research.

The focus of the present work is the fabrication of x-ray detectors for astronomy in the 100 eV to 10 keV range, with quantum (single-photon) efficiencies and with energy resolution $\Delta E_X/E_X$ of better than 1%. Such improved detectors could be useful to x-ray astronomers for several reasons:

- Abundant elements emit K-shell x-rays from 100 eV to 10 keV
- Hot plasmas ($10^6 - 10^7$ K) emit x-rays with information on the temperature, density, and elemental abundance in the gas
- High energy resolution allows determination of source velocity structure
- High efficiency allows observation of faint celestial sources.

Existing "conventional" x-ray detectors either have insufficient energy resolution (*e.g.*, semiconductor *p-n* junctions), or are impractical for use with low particle flux (*e.g.*, dispersive detectors). X-ray astronomy, as well as each of the applications covered in Table 1, requires two qualities in a detector: single particle efficiency, and exceptional energy resolution.

Application	Institution	Reference
Astrophysics		
0.1–10 keV X-Ray Detection	NASA GSFC, Wisc.	Moseley, 88
	TUM	Kraus, 89a
	Livermore	Mears, 93
	ESA	Rando, 92
	SRON, Twente	le Grand, 93
	NRL	Zacher, 93
Dark Matter or WIMPS	LBL, UCB	Sadoulet, 88
	Oxford	Gaitskell, 93
	MPI	Seidel, 93
Solar Neutrinos, Standard Solar Model	TUM – MPI	Kraus, 89a
	Oxford	Booth, 89
Particle Physics		
Coherent Neutrino Scattering	Stanford	Young, 91
Neutrinoless Double Beta Decay	Zaragoza	Larrea, 89
	Milano	Alessandrello, 93
Neutrino Mass Measurements	Swiss Inst. of Tech.	Twerenbold, 86
Compton Scattering in Solids	Stanford	Stahle, 91
Applied Uses		
Materials Analysis	Grumman	Lesyna, 93
Steel Industry, Materials	Nippon Steel	Kurakado, 92

Table 1: Some representative physics applications for improved particle detectors.

The largest class of x-ray detectors consists of ionized–particle detectors. These measure the ionization produced by an x-ray in the absorbing medium. In such detectors, quantum efficiency is readily achievable, but good energy resolution is not. The mean number of ionized charges produced in a detector is commonly written as $N_x = E_x/\varepsilon$, where E_x is the deposited x-ray energy, and ε is the minimal ionizing energy required to release a single charge. Ionization detectors use N_x as a measure of incident particle energy. Fluctuations of N_x obey a Poisson distribution, thus imposing a fundamental limit on the ultimate energy resolution of such detectors.[Klein, 68] A useful measure of energy resolution is E_{FWHM}, the full width at half maximum of a pulseheight spectrum line, given approximately by

$$E_{FWHM} = 2.35\sqrt{E_x F \varepsilon} \ .$$

Here, the Fano factor F is a measure of the degree of anticorrelation among ionizing events ($0 < F \leq 1$),[Fano, 47] and has been estimated as ≈ 0.2 in superconducting x-ray detectors.[Kurakado, 82]

Our approach to x-ray detection involves counting the number of quasiparticles produced in a superconductor by an absorbed x-ray. Figure 1 outlines the basic detection process with a schematic of our device. An incoming x-ray is absorbed by a thick layer of tantalum. A large fraction of the x-ray energy is converted into quasiparticles, which then pass into an aluminum quasiparticle trap, and eventually tunnel through a thin aluminum oxide barrier. It is these quasiparticles that are collected by our preamplifier to give a measure of the incident x-ray energy. The various processes involved are discussed in detail in Chapters 2, 3, and 4.

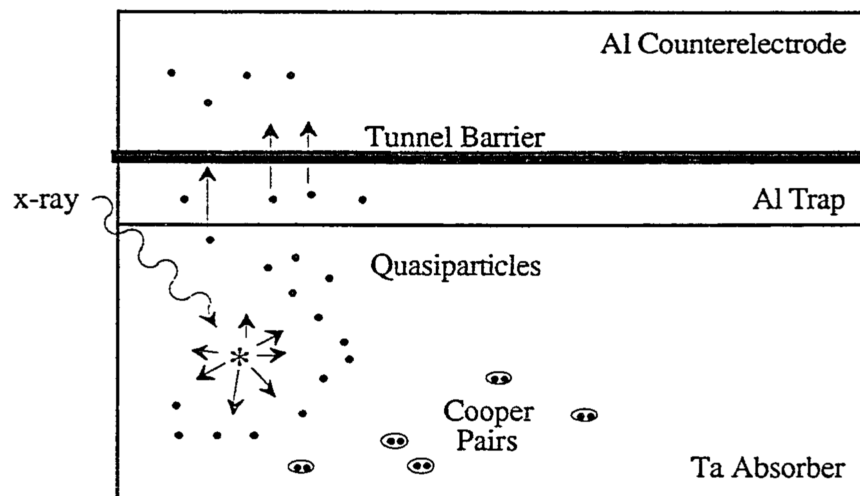

Figure 1: X-ray detection with our superconducting tunnel junction device.

Equation 1 reveals the benefit offered by superconducting tunnel junction (STJ) detectors over semiconducting *p-n* junction detectors. The minimal ionizing energy ε is of order 1 eV in semiconductors (from electron–hole pair breaking), but is of order 1 meV in conventional low temperature superconductors (from Cooper pair breaking). With adequate charge collection and low noise amplifiers, this translates directly to a factor of $\approx$ 30 better energy resolution. A 1 keV x-ray could be detected with $\approx$ 3 eV resolution in a STJ instead of $\approx$ 90 eV resolution presented by the best *p-n* junction detectors. This potential for improved energy resolution with single photon efficiency was the stimulus for the work described in this thesis. The utilization of superconducting particle detectors is in its infancy, and therefore presents some difficult challenges. This work necessarily encompassed all aspects of successful detector demonstration: theory and design of the detector, design of bias and amplifier electronics, device fabrication, and cryogenic testing. These topics are presented below, in this order.

2. SIS Tunnel Junction Detectors: An Overview

2.1 SIS Junction Response to X-Ray Absorption

In a superconducting film, the production of photoelectrons, electron–electron interactions, and electron–phonon interactions are the important processes involved shortly after an x-ray absorption event. These processes convert absorbed x-ray energy into quasiparticles and phonons with energies of a few meV in times of order picoseconds.[Twerenbold, 86b] Further relaxation in a few nanoseconds results in phonons of energy less than twice the gap energy ($\Omega < 2\Delta$) and quasiparticle excitations within a few hundred μeV of the gap edge.[Kaplan, 76] It is these quasiparticles which are detected as an excess current through a tunnel junction, the number of detected quasiparticles giving a measure of the absorbed x-ray energy. Immediately after the relaxation process, approximately 60% of the incident energy resides in the desired charged particle (quasiparticle) system, while 40% is lost in phonons of insufficient energy to break Cooper pairs.[Kurakado, 82] This is a significantly better ratio than in semiconductor detectors, mainly because Debye energies lie between superconductor and semiconductor gap energies. Typical Debye energies are of order 10 meV, about an order of magnitude larger than superconductor gap energies, and two orders of magnitude smaller than useful semiconductor gap energies. This implies that phonon production in a conventional semiconductor ionization detector forever removes that phonon's energy from the detectable charge system, while in a superconductor this is not necessarily the case. Phonons can rapidly generate quasiparticles, provided $\Omega > 2\Delta$. This process makes superconductors approximately twice as effective as semiconductors in converting x-ray energy into charge carriers.[Kurakado, 82] Another interesting consequence of quasiparticle generation by phonons is that STJs can be effective detectors of either ionizing *or* non-ionizing particles (i.e., particles which produce only phonons) – in both cases employing quasiparticle tunneling. This makes STJs potentially useful for exotic particle detection, with much better energy resolution than proven detector schemes.

For readers not familiar with basic superconductor–insulator–superconductor (SIS) tunneling theory, the treatments by Matisoo [69], Gray [81], or Van Duzer [81] cover the important aspects which are not part of this thesis. Simply stated, the current through a tunnel junction is

$$I = \frac{qN}{\tau_t} ,$$

where N is the number of charge carriers which can tunnel, q is the charge of an electron (-1.6×10^{-19} C), and $1/\tau_t$ is the tunneling probability (per unit time). The tunnel time, τ_t, is a measure of the tunnel barrier's opacity. N_X excess quasiparticles generated by an x-ray in a STJ detector result in an increase of current, and the integral of this current (*i.e.*, the created charge) gives a measure of the x-ray energy. The increase in N can be treated as simple heating of the film by the absorbed x-ray energy, in a time of order nanoseconds. A family of current–voltage (I–V) traces for a SIS tunnel junction at several temperatures is shown in Figure 2.1. The behavior of the device upon absorption of an x-ray can be inferred from such traces. *(Note that this and following discussions often include calculations specific to certain materials such as aluminum or tantalum. These materials are chosen as particularly relevent to the devices fabricated in this work, as will be explained in Chapters 3 and 5.)*

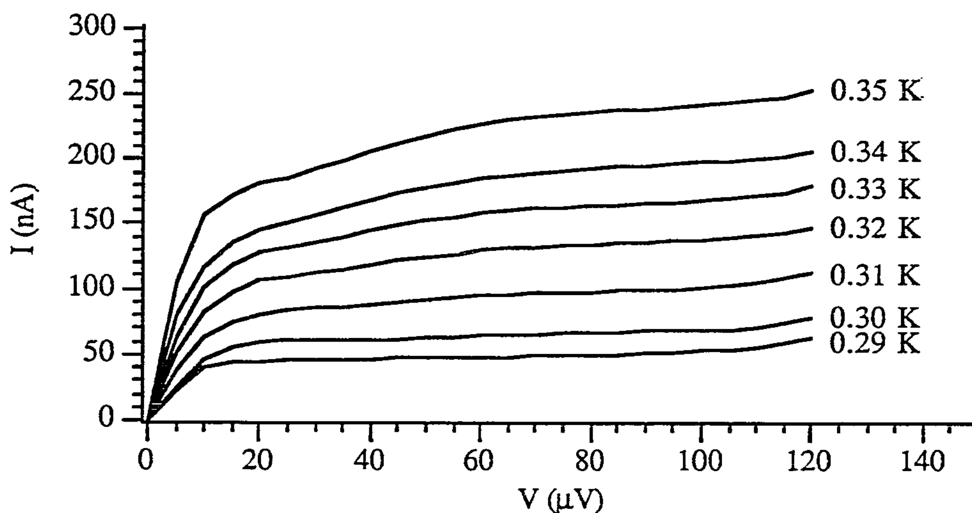

Figure 2.1: Current–voltage trace of the region V « 2Δ for an Al–Al Oxide–Al STJ at different temperatures.

As seen above, the basic operation of these devices does not appear excessively difficult, but there are several factors which serve to degrade their performance. These factors must be evaluated and minimized to obtain energy resolution reasonably close to that predicted by the discussion in Chapter 1.

2.2 Important Processes in STJ Detectors

The discussion in Chapter 1 gives the energy resolution as proportional to the square root of the minimal ionizing energy ε. A naive estimate for ε in a superconductor is just Δ, the superconductor's gap energy. Due to incomplete conversion of the x-ray energy into collectable charges, STJ detectors will give ε values somewhat higher than Δ. There are detector designs incorporating quasiparticle multiplication and backtunneling (see below) which give gain in the detector itself, and effectively smaller values of ε. However, the statistics governing ultimate energy resolution depend solely on the *initial* creation of quasiparticles in the x-ray absorbing film. Thus, for purposes of determining energy resolution, ε can never be less than Δ. Several factors influence how large ε will be:

- the recombination (loss) of quasiparticles back into Cooper pairs
- the diffusion (loss) of quasiparticles away from the junction area
- phonon behavior (possible loss from the film, decay, or trapping of $\Omega > 2\Delta$ phonons; and the loss of $\Omega < 2\Delta$ phonons).

Figure 2.2a schematically outlines these processes along with the tunneling processes which play an important role in determining the relative magnitude of the above effects. Each of these processes are discussed in detail immediately below.

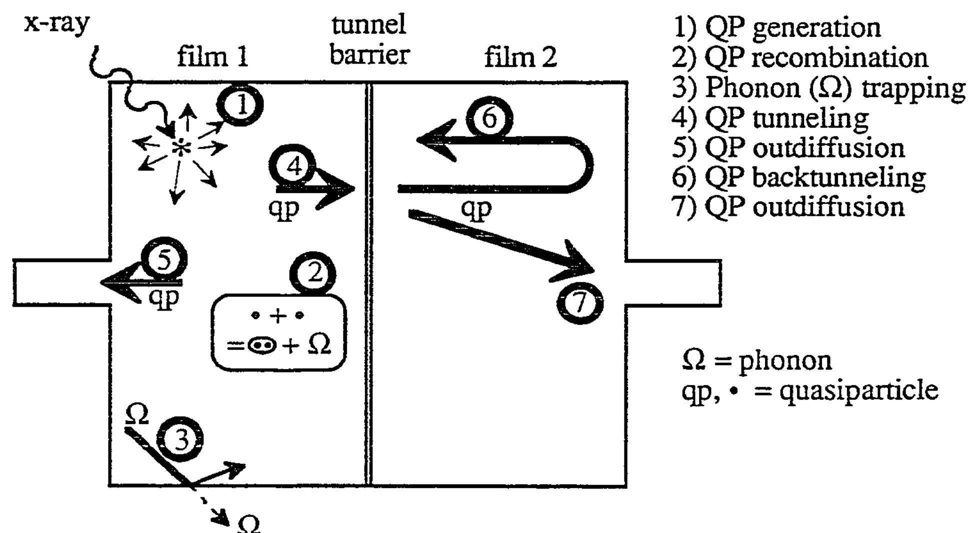

Figure 2.2a: Important processes in a simple STJ detector; see discussion in text.

2.2.1 Quasiparticle Generation Region

An incoming x-ray will typically produce one or more photoelectrons in the superconducting film. As a photoelectron travels through the film, it generates high energy electrons concentrated near the path of the photoelectron. It is important to understand the nature of this highly nonequilibrium "hot spot" region, particularly how the energy diffuses away to dissipate the hot spot. In certain cases, the high energy density of the hot spot can significantly weaken the superconductivity of the region, leading to bandgap suppression. Quasiparticles can be trapped in the potential well of the lower bandgap region – eventually recombining, rather than tunneling. Their energy is lost, thus increasing ε.

The nature of this process is sufficiently complicated that quantitative results are very difficult to obtain. Qualitative considerations, however, can lead to some valuable insight. The severity of the situation can be appreciated if one compares the energy density due to the absorption of an x-ray with the condensation energy density of the superconducting pairs at the bath temperature ($\approx 2 \times 10^4$ eV/μm^3 in Ta).[Van Vechten, 91] To determine the volume in which the x-ray deposits its full energy, we begin with the range of the primary photoelectron produced by an x-ray in Ta. Using the experimental relation [Van Vechten, 91]

$$R_{pe}(E_X) = \frac{3.52}{\rho}\left[\frac{E_X}{10\ \mathrm{keV}}\right]^{1.75},$$

with ρ the density of the material in g/cm^3, and E_X the x-ray energy, we find a photoelectron range $R_{pe} \approx 0.1$ μm in Ta for the absorption of a 6 keV x-ray. Based on femtosecond laser pulse relaxation experiments in metals, we can assume that within picoseconds, the photoelectron energy has been distributed among many electrons near the Debye energy.[Schoenlein, 87] Because high energy electrons scatter very rapidly [Kaplan, 76; Santhanam, 84], we can assume they travel no farther than 0.1 μm in a few picoseconds. We thus have a representative volume of (0.1 μm)^3 over which the x-ray energy is distributed as $\approx$ Debye energy electrons and phonons. The energy density for a 6 keV x-ray is thus $\geq 6 \times 10^6$ eV/μm^3. This calculation implies the possible destruction of superconductivity in the absorption region.

Although the deposited energy density is likely more than two orders of magnitude larger than the superconducting condensation energy density, the devices will still be operable if the x-ray energy can be dissipated from the region before the superconductor reacts to the perturbation. In a worst-case scenario, the absorption region can turn normal, inducing self-trapping of the generated quasiparticles in the

region's potential well. This, however, is not generally the expected situation. High energy quasiparticles (E_{qp} > a few Δ) do not exhibit a strong effect on the actual value of the superconducting energy gap. This is apparent from the self-consistent BCS energy gap equation [Gray, 81]:

$$\ln\left(\frac{\Delta(0)}{\Delta}\right) = \int_0^{\infty} dE_{qp} \; \frac{N(E_{qp})\, f(E_{qp})}{E_{qp}}$$

where $\Delta(0)$ is the zero temperature energy gap, $f(E_{qp})$ is the fermi distribution, and

$$N(E_{qp}) = \mathrm{Re}\left\{ E_{qp} \Big/ \sqrt{E_{qp}^2 - \Delta^2} \right\}$$

is the quasiparticle density of states.[Bardeen, 57] Thus, any possibility of significant gap reduction comes during the expansion (relaxation) of quasiparticles of energy near Δ. (Note that the energy gap equation is strictly valid only for equilibrium situations, but it is believed to give qualitatively correct results also for steady-state non-equilibrium situations, or those which vary on a time scale slower than h/Δ.)

Significant gap reduction occurs if there is a large density of quasiparticles at low energy. The best STJ detectors will utilize films which spatially disperse the energy from the absorption region quickly – such that the quasiparticles will be sufficiently dilute before they scatter to low energy. The extent of the spatial dispersion of the energy is determined by the interaction between the quasiparticle and phonon systems. For reasonably clean films, quasiparticles will have a much higher effective velocity than phonons, and will thus spread out the energy more effectively. For a typical clean tantalum film in this work, the quasiparticle diffusion constant is D $\approx$ 500 cm^2/sec. In 100 psec, quasiparticles in tantalum will diffuse $\approx \sqrt{500 \times 10^{-10}}$ cm $\approx$ 2 μm, giving a volume of about 35 μm^3. Note that for quasiparticle-dominated energy dispersing, cleaner films with higher D will be more effective in diluting the hotspot. Typical phonons in tantalum travel at 2 x 10^5 cm/s [Kaplan, 79], enclosing a volume of $\approx$ 0.035 μm^3 in 100 psec. (That 100 psec is a relevant number will become apparent below.) Therefore, it is important to keep the energy in the quasiparticle system as much as possible.

The energy balance between quasiparticle and phonon systems can be inferred from the characteristic phonon pair breaking time τ_{pb} and the characteristic quasiparticle recombination time τ_r.[Narayanamurti, 78] If $\tau_{pb} \gg \tau_r$, most of the energy will reside in the phonon system, as quasiparticles recombine (and emit

phonons) much faster than phonons dump their energy into the quasiparticle system by breaking pairs. Although there are numerous exchanges of the energy from phonons to quasiparticles and back again, the hotspot dissipation will proceed with velocity determined by the phonons. This is because the hotspot energy does not reside in the quasiparticle system for an appreciable fraction of time. Of course, the converse is true for $\tau_{pb} \ll \tau_r$. In near-equilibrium situations, theoretical calculations explicitly demonstrate that τ_r decreases strongly with temperature, while τ_{pb} displays the opposite temperature dependence.[Kaplan, 76] This behavior is also observed in (moderately) non-equilibrium experiments using laser excitation of superconducting lead films.[Hu, 77] The "crossover" temperature where $\tau_{pb} = \tau_r$ is material dependent and determines how effectively the material can convert x-ray energy into quasiparticles with minimal loss of energy from the desired quasiparticle system. A high crossover temperature is desirable, as quasiparticle transport dominates below this temperature. Theoretical estimates of crossover temperatures for several important materials are given in Table 2.2.1.[Booth, 91]

Material	$T_{crossover}/T_c$
Al	1.0
Ta	0.97
Nb	0.95
Sn	0.91
Pb	0.76
In	0.72

Table 2.2.1: Crossover temperature (where $\tau_{pb} = \tau_r$) for several materials.

From this table, aluminum is seen to perform very well, as most of the x-ray energy should reside in the quasiparticle system at temperatures as high as T_c. Indium and lead have been experimental disappointments as detectors [Booth, 91], presumably due to their low crossover point.

Note that it is only realistic to talk of a superconductor's "temperature" when the quasiparticles are close to the gap edge, and have a significant contribution to the BCS gap equation integral. This implies several ($\approx$ 5) energy transfers from phonons to quasiparticles and back have taken place since the members of the phonon and quasiparticle systems were near the Debye energy.[Gray, 88] For materials like

tantalum, where the energy is likely to reside in the quasiparticle system after only a few scatterings, one can simply estimate the effectiveness of hotspot dissipation as follows: only when quasiparticles are near the gap energy Δ will they significantly suppress the gap; when quasiparticles emit phonons, the typical phonon energy is $\approx E_{qp}/2$ [Eisenmenger, 81]; thus the last inelastic scattering before significant gap suppression occurs on average for quasiparticles near $\approx 4\Delta$. Because the inelastic scattering time gets significantly longer for lower energy quasiparticles, the effective "warm spot" volume can be estimated using the distance quasiparticles travel in the inelastic scattering time for quasiparticles of energy $\approx 4\Delta$. For tantalum, this inelastic scattering time is $\approx$ 100 psec.[Kaplan,76] As calculated above, the volume enclosed by the quasiparticles important in gap suppression is thus $\approx 35\ \mu m^3$. The relevant number for energy density due to a 6 keV x-ray is thus 6 keV / 35 μm^3 = 170 eV/μm^3, significantly less than the condensation energy of the superconducting pairs in tantalum.

Tantalum therefore is a promising material for use as an x-ray energy to quasiparticle number converter. There should be little effect from hotspots in increasing the value of ε. Using Kurakado's [82] calculation that 60% of the x-ray energy eventually resides in the quasiparticle system, one can realistically expect nearly 0.6 x 6 keV/($\varepsilon \approx \Delta$ = 700 μeV) = 5.1 million quasiparticles to be produced in tantalum by a 6 keV x-ray. These quasiparticles are then subject to the influences of the remaining processes detailed in Figure 2.2a.

2.2.2 Quasiparticle Recombination

A STJ will exhibit high energy resolution only if it collects a large fraction of the charge created by an absorption event. In the devices presented in this thesis, the recombination of quasiparticles back into Cooper pairs should dominate all other quasiparticle loss processes. Kaplan *et al.* [76] calculate quasiparticle lifetimes for clean superconductors near equilibrium; these numbers will be used in this thesis, as more suitable numbers for films far from equilibrium are not yet available. (Our experimental data do not cast doubt on the approach of using Kaplan *et al.*'s numbers, but future experiments will test this issue more critically.) Below, the connection between the equilibrium and nonequilibrium conditions is described such that quantitative predictions of nonequilibrium situations can be made based on Kaplan *et al.*'s [76] computations. (See also the treatments by Gray [71], Gray [81], and de Korte *et al.* [92].)

Before discussing the recombination of quasiparticles in the presence of an x-ray absorption event, we can get an idea of the magnitude of the problem by looking at the near-equilibrium recombination time, τ_r. For a small number of excess quasiparticles injected into a superconducting film, the excess quasiparticle number will decay exponentially with time constant τ_r. Theoretical values for this time constant are as follows:[Kaplan, 76]

Al at 0.3 K, $\tau_r = 8.7$ μsec, and

Ta at 0.3 K, $\tau_r >> 1$ sec.

Experimentally determined Al lifetimes in experiments by others are consistent with the above theory.[Gray, 71] Similar experiments involving Ta have not been performed, but from calorimeter experiments [Stahle, 92], it can be inferred that nonidealities (e.g., localized single quasiparticle loss centers) might limit the effective lifetime to tens of milliseconds at low temperatures. If the quasiparticles can tunnel through the STJ barrier to be collected by the preamplifier in a tunnel time (Section 2.2.4) much shorter than this recombination time, then we can expect relatively low quasiparticle losses due to recombination. Of course, one must bear in mind that the large deviation from equilibrium in x-ray experiments make these numbers somewhat inapplicable.

To determine the recombination rate in films with a large number of excess quasiparticles, one must calculate the number of ways one can make Cooper pairs out of N quasiparticles: $N(N-1)/2 \approx N^2/2$ for large N. Defining R as a recombination rate per unit density of quasiparticles, the total rate at which recombination occurs is

$$-\left.\frac{\partial N}{\partial t}\right|_r \approx N^2 \frac{R}{V} \qquad (2.2.2a)$$

where V is the volume of the superconductor. The factor of 1/2 above is lost because each recombination event eliminates two quasiparticles. Using an exponential decay of quasiparticle number with time, one can write

$$-\left.\frac{\partial N}{\partial t}\right|_r = \frac{N}{\tau_r} \quad ,$$

and can identify the recombination time as

$$\tau_r \equiv \frac{V}{N \cdot R} \equiv \frac{1}{n \cdot R} \quad .$$

This expression, combined with Kaplan *et al.*'s [76] expression for the low temperature τ_r and the thermal density of quasiparticles [Eisenmenger, 81]

$$n_{th} = 2N_0\sqrt{2\pi\Delta k_B T}\; e^{-\Delta/k_B T} \quad ,$$

gives

$$R \approx \left(\frac{2\Delta}{k_B T_c}\right)^3 \frac{1}{4\, N_o\, \Delta\, \tau_o} \quad .$$

Here, N_o is the single spin density of states at the Fermi level (1.2×10^{22} /eV•cm^3 for Al, and 4.1×10^{22} /eV•cm^3 for Ta). τ_o is a material dependent characteristic time calculated for several materials by Kaplan *et al.* [76], and is related to the strength of the electron–phonon coupling ($\tau_o \approx 4.4 \times 10^{-7}$ sec for Al, and 1.8×10^{-9} sec for Ta). For low T/T_c, R is temperature insensitive, and is approximately 9.6 μm^3/sec for Al and 260 μm^3/sec for Ta.

Equation 2.2.2a can be easily adapted for the presence of excess quasiparticles generated by an x-ray; the important quantity for detectors is the loss rate due to recombination

$$\Gamma_r \equiv -\frac{\partial(n_{th}V + N_x)}{\partial t}\bigg|_r \approx \left(2N_x n_{th} V + N_x^2\right)\frac{R}{V} \quad ,$$

where the term independent of excess quasiparticles has been removed because it exactly cancels thermal generation. The first term in the last expression represents excess quasiparticles recombining with the background thermal quasiparticles, and the second term represents "self-recombination" among only the excess quasiparticles. This equation demonstrates a need for low temperature operation (small n_{th}) and large volume films (small self-recombination). Note also the factor of two in the first term, implying that (for negligible self-recombination) the loss rate is actually twice as fast as in the equilibrium situation considered by Kaplan *et al.* [76]. Self-recombination only increases this rate even more. Table 2.2.2a shows the importance of each term with respect to temperature for Al and Ta films representative of our devices.

Table 2.2.2a shows that the recombination losses in our Ta films will be insensitive to temperature in the range of interest. Due to the large Ta bandgap (700 μeV; $\Delta/k_B \approx 8.1$ K), relatively few thermally excited quasiparticles exist, and self-recombination dominates. The losses can be reduced by increasing the Ta film volume. Aluminum, however, is quite different at the same temperatures, owing to its much smaller bandgap (170 μeV; $\Delta/k_B \approx 2.0$ K). Self recombination dominates only below ≈ 0.3 K, but a significant thermal contribution is still present at 0.25 K. One can reduce losses in the Al film either by increasing the film volume or by reducing the temperature. Because the recombination rates calculated in Table 2.2.2a are functions of the number of excess quasiparticles (which is a function of time), one cannot immediately determine if the total quasiparticle losses are prohibitively large; an iterative computer algorithm is necessary to determine the number of excess

Aluminum, $N_x = 5 \times 10^6$

V, μm^3	T (K)	n_{th}, /μm^3	$\Gamma_{r,\,thermal}$	+ $\Gamma_{r,\,self}$	= Γ_r, /sec
500	0.25	1500	1.5×10^{11}	4.8×10^{11}	6.3×10^{11}
	0.3	6000	6.0×10^{11}	4.8×10^{11}	1.1×10^{12}
	0.35	16,000	1.6×10^{12}	4.8×10^{11}	2.1×10^{12}
850	0.25	1500	1.5×10^{11}	2.8×10^{11}	4.3×10^{11}
	0.3	6000	6.0×10^{11}	2.8×10^{11}	8.8×10^{11}
	0.35	16,000	1.6×10^{12}	2.8×10^{11}	1.9×10^{12}

Tantalum, $N_x = 5 \times 10^6$

V, μm^3	T (K)	n_{th}, /μm^3	$\Gamma_{r,\,thermal}$	+ $\Gamma_{r,\,self}$	= Γ_r, /sec
10,000	0.25	2.2×10^{-7}	570	6.5×10^{11}	6.5×10^{11}
	0.3	5.3×10^{-5}	1.4×10^5	6.5×10^{11}	6.5×10^{11}
	0.35	2.7×10^{-3}	7.0×10^6	6.5×10^{11}	6.5×10^{11}
15,000	0.25	2.2×10^{-7}	570	4.3×10^{11}	4.3×10^{11}
	0.3	5.3×10^{-5}	1.4×10^5	4.3×10^{11}	4.3×10^{11}
	0.35	2.7×10^{-3}	7.0×10^6	4.3×10^{11}	4.3×10^{11}

Table 2.2.2a: Recombination rates for films representative of our devices.

quasiparticles as a function of time. Figure 2.2.2 shows the calculated total losses due to recombination alone, for representative Ta and Al films as a function of time. These curves can be fit by an exponential decay to give an effective recombination time τ_r, tabulated in Table 2.2.2b. The curves and fits for Ta films were nearly identical for the temperatures below 0.3 K (calculations were not performed for higher temperature films), so only one curve is seen for each film volume.

The results presented in Figure 2.2.2 and Table 2.2.2b are consistent with the above generalizations regarding temperature and volume effects on recombination. One immediate observation is that the effective recombination time in the Al films at 0.3 K is not much smaller than the near-equilibrium values discussed at the beginning of this section. The Ta values, however, indicate the possibility of substantial losses compared to the near-equilibrium situation. Section 2.2.3 will illustrate how phonon

trapping can significantly lengthen the effective Ta quasiparticle recombination time so that we may neglect recombination in the Ta alltogether. Section 2.2.4 will discuss the relation between quasiparticle tunnel time and quasiparticle losses, given these results for effective recombination time.

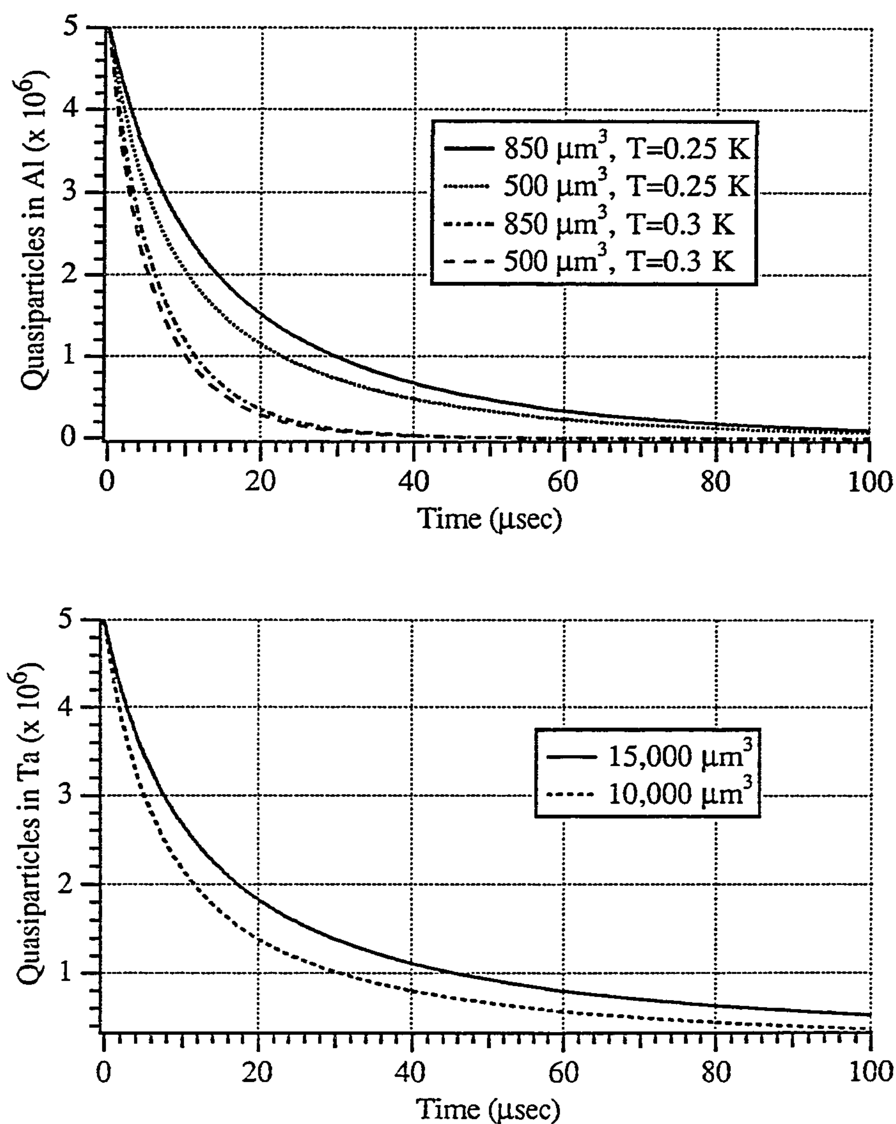

Figure 2.2.2: Quasiparticle losses due to recombination for isolated Al (top) and Ta (bottom) films, assuming no phonon trapping. Initial $N_{qp} = 5 \times 10^6$ in all films.

Material	Volume, μm^3	Temperature, K	τ_r, μsec
Al	850	0.25	17
Al	500	0.25	13
Al	850	0.30	7.1
Al	500	0.30	6.4
Ta	15,000	$\leq$ 0.30	18
Ta	10,000	$\leq$ 0.30	14

Table 2.2.2b: Effective recombination time of various films due to the addition of 5×10^6 quasiparticles.

2.2.3 Phonon Trapping

A potential advantage of superconducting detectors over semiconducting detectors arises from the Debye energy being larger than superconducting energy gaps. ($k_B\theta_D$ is smaller than typical *semi*conducting energy gaps.) When charge carriers recombine in superconductors, a phonon of energy $\Omega > 2\Delta$ is emitted -- and can break another Cooper pair. The phonon energy in a semiconductor, however, would simply be lost from the charge collection process. Due to the short phonon Cooper pair breaking time τ_{pb} and the significant probability of phonon reflection at the film–substrate interface, recombination phonons will frequently break pairs before escaping to the substrate or anharmonically decaying. This increases the effective quasiparticle recombination time, and can lead to more efficient charge collection.

As in section 2.2.2, we apply near-equilibrium results to obtain understanding about the non-equilibrium situation. Rothwarf and Taylor [Rothwarf, 67] were the first to identify this "phonon trapping" process, and they make the assumption that the rate at which phonons generate quasiparticles is proportional to the number density of phonons with energy $\Omega > 2\Delta$. The constant of proportionality $2/\tau_{pb}$ is the generation rate per unit density of phonons, where the factor of two reflects the production of two quasiparticles for each pair-breaking phonon. The Rothwarf-Taylor relation can be combined with the phonon loss rate (by decay or to the substrate) γ to give the effective quasiparticle recombination time with phonon trapping [Gray, 71],

$$\tau_r^* = \tau_r\left(1+\frac{1}{\gamma\,\tau_{pb}}\right) \quad .$$

The enhancement of τ_r is dependent on quantities such as the phonon mean free path against pair breaking, the film thickness, and the acoustic mismatch between the film and substrate. Gray [71] gives a lengthy expression for the factor which multiplies τ_r, with leading term $\frac{4d}{\alpha\Lambda}$, where d is the film thickness, α is an average phonon transmission coefficient, [Kaplan, 79] $\Lambda = c_s\tau_{pb}$ is the phonon mean free path against pair breaking, and c_s is an average phonon velocity. Corrections to the leading term are less than 10% for the devices studied here. Table 2.2.3 summarizes phonon trapping effects for typical films in our tunnel junction detectors.

Film	d, Å	α†	c_s, cm/sec†	τ_{pb}, sec††	τ_r^*
Al on SiO_2	2000	0.7	4.0×10^5	2.4×10^{-10}	$\approx 1.2\ \tau_r$
Ta on SiO_2	6000	0.25	2.5×10^5	2.3×10^{-11}	$\approx 170\ \tau_r$

† Kaplan, 79; †† Kaplan, 76

Table 2.2.3: Phonon trapping enhancement of quasiparticle recombination time.

Note that due to phonon polarization differences and possible diffusive phonon transport, the calculated recombination time enhancement in Table 2.2.3 will probably be accurate only to within a factor of 5. Without data from experiments designed to specifically address the phonon trapping question, one cannot make definitive statements regarding the enhanced quasiparticle lifetime. We can infer from Table 2.2.3, however, that the enhancement factor in the Al films is significantly smaller than in the Ta films. This is intuitively straightforward, given the stronger electron–phonon coupling in Ta (and thus faster pair breaking), and given the thicker Ta film in which phonons will reside somewhat longer before attempting to cross the film–substrate boundary. Only about 20% of the 2Δ phonons in Al will break pairs before escaping to the substrate, whereas more than 99% of the 2Δ phonons in Ta will break pairs.

Note also that anharmonic decay of phonons should not be a significant loss process compared to phonon transmission into the substrate. Gaitskell [93] predicts that decay of $\Omega = 2\Delta$ phonons in Al should require milliseconds, and in Ta should require $\approx$ 10 μsec. The information in Figure 2.2.2 and Table 2.2.3 indicates that recombination losses in Ta should be minimal, whereas the Al films could still be the

location of substantial losses. However, the device design techniques discussed in Section 3.3.2 and the tuning of quasiparticle tunnel times offer some methods of minimizing recombination losses in the Al films.

2.2.4 Quasiparticle Tunneling

Quasiparticle tunneling is the process by which charge is actually detected in the device. For the best device energy resolution, the quasiparticles must tunnel quickly so that losses are not significant. Practical considerations limit the tunnel rate to values in the 10^5 to 10^7 per second range – of the same order as inverse quasiparticle recombination times. Thus, control of the tunnel rate is a major concern in the design of STJ detectors.

The tunnel rate is proportional to the transmissivity of the barrier and the frequency of quasiparticles impinging on the barrier. The transmissivity is most sensitive to the tunnel barrier thickness, and is measurable in terms of the tunnel junction resistivity ($R_{nn} \cdot A$) at bias voltages $V_{bias} >> 2\Delta/e$. A typical tunnel barrier in our devices has current density ≈ 25 A/cm^2, which corresponds to a probability of about 10^{-8} per attempt that a quasiparticle will cross the barrier. For reasonable tunneling rates, one must therefore have large attempt frequencies. The frequency at which quasiparticles attempt to cross the barrier is inversely proportional to the superconductor film thickness d out of which the quasiparticle is tunneling. The transmissivity and attempt frequency give contributions to the expression for tunnel time between films of equal bandgap [de Korte, 92]:

$$\tau_t = 4q^2 N_o \, d \, (A \cdot R_{nn}) \frac{\sqrt{(\Delta + qV_{bias})^2 - \Delta^2}}{\Delta + qV_{bias}} \quad . \qquad (2.2.4a)$$

The factor of four arises from two electron spins and two quasiparticle branches. Only one quasiparticle branch can tunnel; the other branch must empty by mixing into the tunneling branch. As both branches are initially equally populated by an x-ray, and as the branch mixing time is typically several orders of magnitude faster than the tunneling time, only a factor of two is involved. The last term in the tunnel time equation corrects for the enhanced superconductor density of states near the bandgap. At reasonable bias points $\Delta/3 < qV_{bias} < \Delta/2$, this factor is between 0.65 and 0.75.

Parameterizing the above expression for Al–Al oxide–Al tunnel junctions ($V_{bias} = 80\ \mu$V) gives

$$\tau_t \approx \left(6 \times 10^{-9}\,\text{sec}\right)\cdot\left(\text{Al Volume in }\mu\text{m}^3\right)\cdot R_{nn}(\Omega) \quad . \qquad (2.2.4b)$$

This is ≈ 3 μsec for typical 850 μm^3, 0.6 Ω devices, and is dangerously close to the quasiparticle lifetime in the Al films. Figure 2.2.4 graphically illustrates the severity of quasiparticle recombination for long tunnel times.

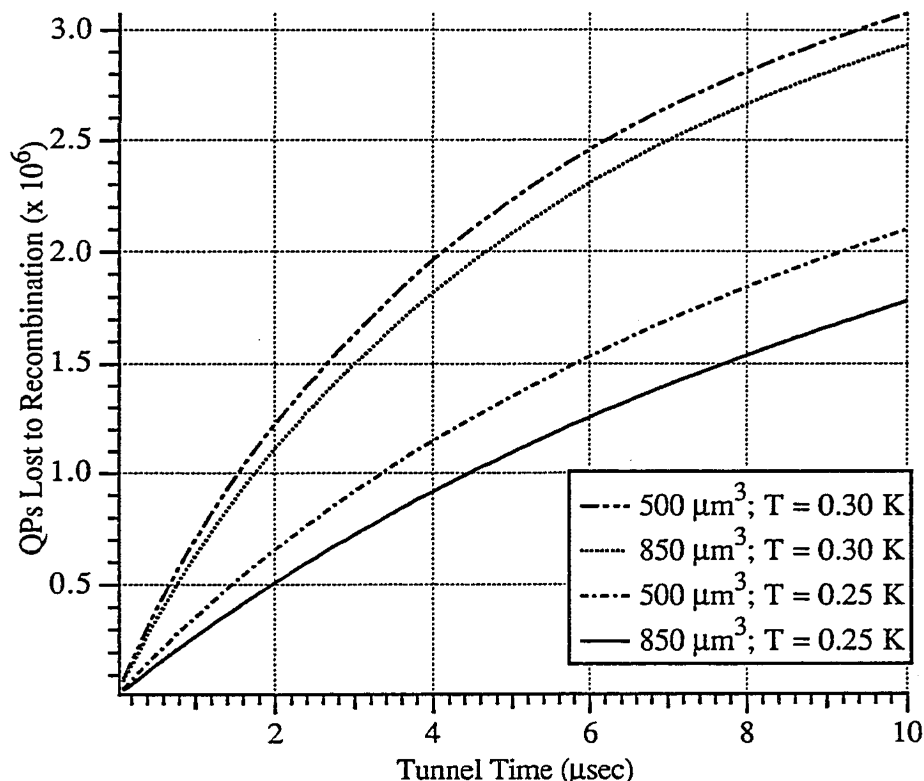

Figure 2.2.4: Quasiparticle recombination loss in Al as a function of tunnel time. Initial $N_{qp} = 5 \times 10^6$; does not include effects of phonon trapping.

Because quasiparticle self-recombination losses are inversely proportional to volume, and the tunnel time is proportional to volume, one can reduce quasiparticle losses only if R_{nn} is reduced. This will reduce the tunnel time (for constant volume films), or will reduce the self-recombination rate (for larger volume films, and constant tunnel time). The first option is best at operating temperatures above ≈ 0.25 K, as the recombination rate is not completely determined by self recombination. More detailed computer simulations presented in Chapter 8 for our devices indicate that self-recombination might be less severe than indicated in Section 2.2.2, and suggest that reducing the tunnel time will be more helpful than increasing the film

volume. Note, however, that successful reduction of tunnel junction resistance will likely require a good deal of effort, as lower R_{nn} devices often do not display ideal BCS I-V characteristics, and might be more difficult to match to the pulse amplifier electronics without some degradation in the signal-to-noise ratio.

2.2.5 Quasiparticle Outdiffusion

The most significant difference in the dynamics of STJ and semiconductor detectors arises from the inability of a superconductor to sustain an electric field. Quasiparticles in STJs must travel by diffusion to the tunnel barrier rather than by E-field induced drift. This results in two major difficulties: 1) the devices are inherently slower than *p-n* junctions and are thus unable to handle very high photon flux, and 2) quasiparticles can be lost through diffusion out the wiring leads if they do not first tunnel through the junction barrier. The first difficulty is not expected to be severe, as celestial x-ray sources are not high flux. The latter difficulty can be quite important, however, as outdiffusing quasiparticles are lost from the charge collection process. This can severely degrade the energy resolution -- either by an enhanced value of ε or by exhibiting a very sensitive dependence on the x-ray absorption position.

The random walk, or diffusion, framework is an accurate one in which to treat the quasiparticles because typical device dimensions (tens of microns) are much larger than typical quasiparticle mean free paths (tenths of microns). The device films are thin enough that we should treat the diffusion in two dimensions. The standard diffusion equation, with an initial δ function local source of N_X quasiparticles (the x-ray absorption) is [Jochum, 93]

$$\frac{\partial n}{\partial t} - D\,\nabla^2 n = N_x\ \delta(t)\ \delta(x - x_o)\ \delta(y - y_o) \quad ,$$

where n is the number density of diffusing quasiparticles and D is the diffusion coefficient. The solution to this equation is straightforward (for no boundaries):

$$n(x,y,t) = \frac{N_x}{4\pi\, D\, t}\ e^{-\left(\left(x^2+y^2\right)/4Dt\right)} \quad .$$

The standard deviation of the Gaussian, $\sqrt{2Dt}$, can be taken as an effective diffusion length $L_D(t)$.

The diffusion coefficient D is given by $\approx \frac{1}{3} v l$, where v is the quasiparticle velocity, and l is the quasiparticle mean free path ($\approx$ three dimensional). There is some question as to what value should be used for v. The Fermi velocity v_F is valid for normal metals, but the dispersion curve E_{qp} vs. k in superconductors has a minimum at the gap edge, implying zero group velocity. Thermal excitation will

prevent quasiparticles from sitting directly on this minimum, so the average velocity will be somewhere between 0 and v_F: [Narayanamurti, 78]

$$v \approx \sqrt{\frac{2k_BT}{\pi \Delta}} \cdot v_F \quad .$$

At a typical operating temperature of 0.3 K, $k_BT \approx 26\ \mu eV \approx \Delta_{Ta}/27 \approx \Delta_{Al}/6.6$, predicting quasiparticle velocities significantly below v_F in both Ta and Al films. In a nonequilibrium superconductor, the velocity should be much closer to v_F than the above equation implies -- particularly if the quasiparticle distribution is highly nonthermal. From Kaplan [76], we can assume that x-ray generated quasiparticles will remain above 1.1Δ in Ta, and above 1.5Δ in Al for more than 1 μsec (longer than the expected time necessary to diffuse across the films in the device at v_F). From a simple free-electron model of the Fermi surface,[Ashcroft, 76] one finds that quasiparticles at 1.1Δ in Ta will travel at about 40% of the Fermi velocity, and quasiparticles at 1.5Δ in Al will travel even closer to the Fermi velocity. Figure 2.2.5 displays the relative velocities for quasiparticles based on the free electron model and the BCS theory. The simple model used to generate Figure 2.2.5 appears to be not far wrong. Kraus [94] indicates that measurements of his tin devices are consistent with a quasiparticle velocity within a factor of two of the Fermi velocity.

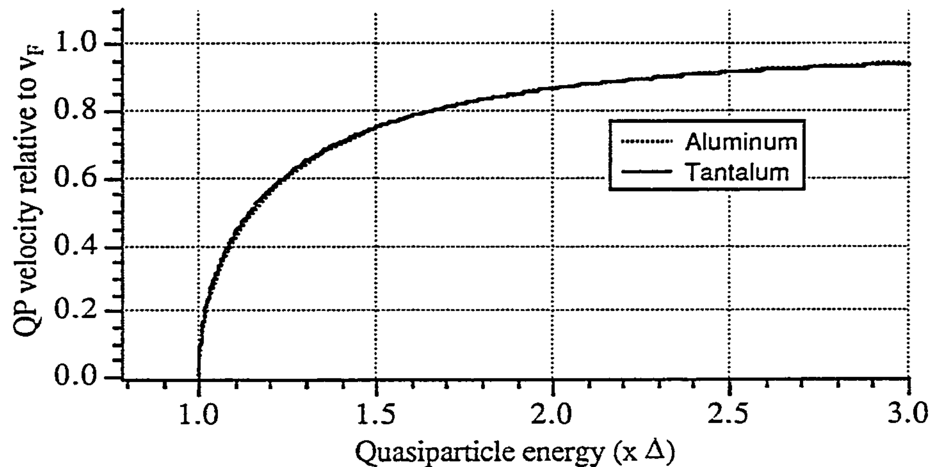

Figure 2.2.5: Quasiparticle velocity as a function of quasiparticle energy.

For times shortly after the x-ray absorption, the quasiparticles will travel with velocities close to the Fermi velocity. As the quasiparticles lose energy by phonon emission, they will slow down. The complex time dependence of the velocity makes

it difficult to assign a single value to the velocity in the diffusion constant, but it is likely that the Fermi velocity v_F is not a bad approximation.

The Ta and Al films used in our devices are deliberately fabricated in such a way as to give the highest quality films possible from our deposition equipment. The residual resistance ratio (RRR) in our Ta is ≈ 20, and in our Al is ≈33 unless limited by boundary scattering; 2700 Å films of Al exhibit RRR ≈ 9.5. The low temperature resistivities for these films are 0.74 μΩ-cm, 40 nΩ-cm, and 0.18 μΩ-cm, respectively. These values correspond to mean free paths of 1100 Å in the Ta, 9850 Å in thick Al films, and 2250 Å in the thin Al film. The diffusion constant for the Ta films is $D_{Ta} \approx 500$ cm^2/sec. For Al films in our devices, we typically use a thickness of only 2000 Å, so the mean free path is probably a bit less than 2000 Å. This makes the relevant diffusion constant $D_{Al} \approx 1300$ cm^2/sec. This large diffusion constant makes for rapid spreading of quasiparticles in our Al films: in 1 μs, the quasiparticles should diffuse ≈ 500 μm in our Al.

The largest device dimension is the length of the Ta absorber, 200 μm. With the above diffusion constant, the diffusion time to cover the 200 μm in Ta is 0.4 μsec. Note that this diffusion time is not much smaller than self-recombination times. The diffusion process may thus set a limit on the size of a useful device: for a 1 mm Ta device, the diffusion time is 10 μsec. The self-recombination rate might be significantly smaller in this larger volume film, so the long time might not result in devastating losses. However, the diffusion time does take part in determining the overall response time of the device, and the allowable incident x-ray flux (see Section 4.1.1). Because the time to diffuse a given distance is inversely linear in the velocity used to determine the diffusion constant, a reduced quasiparticle group velocity would be quite noticeable in the time we observe quasiparticles to traverse the device films. Devices employing larger Ta absorber films will likely require cleaner Ta, for longer quasiparticle mean free path and thus higher diffusion constant.

The diffusive nature of the quasiparticles can also result in significant quasiparticle losses through the contact leads. The situation is worsened if the tunnel time is comparable to or larger than the quasiparticle out-diffusion time. De Korte [92b] estimates the fraction of detected charge for a tunnel junction with area A and lead width w as

$$\frac{Q_{det}}{Q_o} \approx \frac{A}{A + w\sqrt{\pi D \tau_t}} \quad . \tag{2.2.5a}$$

The situation, however, is not hopeless, as quasiparticle trapping (discussed in Chapter 3) can effectively prevent diffusion away from the tunnel junction. This is

accomplished by the use of Nb leads. There is another region of the device, the Al counterelectrode, where we want to enhance the quasiparticle outdiffusion. This will prevent backtunneling.

2.2.6 Quasiparticle Backtunneling

Another feature unique to STJ detectors is that quasiparticles can not necessarily be forgotten after they tunnel out of the x-ray absorbing film. There are two possible means of effectively tunneling back into the absorbing side of the tunnel barrier. Reverse tunneling is simply the opposite of the tunneling process, and will reduce the detected current. Quasiparticles can also "backtunnel," apparently moving a single quasiparticle back to the absorbing film -- but actually increasing the current. The processes are outlined in Figure 2.2.6 with density of states diagrams for the two superconducting films separated by the insulating barrier.

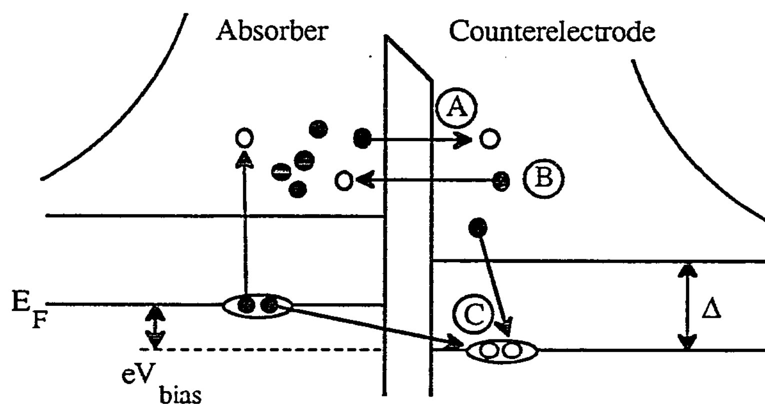

Figure 2.2.6: Quasiparticle tunneling (A), reverse tunneling (B), and backtunneling (C).

Reverse tunneling can be made negligible by ensuring that the reverse tunnel time is much longer than the time for a quasiparticle to outdiffuse or to scatter below the opposite film's gap edge. For a typical bias of 80 μV in Al–Al oxide–Al junctions, the relevant scattering time is ≈ 1 μsec at 0.3 K.[Kaplan, 76] The reverse tunnel time can easily be made much larger than this by using thick counterelectrode films with fast outdiffusion, as is done in our devices.

In backtunneling, due to the breaking and creation of Cooper pairs, energy and charge are both conserved. The quasiparticle in the non-absorbing film merely makes this process quantum-mechanically allowed. The "backtunneled" quasiparticle can tunnel and backtunnel many times before it is lost due to outdiffusion or recombination. This results in amplification, and has been used in a type of superconducting transistor.[Gray, 78a] Some workers in the detector field [Mears, 93] use this approach to greatly increase the signal-to-noise ratio. (This method is effective if the preamplifier is the dominant noise source: backtunneling increases the quasiparticle signal, but does not affect the preamplifier noise.) The signal gain can be estimated as τ_l/τ_t, where τ_l is the overall quasiparticle loss time (due to recombination or outdiffusion). Note that for films near equilibrium, the backtunnel time is generally set by the forward tunnel time -- i.e., it is not set by the volume of the counterelectrode film as in the case of reverse tunneling.[Gray, 81] However, if the quasiparticles in the counterelectrode diffuse quickly away from the tunnel barrier region, the effective backtunnel time will be much greater than the forward tunnel time. The gain from backtunneling can exceed 5 in reasonably simple devices.

The Fano-factor limited statistics of the initial hotspot of quasiparticle creation determine the best energy resolution, and the random nature of the backtunneling or reverse tunneling processes can only worsen this statistical limit.[Goldie, 94] Reverse tunneling must be eliminated as it is always detrimental to the performance of the detector. Because of potential gain in signal to (electronic) noise ratio, backtunneling is useful in certain devices. The application for our devices (x-ray astronomy) requires the best energy resolution, and cannot afford the excess energy resolution broadening due to backtunneling. Thus, in our devices, we take pains to eliminate backtunneling and reverse tunneling entirely.

2.2.7 Quasiparticle Outdiffusion (from the Counterelectrode)

Perhaps the best way to eliminate backtunneling and reverse tunneling is to enhance quasiparticle diffusion away from the tunnel junction immediately after the quasiparticle has (forward) tunneled. One can deposit very clean, thick, and wide counterelectrode or counterelectrode wiring films to achieve this result. These films will have fast quasiparticle diffusion and effectively long tunnel times to re-enter the absorbing side of the tunnel junction. It is relatively straightforward to accomplish this goal with thermally evaporated Al, at thicknesses in our devices of $\approx 0.4\ \mu m$. Assuming a diffusion constant in the Al of at least 1300 cm^2/sec, equation 2.2.5a gives the fraction of charge actually backtunneling in our devices as approximately

2.5%. Indeed, backtunneling probabilities of less than 10% are observed in such devices we have fabricated (see Section 7.7), indicating that the diffusion constant might be larger than 1300 cm^2/sec, or that significant recombination losses take place in the Al film before backtunneling can occur.

2.3 Discussion

The discussion in this chapter introduces many of the fundamental issues of importance in the STJ detectors, and indicates that, while these devices are indeed complex, they do appear feasible. Tantalum films should provide efficient conversion of x-ray energy into quasiparticles, and, with significant phonon trapping, these films should exhibit low quasiparticle recombination losses. The aluminum films used in the fabrication of our device tunnel barriers might exhibit significant recombination losses, but will prove very useful in the quasiparticle trapping to be discussed in Chapter 3.

There is a surprising amount of detail in the operation of the simple device introduced in Section 2.2. The simplification that we need only detect an effective temperature rise in our device is in fact a very gross simplification. Because phonons can break superconducting Cooper pairs, the dynamics of these devices can be significantly more complicated than the similar semiconducting *p-n* junction detectors. The discussion in Chapter 3 introduces superconductor bandgap engineering and quasiparticle trapping, both of which will only add to the complexity of these devices. However, the promise of greatly improved single photon energy resolution makes this complexity acceptable.

3. Superconductor Bandgap Engineering

The needs of x-ray astronomers can pose difficult challenges to device physicists. Perhaps the most demanding device requirement is a high x-ray absorption efficiency. Celestial x-ray sources present very few x-ray photons to the detector (< 100 photons/sec); thus, the absorption efficiency of the detector must be maximized to ensure realistic observation times. This requires a relatively thick film to capture almost every photon incident on the film, and large film areas (ideally greater than 0.5 mm x 0.5 mm) to allow for telescope drift. As will be explained in this chapter, the device described in Figure 2.2a will not easily fulfill these requirements while still delivering the necessary energy resolution $\Delta E_x/E_x < 1\%$ over the photon energy range of interest, 100 eV to 10 keV. With the use of superconductor bandgap engineering, however, it becomes apparent that the requirements of high efficiency and high resolution are not mutually exclusive in a STJ device.

3.1 Device Requirements

One of the major advantages STJs hold over high energy resolution microcalorimeters is the possible ease of array fabrication with standard thin film photolithographic processing. Two dimensional arrays of STJs hold much promise as imaging detectors for x-ray astronomy, and a planar thin film STJ design should prove simpler and more reliable than micromachined devices. To maintain this advantage, STJs should be designed compatible with thin film technology (as opposed to using foils or bulk single crystals). While metal films of thicknesses < 1 µm are relatively straightforward to process with standard semiconductor lithography techniques, thicker films will pose some difficult, but not insurmountable, technical challenges.

Unfortunately, for x-rays of energy as high as 10 keV, 1 µm thick films will not exhibit very good absorption efficiency. As shown in Figure 3.1, the x-ray absorption depths of common superconductors are somewhat longer than desirable for standard thin film processing. Aluminum forms excellent films and robust oxide tunnel junctions, but more than 35 µm of Al would be necessary to give 67% absorption efficiency -- certainly not a "thin" film. The most absorbant superconductor in the figure is Ta; a 1 µm thick film of Ta will be ≈ 43% efficient in absorbing 6 keV x-rays. A 2 µm thick film of Ta will be ≈ 67% efficient at the same

energy. The important iron lines in celestial sources lie near 6 keV, making it imperative that the STJ detectors have good efficiency near that energy. The efficiency of a 2 μm thick Ta film will perhaps be adequate for astronomers, but the ≈ 6% efficiency of the same thickness of Al will certainly not. For this reason, among others (see Chapter 5), we use Ta in our devices as the x-ray absorbing film.

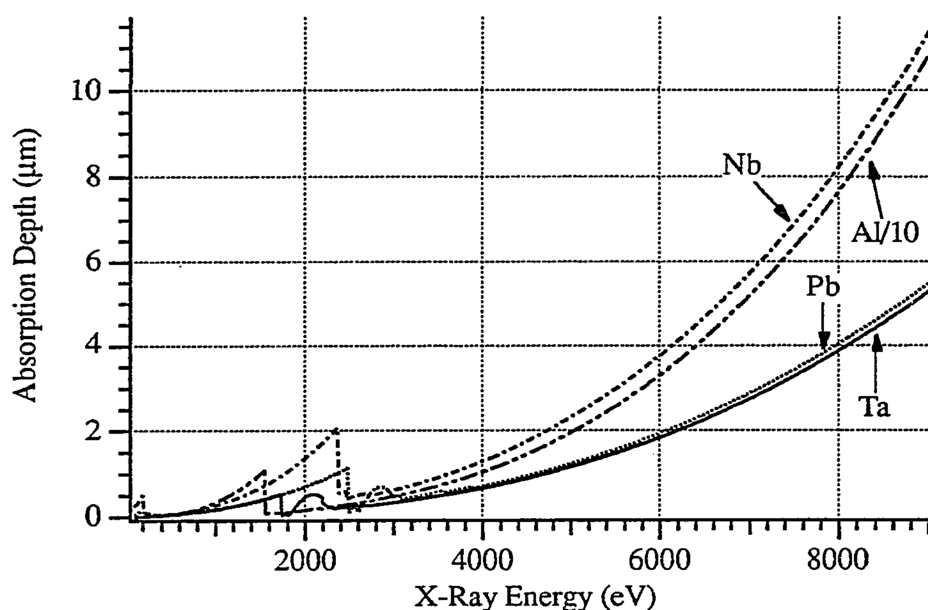

Figure 3.1: X-ray absorption depths of several superconductors.[Brennan, 92]

It is enlightening now to consider the tunnel time of quasiparticles from a Ta film which is 2 μm thick and 0.5 mm x 0.5 mm in area. The tunnel barrier normal state resistance should not be any less than about 10 mΩ, or shot noise will become a problem. (This assumes that whatever barrier we use to form the oxide will follow the same qualitative behavior of I_{bias} vs. T as seen in the work of Mears [93] and Kraus [89a], and that the operating temperature is ≈ 0.3 K.) From the equations in Section 2.2.4, we can thus estimate the tunneling time $\tau_t \approx 10^{-4}$ sec. Because of quasiparticle recombination, we can expect a significant loss of quasiparticles for this long tunnel time, and thus a broadening of the device's energy resolution. In addition, the pulse length will be long enough to cause pileup even at the low count rates expected from celestial sources. We need a smaller volume film (thinner) to speed up the tunneling. (Note that a useful device could *possibly* be fabricated in the simple fashion of Figure 2.2a. With perhaps smaller area devices (≈ 0.1 mm^2) and

extremely high quality tunnel barriers (> 5000 A/cm^2 to minimize capacitance -- see Chapter 4), one might obtain satisfactory performance. However, this is highly unlikely because such high current density barriers typically show prohibitively high subgap leakage current.)

Because the tunnel time is linear in the film thickness, d, and the absorption efficiency is inversely related to the exponential of film thickness, d, we are presented with confilicting requirements which cannot be adequately resolved for any choice of d. The use of quasiparticle trapping [Booth, 87] can greatly relax these constraints, allowing the use of thick absorbers and lower current density tunnel junctions (which typically give more ideal DC I–V characteristics). In addition, quasiparticle trapping will also provide the basis for position-sensitive STJ detectors.[Kraus, 89a]

3.2 Quasiparticle Trapping

The premise behind quasiparticle trapping is a separation of the functions of x-ray absorption and quasiparticle tunneling into two different films. One uses a thick, large area film for efficient x-ray absorption in contact with a small volume film with short tunnel time for the quasiparticle detection. The trick is getting the quasiparticles from the x-ray absorbing region (in the thick film) to be trapped in the tunneling region (the thin film) much faster than the quasiparticles recombine. When the quasiparticles are in the thin film, tunneling can then take place rapidly. If this two-stage process is faster than the direct tunneling from the single large volume film, we will accelerate the device response time, and possibly reduce quasiparticle recombination losses. The tunnel junction geometry and current density can be chosen for best matching to the charge amplifier (Chapter 4), without consideration of x-ray absorption efficiency.

We can utilize superconductor bandgap engineering to influence the motion of quasiparticles in the detector films. If the thick absorbing film has an energy gap larger than the thin tunneling film, quasiparticles which enter the tunneling film can emit a phonon and be trapped in the thin film. Figure 3.2a schematically illustrates this process. Quasiparticles generated in superconductor 1 (S1) diffuse rapidly throughout S1 and S2. While in the lower bandgap superconductor S2, the quasiparticles can emit a phonon, becoming effectively trapped in the potential well formed by S2. It is unlikely that phonons will excite trapped quasiparticles back into the higher gap film, because phonon-electron scattering is infrequent at the low temperatures of operation, and because phonons with $\Omega < 2\Delta$ exit the film

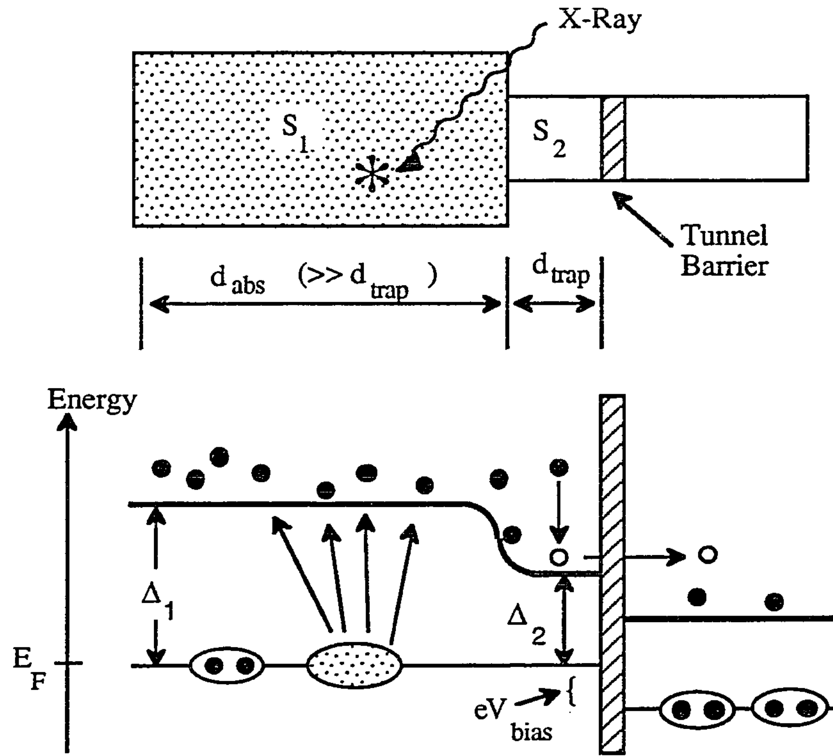

Figure 3.2a: Quasiparticle trapping.

quickly.[Kaplan, 76] If the volume of S1 is much larger than the volume of S2, one can obtain good x-ray absorption efficiency in S1 with much faster tunnel times in S2. Of course, the success of the trapping process relies on the diffusion time and phonon emission time being short on the time scale of quasiparticle recombination. Assuming the quasiparticles diffuse instantaneously compared to the time scale of interest, the fraction of time spent by a quasiparticle in the trap is just the volume fraction

$$V_{trap} / \left(V_{trap} + V_{abs} \right).$$

(Quasiparticles ideally will diffuse ≈ 100 μm in 200 ns in the Ta films used for our devices.) This results in a trapping time given by

$$\tau_{trap} = \tau_s \cdot \left(\frac{V_{trap} + V_{abs}}{V_{trap}} \right), \tag{3.2a}$$

where τ_s is the phonon emission (scattering) time for a quasiparticle of absorber gap energy Δ_1 in the trap superconductor S2, with gap Δ_2. Kaplan [76] calculates the

scattering time τ_s for quasiparticles in superconductors, and finds for low temperatures

$$\tau_s \propto \tau_o \cdot \left(\frac{\Delta_2}{\Delta_1 - \Delta_2} \right)^3 , \qquad (3.2b)$$

where τ_o is the material dependent characteristic time introduced in Section 2.2.2. Thus we see that quasiparticles at higher energies scatter much more rapidly, and a large difference $\Delta_1 - \Delta_2$ will make the trapping process faster and more effective.

Aluminum is an obvious choice of material for S2, as it has a bandgap much smaller than that of Ta, has long quasiparticle lifetime (although this implies a long τ_o), and forms robust, high quality oxide barrier tunnel junctions. The scattering time in Al for a quasiparticle of energy $\approx \Delta_{Ta}$ ($\approx 4\Delta_{Al}$) is approximately 20 nsec.[Kaplan, 76] Requiring that the trapping time be much less than the quasiparticle lifetime, Equation 3.2a dictates (for $\tau_{trap} < 3$ µs) that $V_{abs}/V_{trap} < 150$. Requiring that the tunnel time τ_t also be much less than the quasiparticle lifetime, Equation 2.2.4b dictates (for $\tau_t < 3$ µs for our typical 0.6 Ω, 25 A/cm^2 devices) that $V_{trap} < 850$ µm^3. Thus, with this resistance tunnel junction, we can utilize an absorber of dimensions ≈ 2 µm thick x 100 µm x 500 µm.

Reducing the junction normal state resistance to 0.1 Ω will allow us in the future to use 500 µm x 500 µm absorbing film areas. However, it will take quasiparticles ≈ 5 µs to diffuse through 500 µm of our RRR = 20 tantalum. This invalidates the assumption that diffusion is much faster than other time scales of interest, and will result in much longer trapping times. For such very large devices, epitaxially grown Ta will probably be necessary to increase the diffusion constant.

Quasiparticle trapping can also be used to control quasiparticle outdiffusion (Section 2.2.5). By using a superconductor with higher gap than the absorber to contact the absorber, quasiparticles will be prevented from diffusing out the leads. Figure 3.2b shows the structure, where high gap Nb (Δ ≈ 1500 µeV) is used as the wiring, intermediate gap Ta (Δ ≈ 700 µeV) is used as the absorber, and low gap Al (Δ ≈ 175 µeV) is used as the trap. Kraus [89b] has demonstrated this scheme to be very effective with the respective materials Pb, Sn, and Al.

For the Nb to be effective as an outdiffusion blocker, the quasiparticles in the Ta must inelastically scatter below the gap of Nb before they diffuse into the Nb. Based on the arguments in Section 2.2.1, it should take of order 100 psec for quasiparticles in Ta to scatter below the Nb gap edge. With a Ta diffusion constant of ≈ 500 cm^2/sec, this implies that x-ray absorptions within ≈ 5 µm of the Nb contact

will suffer some quasiparticle losses to the Nb. (Note that these quasiparticles can of course diffuse back into the Ta, but Nb is observed to have very short quasiparticle lifetimes [Mears, 93], so the losses due to the Nb can be significant.) Aside from minimal Nb–Ta contact area, our devices have no features to prevent this loss process. Future devices will have the Nb contact region masked off from the incident x-ray flux (see Figures 3.4.1a and 3.4.1b).

Also, as mentioned in Section 2.2.7, outdiffusion from the counterelectrode is desirable to prevent backtunneling. Although the use of thick Al films apparently accomplishes this quite well, one could also imagine using "reverse" quasiparticle trapping: depositing a normal metal film (e.g., Au) on top of the Al counterelectrode to trap quasiparticles in the counterelectrode away from the barrier.

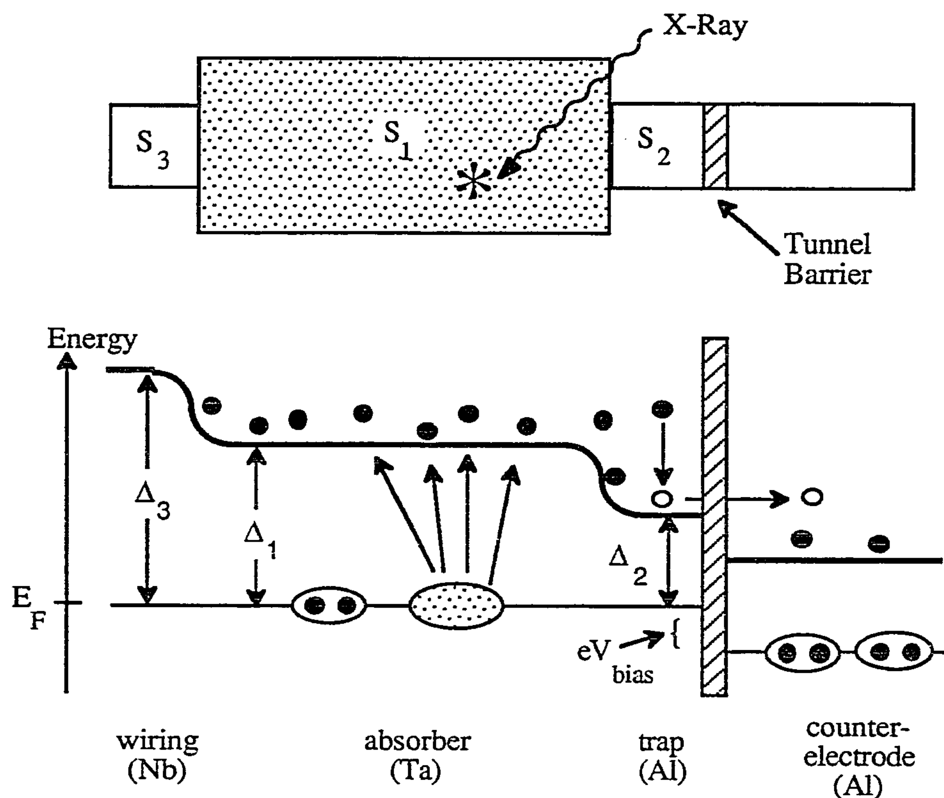

Figure 3.2b: Quasiparticle trapping with outdiffusion prevention.

3.3 The Absorber – Trap Interface

The effectiveness of quasiparticle trapping relies a great deal on the quality of the interface between the absorber and the trap. A clean interface will modify the film gaps and densities of states within a coherence length of the interface, and can thus change the trapping time through a modified phonon emission time. A damaged or partially reflecting interface can inhibit quasiparticle diffusion into the trap, lengthening the trapping time and causing a loss of information about the x-ray absorption position.

3.3.1 Proximity Effect

Several models exist to explain the nature of superconductivity near the interface between two superconductors. (For a good review, see Gilabert [77].) Due to the long range coherence of the superconducting state, and the local nature of the electron–phonon interaction responsible for superconductivity, there is a significant influence of one superconductor on another placed in contact with it. Useful theories of the proximity effect become quite complicated due to the spatial dependence of the Cooper pair amplitude (conventional BCS theory relies on translational invariance). Most theories thus begin with Green's function formalism, but then make varying assumptions, restricting the range of validity in the process of making the equations mathematically tractable. In addition, accurate experimental data for the verification of theoretical models are difficult to obtain for several reasons: the bilayer must contain no intermetallic compounds, the metals must have low solubilities in each other, there must be good control over film purity (mean free path), and one must be able to process the materials in a reliable fashion.

Because of such theoretical and experimental difficulties, a reliable description of the nature of superconductivity in our heterostructures is not available. To gain some insight into what we should expect in our films, however, we can apply one of the simpler, more intuitive models, put forth by DeGennes [64]. The simplifying assumptions of this model require that the mean free path, l, be much less than the coherence length, ξ, so that the reflection and transmission properties of the transition region do not play an important role. This leads to great simplification in the equations, but, as discussed below, the reflection at the interface can be important in our devices, as l is relatively large. DeGennes also requires that the superconductivity be weak (Δ small; e.g., $T \approx T_c$) so that the complex Gor'kov equations can be interpreted in terms of the much simpler Ginsburg–Landau theory. This

simplification is also not valid for our devices, but the incredible success of the Ginsburg–Landau theory at lower temperatures in describing general superconductivity indicates that this simplification might not be too damaging.

Figure 3.3.1a displays the superconducting gap parameter for a thick Ta film in contact with a thick Al film, as calculated in the framework of the DeGennes theory (the parameters being representative of our devices). This calculation is useful for understanding the nature of "lateral" trapping in our devices, as illustrated in Figure 3.3.2b. Here, Ta is the x-ray absorbing film, and Al is the quasiparticle trap (upon

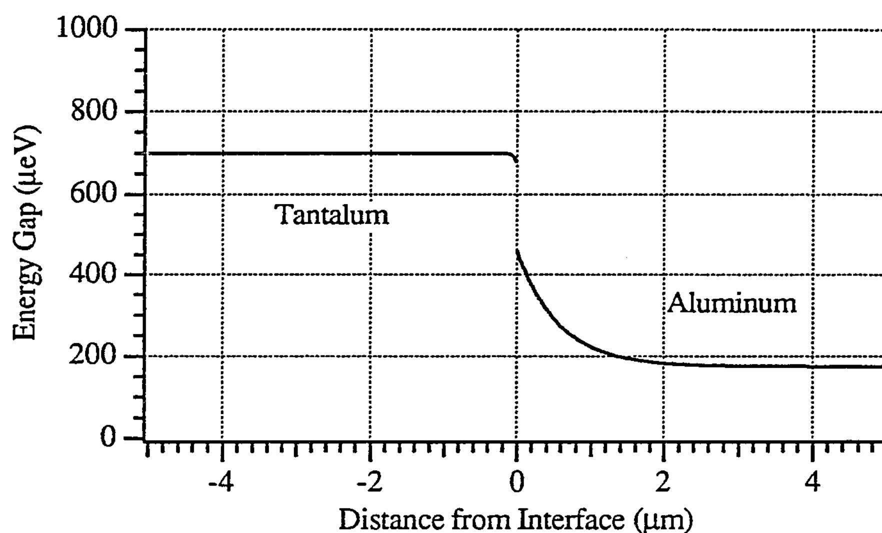

Figure 3.3.1a: DeGennes model prediction for thick Ta / thick Al films in proximity.

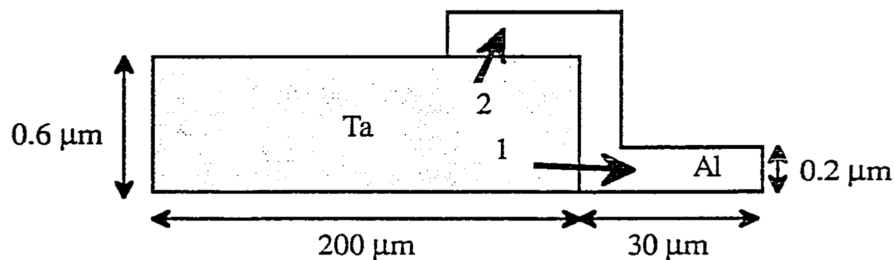

Figure 3.3.1b: Device model for proximity effect calculations.
1) Lateral trapping, and 2) vertical trapping.

which the tunnel junction would be formed). Figure 3.3.1a shows that the Al gap is significantly enhanced within ≈ 1 μm of the interface (ξ ≈ 5600 Å for this film). However, as the lateral Al film dimensions are much larger than this distance, and the quasiparticle diffusion in the Al is so rapid, the proximity enhanced region of the Al will have little effect on the trapping process. Note also from Figure 3.3.1a that the short coherence length in Ta (ξ ≈ 450 Å) makes the proximity depressed Ta layer very thin and with minimal gap suppression. In the trapping process, inelastic quasiparticle scattering will take place most rapidly in the Al film far from the interface, because of the E_{qp}^3 dependence of the scattering rate (Equation 3.2b).

The vertical proximity effect (#2 in Figure 3.3.1b) appears quite different from the lateral proximity effect. This is because the long Al coherence length prevents the Al gap from recovering within the thickness of the Al film, as illustrated in Figure 3.3.1c. For 2000 Å thick Al films on 6000 Å thick Ta, the Al gap remains between ≈ 400 μeV and 500 μeV throughout the film, significantly higher than the intrinsic Al gap of ≈ 175 μeV. This can have drastic consequences for the quasiparticle inelastic scattering rate, as suggested by Equation 3.2b. Assuming we

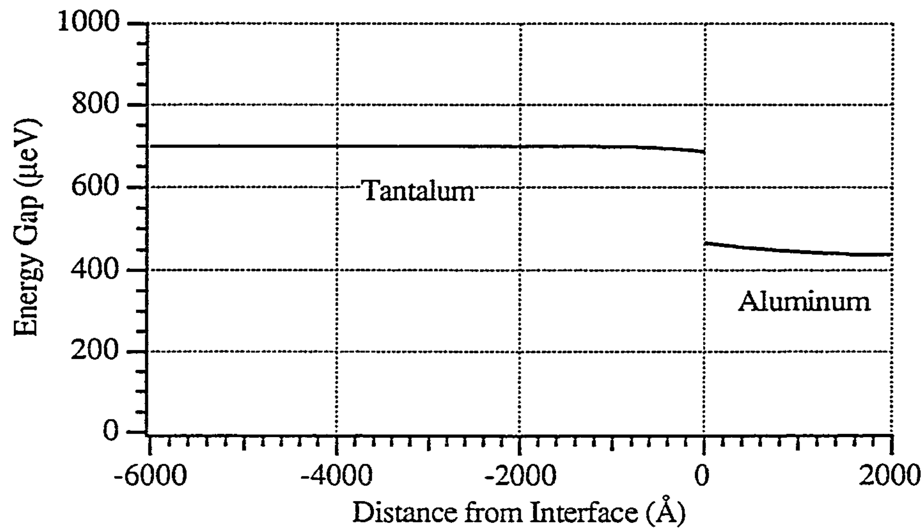

Figure 3.3.1c: DeGennes model prediction for thick Ta / thin Al films in proximity.

can use the same bulk Al electron–phonon coupling parameters for the proximity enhanced Al, we arrive at $\tau_s \approx 1.5$ μsec for quasiparticles of energy Δ_{Ta}. This renders the thin Al film ineffective in trapping: to minimize recombination losses, we

require $\tau_{trap} < \tau_t \approx 3$ μsec, and thus Equation 3.2a gives us no reduction in the trap volume with respect to the absorber volume -- and no reduction in tunnel time.

There are, however, at least two effects which make the estimate $\tau_s \approx 1.5$ μsec somewhat suspect (aside from the possible modification of electron–phonon coupling in Al due to the proximity effect). The first effect, which might lengthen the scattering time, is the softening of the density of states singularity in the Al. The proximity effect will change the densities of states near the interface to have peaks, but not strong singularities, at the adjusted local Ta and Al gaps.[Golubov, 89] Without the density of states singularity available to scattering quasiparticles, the scattering rate will be somewhat reduced. The other effect which makes the $\tau_s \approx 1.5$ μsec estimate somewhat unreliable is the possibility of quasiparticles entering the Al film with energy significantly above Δ_{Ta}. As discussed in Section 2.2.1, x-ray generated quasiparticles will diffuse more than 2 μm in the Ta before they fall below $2\Delta_{Ta}$. Thus, any x-ray absorption in the Ta directly below the Al film will present the Al film with many high energy quasiparticles. These high energy quasiparticles will scatter much faster in the Al trap, making the trapping more effective. This process, however, is undesirable as it gives an x-ray absorption position dependence to the trapping process, and thus to the collected signal charge. Experiments will be needed to determine the extent to which this vertical trapping broadens the energy resolution for several different thicknesses of Ta. The problem will likely be worse for much thicker films (as are desired for near unity photon absorption efficiency), as the quasiparticles could have to travel 2 μm or more just to reach the Al film directly above the absorption position. This results in a signal dependence on the height of the x-ray absorption within the Ta absorber.

The vertical trapping portion of the Al film must, however, be present to a large extent in our devices to aid in the transmission of quasiparticles from the Ta to the lateral Al trap. The Al–Ta interface will not be completely transparent to quasiparticles, so we must consider the area of the interface as an important parameter in determining the bottleneck in the trapping process. For small and/or dirty interfaces, such that the frequency of quasiparticle attempts to enter the Al trap is low, the bottleneck to quasiparticle trapping will be formed at the interface. If the interface is made large and clean, quasiparticle diffusion in the Ta, or quasiparticle inelastic scattering in the lateral Al forms the bottleneck in the trapping process.

The proximity effect calculations using DeGennes' theory will likely be not as accurate for dirty interfaces as the McMillan [68] model or the even more applicable (but complex) Golubov [89] model. With a low transparency interface, one can

expect the Al energy gaps in Figures 3.3.1a and 3.3.1c to be somewhat lower (and with less curvature) than shown in the DeGennes calculations. This will certainly enhance the quasiparticle inelastic scattering rate, but the trapping rate will be reduced because the quasiparticles will take longer to leave the Ta.

3.3.2 Poor Quality Interfaces

The quality of the Ta–Al interface in our devices is suspect because the Ta film is exposed to atmosphere (and several processing steps) before the Al trap is deposited. Although an ion beam cleaning of the Ta surface (see Appendix 1) is used *in situ* prior to the Al deposition, one cannot guarantee an interface free of damage or impurities. If this interface inhibits the transmission of quasiparticles from the Ta to the Al, excessively long trapping times can result. Note, however, that although quasiparticles may have difficulty traversing the Ta–Al interface, phonon transmission through the interface might actually be enhanced by a poor (graded) interface. The effect of phonon transmission through the interface is discussed in Section 3.4.1, and our experimental findings on interface quality are covered in Chapter 6.

Significant reflection at the absorber–trap interface can result in loss of information regarding the location of the x-ray absorption in double tunnel junction structures.[Kraus, 89a; Jochum, 93] Such reflection will allow the quasiparticle distribution to homogenize within the Ta absorber before tunnel junctions can sense any spatial nonuniformity in quasiparticle density. In addition, the trapping time will have an effect on quasiparticle recombination losses. If recombination losses in Ta dominate, then long trapping times will of course be harmful; one would hope to remove the quasiparticles from the Ta as fast as possible to minimize the losses. However, it is more likely that recombination losses in the Al trap will dominate, and long trapping times can actually reduce recombination losses. For tunnel time short compared to trapping time, the quasiparticle density in the Al will not build up very high, and the self recombination rate will be somewhat reduced. This is illustrated in Figure 3.3.2, where the recombination losses in an 850 μm^3 Al trap are plotted against trapping time. Our best devices operate along the uppermost curve, $\tau_t \approx 3$ μsec, $T \approx 0.30$ K. For devices in which spatial resolution is not important, the trapping time can be modified (either through interface transparency or through the absorber/trap volume ratio) in conjunction with the tunnel time to minimize recombination losses. It is evident from Figure 3.3.2, however, that recombination losses are not as sensitive to trapping time as they are to tunnel time and operating temperature. It is interesting to compare the two curves in the middle of Figure 3.3.2.

For very fast trapping, the lower temperature film exhibits higher losses, because the tunnel time is longer in this film, and, thus, quasiparticles reside longer in the Al trap. This is consistent with the data presented in Figure 2.2.2. For longer trapping times, the quasiparticle population does not build up in the trap, so background thermal recombination dominates self recombination. In this case, the lower temperature gives lower losses, even with the longer tunnel time.

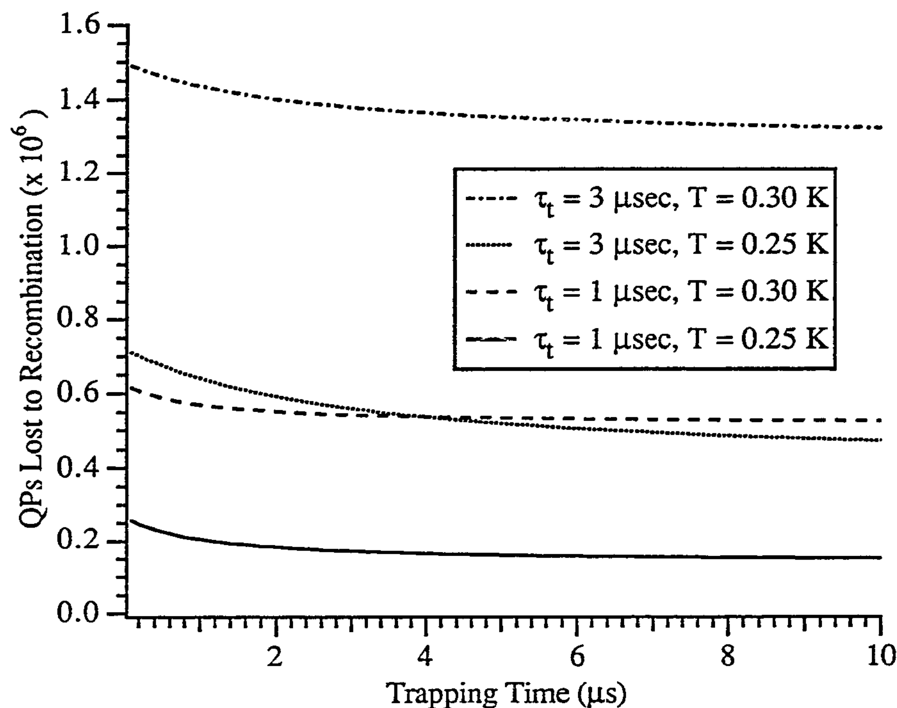

Figure 3.3.2: Total quasiparticle recombination losses as a function of trapping time from Ta to Al. Initial $N_X = 5 \times 10^6$ in the Ta. Assumes no losses in Ta, and no phonon trapping effects in the Al. Al film volume = 850 μm^3.

3.4 Increased Signal Due to Bandgap Engineering

The simple device of Figure 2.2a will deliver a charge (ignoring quasiparticle losses) of $\approx \eta E_X/\Delta_{Ta}$, where η is the fraction of x-ray energy converted into quasiparticles, and Ta is the x-ray absorbing film. Bandgap engineered structures, however, can deliver more charge because of the presence of a lower bandgap material. A certain fraction of the energy in the initial x-ray hotspot will be released as phonons with energy $2\Delta_{Al} < \Omega < 2\Delta_{Ta}$. Because such phonons cannot break Ta

pairs, they can travel long distances in the Ta. If the phonons make it to the Al trap, they can break pairs, resulting in an increased charge output.

Another mechanism exists for charge multiplication when the absorbing film's gap is greater than three times the trap film's gap.[Booth, 87] Relaxation phonons emitted by the quasiparticle in the trap can have enough energy to break Cooper pairs in the trap, and will thus give some quasiparticle multiplication. This effect has been explicitly verified for high energy quasiparticles injected in Nb–Ta structures,[Warburton, 93] and should also be relevant for our Ta–Al devices.

3.4.1 Ta Subgap Phonons

In section 2.2.1, it was indicated that approximately 40% of the initial x-ray energy resides in $\Omega < 2\Delta_{Ta}$ phonons immediately after the dissipation of the hotspot. Because $\Omega < 2\Delta_{Ta}$ phonons in Ta are not absorbed by Cooper pairs, they decay very slowly [Gaitskell, 93], and interact rarely with electrons [Kaplan, 76], their lifetime can be quite long. They will most likely escape to one of the materials in contact with the Ta absorber: the Nb wiring, the Al trap, the SiO insulation layer, or the SiO_2 substrate (see Chapter 5 for a complete description of the device). If the phonons enter the Al trap, the short pair-breaking time in Al will ensure that a significant fraction of phonons produce quasiparticles from Cooper pairs.

This effect will lead to collected charge in excess of that collected from a Ta film alone, but will actually broaden the energy resolution. Because of the nonzero probability that the subgap phonons will escape to films other than the trap, an absorption position dependence results. X-ray absorptions farther away will dump their phonons into the substrate before they make it to the trap. Absorptions closer to the trap will give a larger amount of charge. (Note that the phonon transmissivity from Ta into Al should be a factor of ≈ 2 greater than from Ta into SiO_2.[Kaplan, 79]) This is all complicated by the effect of high energy quasiparticles diffusing close to the trap, then emitting relaxation phonons into the trap. In this way, even absorption events far from the trap can dump some $2\Delta_{Al} < \Omega < 2\Delta_{Ta}$ phonons into the trap. Experimental tests confirm that this is likely the case: in Pb–Sn–Al devices, Kraus [94] observes such phonon effects from x-ray absorptions in the Sn as far as 30 μm away from the Al trap. Our experiments on Ta – Al structures show evidence of this phonon effect for absorptions more than 50 μm away from the trap (see Chapter 7). With the phonon transmission coefficient from Ta to SiO_2 being as large as 0.25 [Kaplan, 79], one would not expect the $\Omega < 2\Delta_{Ta}$ phonons to travel far in the Ta to the trap without being lost to the substrate. Of course, once in the substrate, the

phonons might be able to re-enter the superconducting films before decaying (see Section 5.1).

This excess charge is somewhat unpredictable, and will lead to a broadening of the energy resolution. One cannot use a position sensitive structure such as Kraus' [89] double junction device to deconvolve the effects of the excess phonons because there will be a dependence on the absorption height in addition to the dependence on distance from the trap. That is, absorptions in the Ta film which take place close to the substrate will lose more of their phonons to the substrate than absorptions which occur near the top of the Ta film. The double junction device can only account for lateral position variations, not such vertical position variations.

The solution to this problem is to eliminate or greatly reduce absorption events which generate $\Omega > 2\Delta_{Al}$ phonons in the trap. One relatively simple means of achieving a reduction in these unwanted absorptions is to reduce the thickness of the Ta layer within $\approx 30\ \mu m$ of the trap, as illustrated in Figure 3.4.1a. Relatively few absorptions will occur near the trap because the Ta thickness is much less than the absorption depth, and phonons created from events more than 30 μm away will have a high probability of scattering into the substrate before making it to the trap. The trap might need to be extended laterally, if the gap in the proximity enhanced Al trap is high enough to significantly slow the quasiparticle inelastic scattering process. A thick dielectric coating might be used to prevent low energy x-ray absorptions in the thin Ta region. Such a dielectric coating might also be beneficial in removing some of the $\Omega > 2\Delta_{Al}$ phonons from the trap film. Note also that the Nb wiring contact is placed more than $\approx 5\ \mu m$ from the thick, high absorption efficiency Ta region, to ensure that only Ta quasiparticles of energy less than Δ_{Nb} sense the Nb (see Section 3.2). Experimental studies must be performed to evaluate the effectiveness of this design.

A more reliable, if less elegant, solution is the use of a mask above the device to prevent any absorptions in a region near the trap. Au or Pt films have absorption depths even smaller than Ta, and can thus form reasonably effective masks in thin film form. Such films can be deposited on an insulating film which covers much of the device, masking off the absorber within $\approx 30\ \mu m$ of the trap, the trap, and the substrate. Subgap phonons would have large insulating and normal metal films in which to downconvert to $\Omega < 2\Delta_{Al}$. Again, note that the Nb wiring is several microns away from the active Ta absorbing region. Both of the designs presented in Figures 3.4.1a and 3.4.1b will also help in ensuring that the quasiparticles which enter the Al trap will have been thermalized close to the Ta gap edge, thus removing

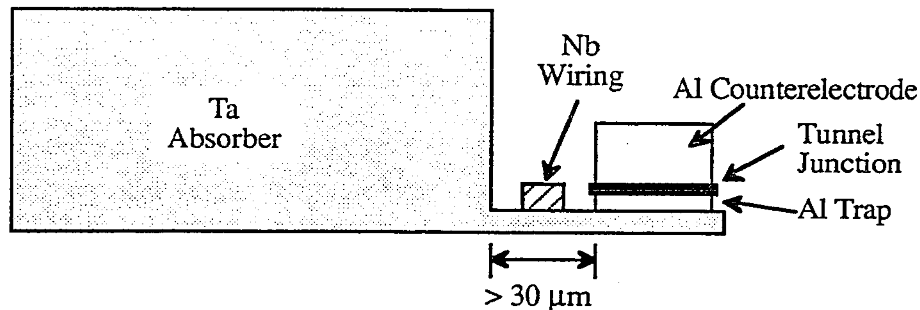

Figure 3.4.1a: Possible device for reducing Ta subgap phonon production of quasiparticles in the trap (side view).

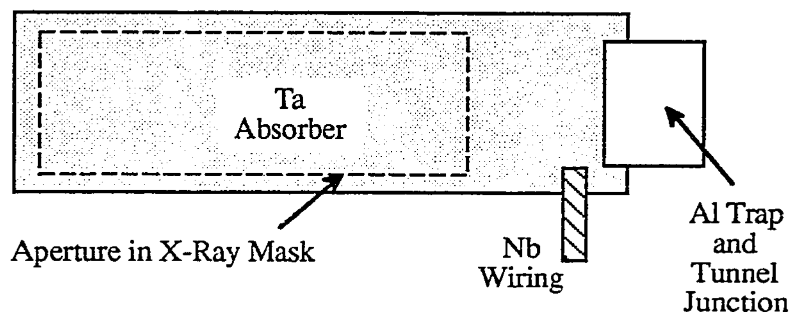

Figure 3.4.1b: Possible device for masking of absorption events near the trap to reduce Ta subgap phonon production of Al quasiparticles (top view).

the energy resolution broadening effects of high energy quasiparticles involved in the trapping process.

Some simple attempts at masking the trap region in this work were performed using a thick copper foil held in place above the trap. This method of masking did prove somewhat successful, although not desirable as a long term solution (e.g. for two dimensional arrays which will fly on a satellite).

3.4.2 Multiplication upon Trapping

The energy difference between the gaps in Ta and Al is ≈ 700 μeV – 175 μeV = 525 μeV. Relaxation phonons emitted upon trapping will therefore have energy 0 <

$\Omega < 525$ μeV (assuming the quasiparticles in the Ta have thermalized to the gap edge). The fraction of phonons with energy $\Omega > 2\Delta_{Al} \approx 350$ μeV will be able to break pairs in the Al trap. Figure 3.4.2 illustrates the pair breaking process schematically. Phonons of energy $2\Delta_{Al}$ will have a pair breaking time of $\approx 2.4 \times 10^{-10}$ sec, and phonons with the maximum ≈ 525 μeV will pair break approximately 1.25 times faster.[Kaplan, 76] Based on the acoustic coupling to the substrate (Section 2.2.3), approximately 20% of the $\Omega > 2\Delta_{Al}$ phonons will break pairs in the Al before escaping into the substrate.

Some calculations of the energy distribution of these relaxation phonons have been reported.[Eisenmenger, 81] Due to the complicated expressions for the electron-phonon interaction, the phonon density of states, and the quasiparticle density of states, the calculations are somewhat involved, and will not be discussed here. Based on these calculations, we can assume, without gross error, that the phonons have an approximately flat energy distribution from 0 to $\Delta_{Ta} - \Delta_{Al} \approx 525$ μeV. This implies a fraction $\approx 33\%$ of the relaxation phonons will have sufficient energy to break Al Cooper pairs. Assuming $\approx 80\%$ of the phonons escape to the substrate, we find $\approx 6\%$ of the Ta quasiparticles will create two more quasiparticles as they trap in the Al. One thus calculates a quasiparticle gain of ≈ 1.12 for our Ta–Al device. (Booth [87] has in fact proposed a variant of this device as a superconducting amplifier.)

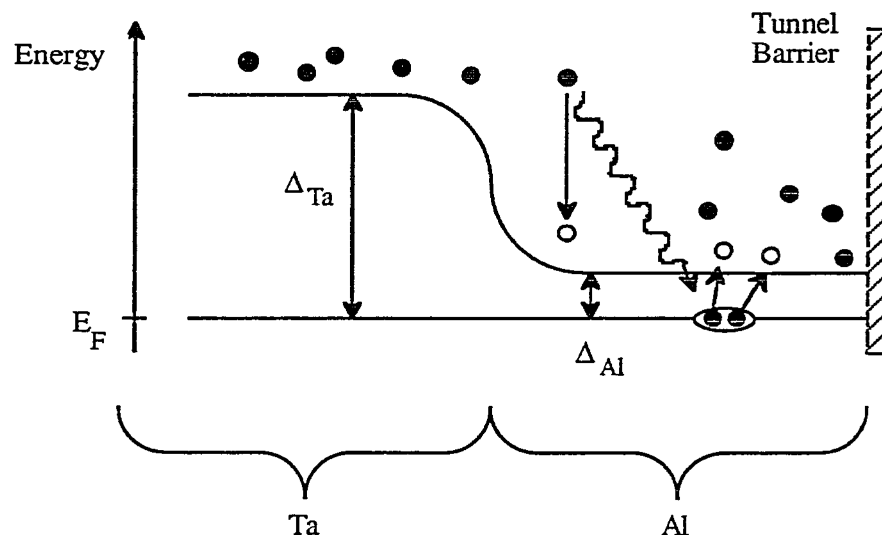

Figure 3.4.2: Quasiparticle multiplication from phonon emission in the trap.

Due to the statistical nature of the phonon generation and pair breaking processes, the excess quasiparticles produced by this effect will not improve upon the Fano-factor limited energy resolution. The fluctuations in the number of excess quasiparticles produced will combine with the fluctuations inherent to the quasiparticle generation at the x-ray absorption site to give a broader effective energy resolution. We have approximated the broadening of energy resolution due to the multiplication assuming the pair-breaking process obeys a binomial distribution. For $\approx$ 6.6% of the trapped quasiparticles breaking pairs, we calculate the excess broadening of energy resolution should be less than 2 eV. The broadening could be somewhat larger if the quasiparticles entering the trap are not all thermalized to the same energy (at the Ta gap edge), as the higher energy quasiparticles will be more likely to cause multiplication upon trapping. This effect will be reduced if the quasiparticles in the Ta have more time to thermalize before reaching the Al trap, as would be the case in the devices illustrated in Figures 3.4.1a and 3.4.1b.

Quasiparticle multiplication by this process is not necessarily damaging to the device's actual energy resolution. The signal to noise ratio can be improved by the gain factor ($\approx$ 1.12), if electronic noise from the preamplifier dominates the broadening of the device's intrinsic energy resolution. Mears *et al.* [93] use this technique to greatly increase the signal to noise ratio in Nb trilayer STJ detectors.

3.5 Discussion

Without quasiparticle trapping, it is unlikely that useful STJ x-ray detectors could be fabricated. The x-ray astronomers' need for high absorption efficiency and high energy resolution presents two requirements which likely cannot be simultaneously satisfied in a non-trapping device. A useful device with quasiparticle trapping can be made with moderately thick films of Ta forming high efficiency, low quasiparticle loss x-ray absorbers. These absorbers match well to thin Al traps and oxidized Al tunnel barriers, which give robust devices with good electrical performance.

The concept is quite simple, but the success of quasiparticle trapping depends a great deal on the device design parameters and fabrication techniques. Without adequate control of quasiparticle diffusion and interface transparency, one cannot control quasiparticle trapping. Without careful attention to the behavior of phonons in the device, one will find broadened energy resolution due to the presence of multiple gaps. But, with careful design and fabrication, superconductor bandgap engineering

becomes an effective, as well as essential, technique for creating useful x-ray detectors.

4. Electronic Circuitry

Of the three main amplifier types (charge, current, and voltage), the charge amplifier is clearly the desired choice for our application. Voltage amplifiers are impractical because of their high input impedance, which causes nonlinear response (Figure 2.1) and variation in quasiparticle tunnel time (Section 2.2.4) due to the shift in bias point on the junction subgap I-V curve. Conventional current amplifiers can be somewhat more noisy than charge amplifiers because bandwidth requirements force small values of feedback resistor.[Gatti, 84] SQUID current amplifiers are less noisy than conventional JFET current amplifiers only for detector resistances somewhat lower than 100 Ω. Also, because the *charge* is directly related to the input x-ray energy, one would integrate the output of a current amplifier anyway. Note, however, that current signals give more useful information for diagnostics of the detector device dynamics, as charge signals are one step removed from the device response by integration. In the following discussion, the focus is simply on the best performance for low noise, linearity, and good energy resolution -- the charge preamplifier.

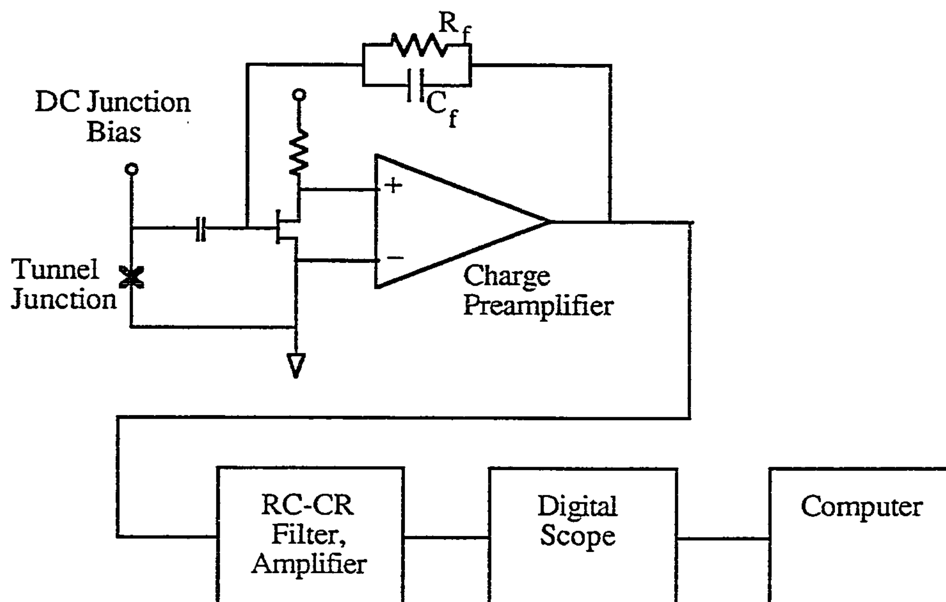

Figure 4: Block diagram of pulse detection electronics, with detailed preamplifier.

An overview of the electronic circuitry used with the STJ detectors in this work is presented in Figure 4. The charge preamplifier integrates the excess current which an x-ray induces in the tunnel junction. The preamplifier sends an output voltage, proportional to the x-ray produced charge, to a filter / amplifier (Tektronix 5A22N). The resultant pulse is then digitized and measured by a Hewlett-Packard 52510A digital oscilloscope, and recorded by an Apple Macitosh computer using National Instruments LabView software.

4.1 Charge Preamplifier

The conventional charge amplifier configuration is given in Figure 4.1, where the tunnel junction has been expanded, and the input FET has been hidden inside the op-amp. The DC junction bias circuit is simply represented by a current source (bias voltage through a large bias resistance), and will be discussed in more detail in section 4.2. The blocking capacitor prevents DC currents from entering the preamplifier; it is chosen large enough (1 μF) to be ignorable at x-ray signal frequencies. The tunnel

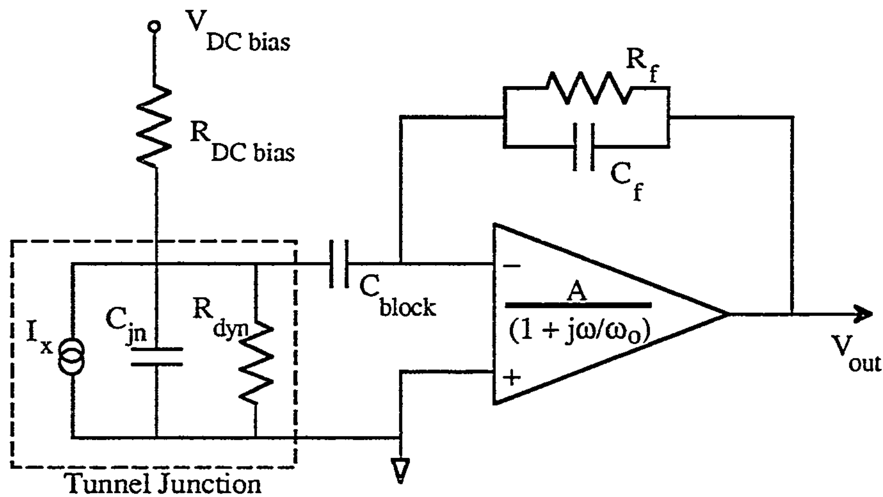

Figure 4.1: Schematic representation of a charge amplifier and tunnel junction.

junction is represented in this model by a junction dynamic resistance in parallel with a device capacitance (which includes the input capacitance of the amplifier), and a current source representing the x-ray induced quasiparticle current. A magnetic field is applied to suppress any important Josephson effects (section 4.2). The junction

dynamic resistance is defined as $\partial V_{bias}/\partial I_{bias}$ at the DC bias point in the subgap region. The tunnel barrier capacitance is approximately 40 $fF/\mu m^2$ for aluminum oxide junctions [Houwman, 90; Mayer, 91], or 60 pF for one of our typical devices, and the amplifier (and wiring) has capacitance ≈ 240 pF. The amplifier has DC open loop gain A with dominant pole at ω_o, thus giving the open loop gain for all frequencies as

$$A_{OL} = \frac{A}{1 + j\omega/\omega_o}.$$

Current induced by an x-ray absorption will ideally be collected on the feedback capacitance, C_f, giving an output voltage $V_{out} = -Q_x/C_f$, where Q_x is the total charge collected. For a typical C_f of 10 pF, this gives 16 nV per electron, or 6.25×10^7 electrons per volt. STJs deliver several million electrons, so the preamplifier output signal (10 - 100 mV) is large enough to feed directly into a good oscilloscope. The only pulse shaping performed is by a RC-CR bandpass filter in the oscilloscope input stage (Tektronix 5A22N). Future optimization of signal to noise ratio will utilize improved pulse shaping techniques.[see, e.g., Knoll, 89; Fairstein, 65]

The feedback resistor rolls off the integrating action of the amplifier at low frequencies, particularly to eliminate input bias currents from saturating the amplifier. With the use of a FET amplifier input stage, the feedback resistance can be chosen large enough such that one can neglect its effect on the noise of the amplifier. The R_fC_f time constant determines the low frequency rolloff, and must be chosen much larger than characteristic junction signal times such that full charge collection can occur before significant charge leaks off C_f.

4.1.1 Charge Amplifier Signal Response

Transfer Function

Figure 4.1.1a shows an equivalent circuit for the amplifier, where the bias circuitry and the blocking capacitor have been removed for simplicity. Polarities have been assigned to the currents such that the following analysis will follow more clearly, but these polarities do not necessarily indicate the actual flow of current during amplification of an x-ray pulse. Note that for positive I_x, the output voltage

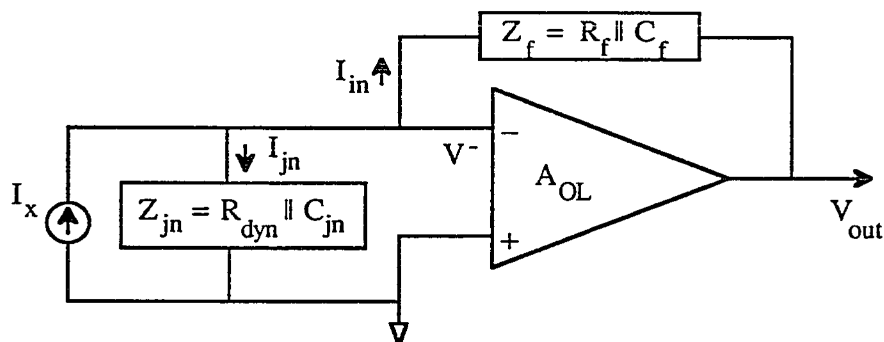

Figure 4.1.1a: Amplifier equivalent circuit for signal response calculations.

V_{out} is negative, and the inverting terminal voltage V^- is positive. V^- is nonzero because of finite open loop gain in the amplifier, and is given by

$$V^- = -V_{out}/A_{OL}.$$

Due to the presence of the junction and the feedback resistor, the signal response is not simply given by the ideal integrator equation

$$V_{out} = -\frac{1}{C_f}\int I_x\, dt = -\frac{Q_x}{C_f} \quad .$$

One must analyze the response of the amplifier in detail to determine the actual response of the amplifier,

$$V_{out} = -\frac{1}{C_f}\int I_{C_f}\, dt, \tag{4.1.1a}$$

which can differ significantly from the ideal equation above. Here, the integrand is the current which actually flows into (or out of) the *feedback capacitor.*

The input side of the equivalent circuit is shown in Figure 4.1.1b, simplified for calculating the current distribution. By Ohm's law, the inverting terminal voltage

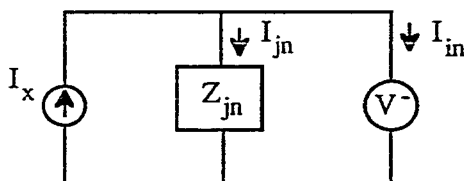

Figure 4.1.1b: Simplified input side of amplifier circuit.

restricts the current across the junction to be

$$I_{jn} = \frac{V^-}{Z_{jn}} = -\frac{V_{out}}{A_{OL} Z_{jn}} \quad .$$

By Kirchoff's law, we know the current into the feedback loop is

$$I_{in} = I_x - I_{jn} = I_x + \frac{V_{out}}{A_{OL} Z_{jn}} \quad .$$

Working explicitly in the imaginary frequency domain ($s = j\omega$), we have

$$V_{out}(s) = -Z_f(s) \cdot I_{in}(s) \quad .$$

With the above equations, we can solve for the transfer function:

$$\frac{V_{out}(s)}{I_x(s)} = -\frac{1}{\frac{1}{R_f} + sC_f + \left(\frac{1 + sR_{dyn}C_{jn}}{R_{dyn} \cdot A_{OL}(s)} \right)} \quad .$$

Plugging in for

$$A_{OL}(s) = \frac{A}{1 + s/\omega_o}$$

(A is the DC open loop gain), we obtain

$$\frac{V_{out}(s)}{I_x(s)} = -\frac{1}{\frac{1}{R_f} + sC_f + \left(\frac{1}{R_{dyn}A} + \frac{s}{\omega_o R_{dyn} A} + \frac{sC_{jn}}{A} + \frac{s^2 C_{jn}}{\omega_o A} \right)} \quad .$$

Inserting this equation into the transfer function allows us to identify terms which give linear gain (no factors of s), integrating action (one factor of s), and double-integrating action (two factors of s). Grouping terms, we have

$$\frac{V_{out}(s)}{I_x(s)} = -\frac{1}{\frac{1}{R_f^*} + sC_f^* + s^2 \frac{C_{jn}}{\omega_o A}} \quad , \qquad (4.1.1b)$$

where the effective feedback capacitance is now

$$C_f^* \equiv C_f + \frac{1}{\omega_o R_{dyn} A} + \frac{C_{jn}}{A} \quad ,$$

and the effective feedback resistance is

$$R_f^* = R_f \| (R_{dyn} A) = \frac{R_f R_{dyn} A}{R_f + R_{dyn} A} \quad .$$

Equation 4.1.1b allows one to estimate the rise or response time of our charge amplifier. The amplifier cannot respond quickly enough to behave like an integrator (instead behaving like a double integrator) at high frequencies. The cutoff frequency, or inversely, the amplifier risetime, is found when the last two terms in the denominator of Equation 4.1.1b are equated:

$$\tau_{rise}^{amp} \equiv \frac{C_{jn}}{C_f^* \omega_o A} \quad .$$

An intuitive feel for this expression can be realized by noting that the input impedance of the charge preamp looks resistive at signal frequencies (far above ω_o). This input resistance is simply $1/C_f^* \omega_o A$. The amplifier risetime is just the product of the input capacitance and the input resistance.[Gatti, 84] Our typical preamp runs with $C_f = 10$ pF, and $C_{jn} \approx 300$ pF (note that this capacitance includes that of the junction, the wiring, and the input stage of the preamp). This gives a risetime of about 1.5 nsec, much faster than any expected x-ray signal component (>> 100 nsec).

Pulse Shape

To proceed further with Equation 4.1.1b, it is helpful to understand the shapes of the x-ray induced current pulses. A typical current pulse and the integrated preamplifier output are shown in Figure 4.1.1c. (Note that because the amplifier is actually an inverter, the charge pulse will be of opposite sign with respect to the current pulse. We display the two pulses here with single polarity for ease in comparison.) The current pulse risetime τ_{rise} is generally set by the trapping time τ_{trap} to present the quasiparticles to the junction However, if τ_{trap} is greater than or comparable to τ_t or τ_r, the risetime will be shortened due to premature pulse decay.

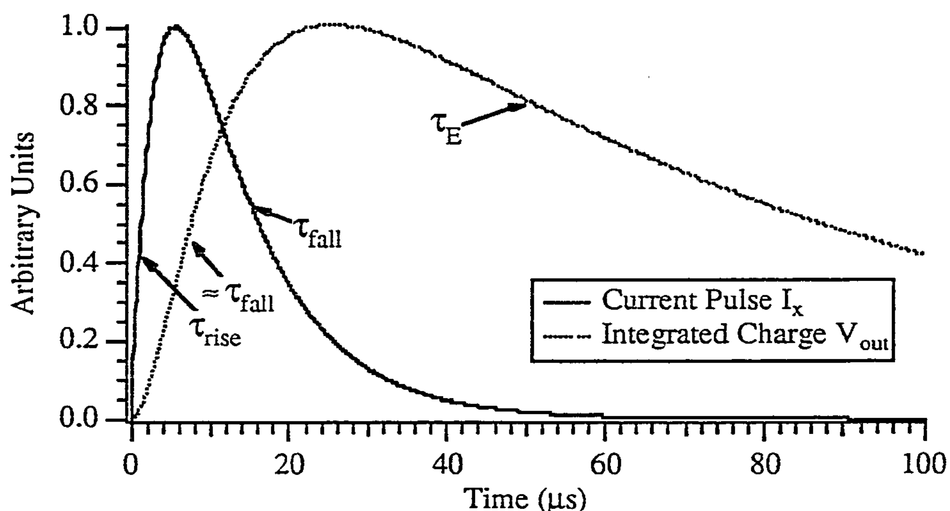

Figure 4.1.1c: Pulse shapes and definitions of characteristic times.

The current pulse waveform is found from solving the simple differential equation

$$\frac{\partial N_{trap}(t)}{\partial t} = -\frac{\partial N_{abs}(t)}{\partial t} - \frac{N_{trap}(t)}{\tau_r} - \frac{I_x(t)}{q} \quad ,$$

where N_{trap} is the number of quasiparticles in the trap, and N_{abs} is the number of quasiparticles in the absorber. For N_x x-ray generated quasiparticles, N_{abs} is given by

$$N_{abs}(t) = N_x \, e^{-t/\tau_{trap}} \quad .$$

Solving the differential equation for the current gives

$$I_x(t) = \frac{qN_x\tau_{loss}}{\tau_t\left(\tau_{trap} - \tau_{loss}\right)} \left(e^{-t/\tau_{trap}} - e^{-t/\tau_{loss}}\right) \quad , \qquad (4.1.1c)$$

where

$$\frac{1}{\tau_{loss}} \equiv \frac{1}{\tau_t} + \frac{1}{\tau_r}$$

is an effective loss rate of quasiparticles from the trap. Here, τ_r is the recombination lifetime in the Al trap, and it is assumed that recombination in the Ta absorber is negligible. Differentiating Equation 4.1.1c, we find that the current pulse will be at a maximum when

$$t = t_{max} \equiv \frac{\tau_{loss}\tau_{trap}}{\tau_{loss} - \tau_{trap}} \, ln\left(\frac{\tau_{loss}}{\tau_{trap}}\right) \quad .$$

The current pulse given by Equation 4.1.1c is not a simple exponential, but for $\tau_{trap} << \tau_{loss}$, the current pulse risetime τ_{rise} can be approximated by τ_{trap}. Our devices (X-N93, X-D94) typically exhibit current pulse risetimes of 2 to 3 μsec. Note that when $\tau_{trap} \approx \tau_{loss}$, the current pulse risetime will be somewhat faster than τ_{trap}. The I_x pulse decay time is similarly complicated, but can be approximated by

$$\tau_{fall} \approx \tau_{trap} + \tau_{loss} \quad .$$

This fall time is ≈ 10 μsec in our devices.

Signal Output

The preamplifier output V_{out} is, for short times, simply the integral of the input. Thus, the risetime of V_{out} will be approximately the falltime of the current pulse. For long τ_r and τ_E, the peak of the preamp voltage will be qN_x/C_f. The electronic time constant τ_E sets the decay time of the integrated pulse. For infinite open loop gain, τ_E is just R_fC_f. However, for finite open loop gain, Equation 4.1.1b gives $\tau_E = R_f^*C_f^*$, which can be somewhat different from R_fC_f. The idea here is that the nonzero voltage at the inverting node of the amplifier will cause current to flow

through the tunnel junction into the feedback loop, thus changing the time constant for decay. (This is discussed in detail below.)

We can now use the information regarding pulse shapes to convert the transfer function (Equation 4.1.1b) into the time domain. With Equation 4.1.1c, the x-ray generated current pulse in the frequency domain is

$$I_x(s) = I_o\left[\frac{1}{s+1/\tau_{trap}} - \frac{1}{s+1/\tau_{loss}}\right] ,$$

where we have defined

$$I_o \equiv \frac{qN_x\tau_{loss}}{\tau_t\left(\tau_{trap}-\tau_{loss}\right)} .$$

(Note that $q = -e < 0$.) Now, with the definition $\tau_f^* \equiv R_f^* C_f^*$, we have

$$V_{out}(s) = -\frac{I_o}{C_f^*}\left[\frac{1}{\left(s+1/\tau_{trap}\right)\left(s+1/\tau_f^*\right)} - \frac{1}{\left(s+1/\tau_{loss}\right)\left(s+1/\tau_f^*\right)}\right] ,$$

where the s^2 term in Equation 4.1.1b has been neglected. Laplace transforming this back into the time domain gives

$$V_{out}(t) = -\frac{I_o}{C_f^*}\left[\tau_{loss}^*\left(1-e^{-t/\tau_{loss}^*}\right) - \tau_{trap}^*\left(1-e^{-t/\tau_{trap}^*}\right)\right]e^{-t/\tau_f^*} ,$$

where we define

$$\frac{1}{\tau_{loss}^*} \equiv \frac{1}{\tau_{loss}} - \frac{1}{\tau_f^*} \text{ , and } \frac{1}{\tau_{trap}^*} \equiv \frac{1}{\tau_{trap}} - \frac{1}{\tau_f^*} .$$

(Note the *minus* signs in the above definitions.) The above equation is rather complex, and does not aid in an intuitive understanding of the problem. We can greatly simplify it by making the useful, if not strictly valid, assumption $\tau_{trap} \approx 0$. This allows us to understand the effect of the electronics on the integrated charge, while removing some of the complexities associated with the pulse shape. We thus obtain

$$V_{out}(t) \approx -\frac{I_o}{C_f^*}\,\tau_{loss}^*\left(1-e^{-t/\tau_{loss}^*}\right)e^{-t/\tau_f^*} . \qquad (4.1.1d)$$

This expression allows us to make several observations about the signal at the output of the charge amplifier. Comparing with equation 4.1.1a, we can identify $I_o\tau_{loss}^*$ as the integral of a constant current ($\approx qN_x/\tau_t$) from the x-ray for a time τ_{loss}^*. The remainder of the expression in Equation 4.1.1d simply modifies this understanding to account for the finite electronic decay time, and to scale the output voltage by the gain ($-1/C_f^*$). We can thus identify τ_{fall} in Figure 4.1.1c with τ_{loss}^*. (Note that $\tau_{loss}^* \approx$

τ_{fall} relies on $\tau_{trap} \approx 0$, which is likely not the case in our tunnel junctions, so τ_{fall} can actually be somewhat longer than τ^*_{loss}.) Also, the electronic decay time τ_E is identified with τ^*_f. For τ^*_f not much larger than τ^*_{loss}, significant reduction in peak output voltage can occur, so one must choose R_fC_f much longer than τ^*_{loss}. The full expression for τ^*_f reveals the need for large amplifier open loop gain and junction dynamic resistance as well:

$$\tau^*_f \equiv R^*_f C^*_f \approx \left(R_{dyn}A \| R_f\right)C_f + \frac{\left(R_{dyn}A \| R_f\right)}{\omega_o R_{dyn}A} .$$

To obtain the desired pulse decay time, $\omega_o R_{dyn}A$ must be large. We can consider three limits now: 1) when $R_f << R_{dyn}A$, 2) when $R_f >> R_{dyn}A$ and ω_o is large, and 3) when $R_f >> R_{dyn}A$ and ω_o is small.

In the first case, $R_f << R_{dyn}A$, the pulse decay will be somewhat *longer* than the simple R_fC_f. This can be explained by realizing that the pole in the op-amp's open loop gain makes it look like an integrator. Thus, the voltage appearing at the input terminals of the op-amp will be a scaled derivative of the output pulse. At the inverting input terminal, the voltage will actually cause excess current to flow *in* from the junction as the feedback capacitor discharges through the feedback resistor. The integrated pulse decay time constant is therefore lengthened.

In the second case, the pulse decay τ^*_f will be approximately $R_{dyn}AC_f << R_fC_f$. This is understood by realizing that for large ω_o, the op-amp actually looks like a linear gain element. The voltage appearing at the input terminals will be a fraction of the output voltage. At the inverting input terminal, the voltage will cause current to flow out through the junction from the feedback capacitor -- faster than current flows through the feedback resistor. Thus, the integrated pulse decay time will be shortened.

The third case is a mix of the first two. Because of the small ω_o, the op-amp exhibits a mix of character between a linear element and an integrating element. The integrated pulse decay time constant will be somewhere between $R_{dyn}AC_f$ and R_fC_f.

Perhaps more important than the time constants, however, is that the effective feedback capacitance can be significantly larger, for $\omega_o R_{dyn}A$ small. This will decrease the peak output voltage. Maximizing Equation 4.1.1d gives

$$V^{max}_{out} = -\frac{I_o}{C^*_f}\,\tau^*_{loss}\left[\left(1-\frac{\tau_{loss}}{\tau^*_f}\right)\cdot\left(\frac{\tau_{loss}}{\tau^*_f}\right)^{\tau^*_{loss}/\tau^*_f}\right] . \qquad (4.1.1e)$$

Using Equation 4.1.1e, we can estimate the effects of the electronic decay time on the measured pulseheight. An ideal pulse ($\tau_{loss} <<< \tau_f^*$) would give approximately

$$V_{out} = -\frac{qN_x}{C_f} \approx \frac{1.6x10^{-19} \cdot 5x10^6}{10^{-11}} = 80 \text{ mV}.$$

For the sake of discussion, we can take as representative values:

$\tau_{loss} \approx 10.00\ \mu\text{sec}$, and $\tau_f^* \approx 60.0\ \mu\text{sec}$,

resulting in a maximum output voltage of 46.59 mV. If, however, τ_{loss} for a different pulse is 11 µsec, the peak output voltage would instead be only 44.64 mV -- a 4.2% change! This corresponds to ≈ 250 eV (≈ per µsec change in τ_{loss}) energy resolution broadening for a 6 keV x-ray, and is thus extremely important in our devices. The data presented in Chapter 7 indicates that τ_{loss} for our pulses can differ by more than 1 µsec about a mean of ≈ 10 µsec. To eliminate this source of error, one must either lengthen the feedback time constant, or ensure that our pulses all have the same (or much faster) τ_{loss}. If we lengthen τ_f^* to 3 msec, for example, we obtain peak output voltages of 78.23 mV, and 78.08 mV, for τ_{loss} = 10 µsec and 11 µsec, respectively -- now only a 0.19% difference (≈ 11.5 eV per µsec). Figure 4.1.1d illustrates this energy resolution broadening as a function of τ_{loss}. Increasing τ_f^* is the most practical solution to the problem, but because of our limited base temperature and excess subgap current, the relatively low junction dynamic resistance limited τ_f^* to < 100 µsec. This is likely the most significant source of energy resolution broadening in our devices to date.

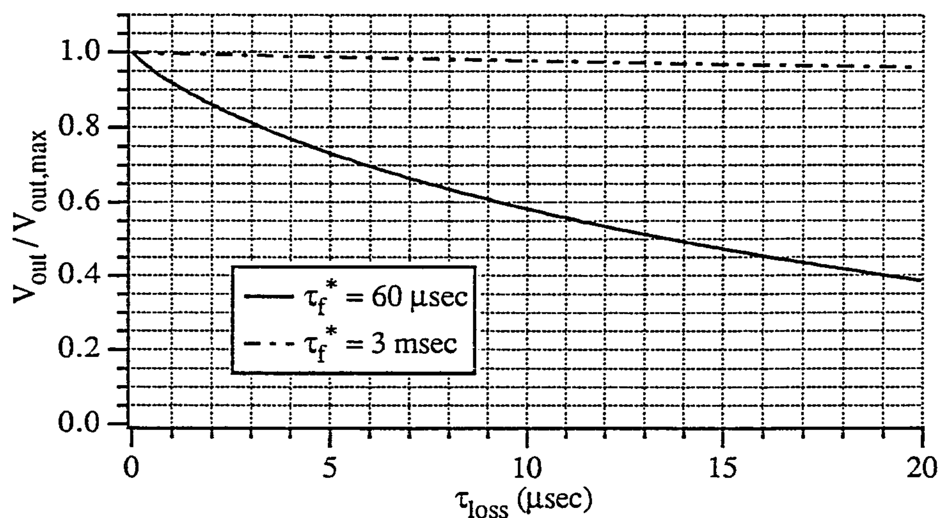

Figure 4.1.1d: Variation in output voltage with input current pulse length.

Note that longer τ_f^* will restrict the count rate somewhat, and should not be increased beyond a few milliseconds; otherwise, the flux from celestial sources might be too large for the detector to handle without some (undesirable) flux attenuation. Future devices could be designed for shorter τ_{loss}, to handle larger photon flux with shorther τ_f^*. It is important to realize that to obtain the very high resolution (0.1%) predicted for STJ detectors, common approximations must be scrutinized. Here we see that it is not good enough to ensure $\tau_{loss} << \tau_f^*$; we must have $\tau_{loss} <<< \tau_f^*$.

4.1.2 Electronic Noise in the Charge Amplifier

Figure 4.1.1a can be modified to include the various noise sources as shown in Figure 4.1.2a. The series noise voltage (squared) a comes from the amplifier's input transistor. In our amplifier, two Toshiba 2SK147 silicon JFETs are used at the

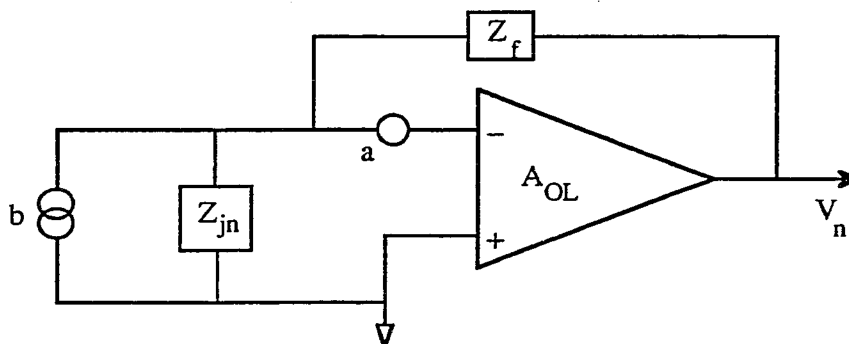

Figure 4.1.2a: Amplifier schematic with noise sources.

input stage, with a total transconductance g_m of about 40 mS. The noise power is given by [Manfredi, 85]

$$a = e_n^2 = 4k_BT\left(\frac{0.7}{g_m}\right)B \approx 2.9 \times 10^{-19}\ V^2/Hz\ ,$$

where B is the noise bandwidth. The parallel noise current (squared), b, arises from several sources: shot noise in the JFET gate current, $i_{n,FET}^2$; shot noise in the DC junction bias current, $i_{n,jn}^2$; thermal noise in the feedback resistor, $i_{n,Rf}^2$; and, thermal noise in the junction dynamic resistance, $i_{n,jn,th}^2$. The sum of these four terms gives b. The last two terms can be neglected, as the feedback resistor (10 MΩ) contributes only ≈ 1% to the total noise, and the junction thermal noise is expected to be quite low

due to the low temperature of operation and the presence of the superconducting bandgap. The JFET gate leakage current is listed by the manufacturer as less than 1 nA per JFET. The total shot noise in the two gates thus approximately 3.2 x 10^{-28} A^2/Hz. The DC bias current of a typical junction is ≈ 300 nA, giving a much larger shot noise of ≈ 9.6 x 10^{-26} A^2/Hz.

We ignore 1/f noise because we operate above the 1/f knee in our JFETs, and thus all noise sources can be assumed white. The parallel noise power can be converted to an effective series noise power by multiplying by the square of the parallel impedance seen from the inverting terminal, $Z_p^2 \equiv (Z_{jn} \parallel Z_f)^2$. We can then redraw Figure 4.1.2a into a simpler form, shown in Figure 4.1.2b.

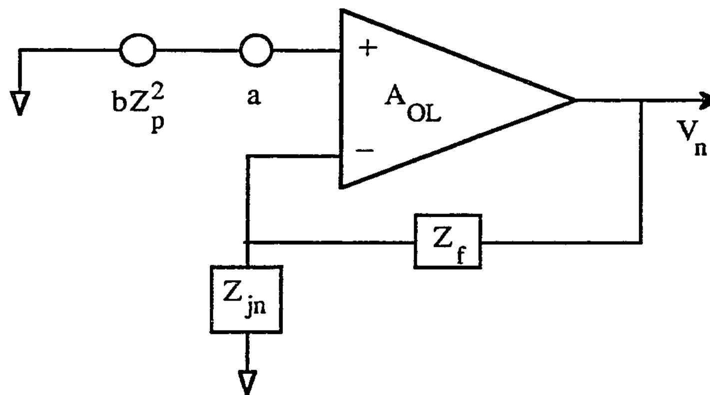

Figure 4.1.2b: Simplified noise model for charge amplifier.

From Figure 4.1.2b, we can immediately see the noise gain of the amplifier, and can integrate over the frequency range of interest to get the output voltage noise:

$$V_n^2 = \int df \left[a\left(\frac{Z_{jn} + Z_f}{Z_{jn}}\right)^2 + bZ_f^2 \right] . \qquad (4.1.2a)$$

The frequency limits are determined by the RC-CR bandpass of the oscilloscope input stage, 100 Hz to 300 kHz. The effective noise bandwidth [Frederiksen, 88] can be taken from 0 Hz to 470 kHz. Plugging in numbers for our junction (1 kΩ || 300 pF) and feedback (10 MΩ || 10 pF) gives the following:

$V_n \approx 275$ μV rms,

with approximately 50 μV of noise from the parallel term (b), and 270 μV from the series term (a). The relevant number for the spectral energy resolution, however, is the FWHM noise, ≈ 2.35 V_n ≈ 650 μV. For a relatively large signal of 5 x 10^6

electrons collected, the output voltage peak is approximately 80 mV, thus resulting in an energy resolution broadening of ≈ 50 eV. For the desired 10 eV resolution on 6 keV x-rays, we will eventually need $V_n \leq 55$ μV rms. From equation 4.1.2a it was found that the largest component of noise comes from the JFET series noise. There are two ways to reduce this noise component: 1) cool the JFETs to temperatures near 130 K, where the thermal noise of the electrons in the JFET channel is greatly reduced, or 2) reduce the noise gain $\left(Z_{jn} + Z_f\right)/Z_{jn}$ by increasing the effective impedance of the junction. At junction dynamic resistances of about 1 kΩ, the parallel capacitance of 300 pF is only marginally significant. The junction resistance can be increased most easily by lowering the operating temperature, and, with somewhat more difficulty, by altering the fabrication process with this specific goal in mind. Note also that reducing the temperature will lower the subgap current, thus reducing the shot noise contribution to the parallel noise term, b. The effective junction capacitance should be reduced only if the junction resistance is greater than about 5 kΩ. This can be done simply by moving the JFETs closer to the junction (as would be done to cool the JFETs), thus reducing the contribution from the wiring. The junction size can also be reduced, in line with general detector operating principles, to reduce its capacitance. And, finally, fewer or different JFETs can be used (note: the 2SK147 has a whopping 75 pF input capacitance). Reducing the noise gain must be approached with caution, however, as the amplifier stability depends critically on this parameter.

4.1.3 Stability of the Charge Amplifier

The need for very high open loop gain at relatively high frequencies imposes some difficult requirements on amplifier design. Combined with the need for low noise, these requirements can become even more difficult to satisfy, as the choice of devices is now severely limited. To date, low noise, fully compensated amplifiers simply do not have the bandwidth necessary for good signal collection efficiency. This leaves two options: either use a low noise, uncompensated amplifier, or use a composite amplifier (e.g., two amplifiers inside the feedback loop) with a low noise input stage. The uncompensated amplifier does not offer any significant advantage over the composite amplifier (other than using less circuit board space). Composite amplifiers, however, are quite flexible, and in this lies their advantage. The first stage can be a simple common source JFET, which can be located remotely from the second stage if desired. This is particularly useful if the JFETs are to be cooled. In

addition, the composite amplifier components can be chosen from a wide range of available amplifiers (even including uncompensated amplifiers), making it much easier to fine tune noise and gain parameters. We have adopted the composite amplifier approach because of these reasons.

As mentioned above, the input stage of the amplifier uses a common source JFET configuration with two paralleled 2SK147 silicon JFETs. These are chosen particularly for their low voltage noise and high transconductance. The drain resistor is 300 Ω, giving a first stage gain of 0.04 S x 300 Ω = 12. The second and final stage of the amplifier is an AMPTEK A250, basically a high gain op-amp without the input stage. Its gain is ≈ 300 at 1 MHz, with an approximately single pole rolloff. To maintain stablility in the amplifier, the closed loop gain must remain greater than 12 x 300/f_C, where f_C is the frequency (in MHz) at which the phase shift for the composite amplifier reaches 180°. This cannot be estimated from the A250 data sheet, but our experimental success tells us that for our high frequency closed loop (noise) gain of $\approx 1 + C_{jn}/C_f \approx 30$, the amplifier is stable. Thus, a 180° phase shift must not occur below ≈ 100 MHz. This analysis ignores all inductances, which is not valid for frequencies above about 10 MHz. The wiring from the junction to the preamp has a few hundred nH, and the rest of the circuit has negligible inductance. The wiring inductance will isolate the junction capacitance, and require that the amplifier is stable for noise gain of only $1 + C_{FET}/C_f \approx 20$, or, equivalently, the 180° phase shift cannot occur below ≈ 200 MHz.

The amplifier stability puts an upper limit on the feedback capacitance. For feedback capacitor values too large, the noise gain will not be large enough to ensure stability. The lower limit on feedback capacitance is set by the amplifier's open loop gain and the junction dynamic resistance. For feedback capacitor values too small, the input impedance of the preamp could be a significant fraction of the junction dynamic impedance, thus causing loss of the x-ray induced current signal through the junction. Additionally, small feedback capacitance can make it more difficult to obtain the long τ_E decay times necessary for > 1% energy resolution.

4.2 DC Junction Biasing

One cannot bias the tunnel junction at any arbitrary voltage in the subgap region; shot noise must be minimized by biasing at a low current, and the noise gain of the amplifier must be minimized by biasing at a large dynamic resistance. In addition, STJs are not simple devices to bias. The wide variety of Josephson effects

results in many negative resistance regions, and undesired steps in current.[Barone, 82] Ideally, a DC voltage bias would be preferable to a DC current bias because of the undesired tendency of a current bias to switch between multiple stable bias points. However, if the bias source presents a low impedance at high frequencies, voltage biasing can cause loss of charge signal into the biasing circuitry. A large inductor in series with the voltage bias might seem like a good idea, but often will have too large a parasitic capacitance, or will lead to resonant oscillations with the tunnel junction and the oscillation-prone charge preamplifier.[Fulton, 73; Buckner, 70] The current bias, conversely, is quite simple, and is the natural approach for this early stage of the research project, as there are ways to make it more stable.

4.2.1 Applied Magnetic Fields

The switching problems of the current bias can be greatly reduced by the application of a magnetic field parallel to the plane of the tunnel junction. A large enough field will quench any important Josephson effects, and present the current bias with only one stable operating point: that on the subgap region of the I-V curve. This is demonstrated in Figure 4.2.1; the magnetic field is applied parallel to the junction, causing a reduction in the critical Josephson current I_c at $V_{bias} = 0$. If the critical Josephson current is reduced below the intersection of the load line with the current axis, there will be only one stable bias point. The mechanism responsible

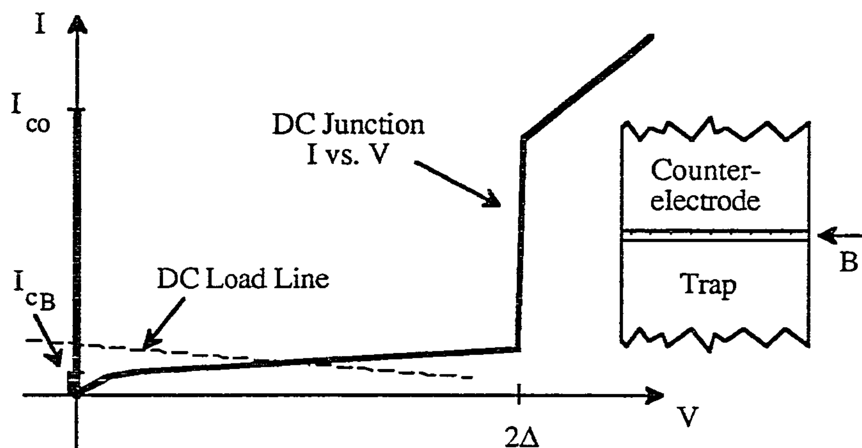

Figure 4.2.1: Applied magnetic field effects on tunnel junction DC biasing.

for the reduction in critical current is a modification of the phase of the Cooper pairs tunneling through the junction such that the phase varies spatially. At certain

magnetic fields, the pairs will destructively interfere, resulting in very low critical currents.[Van Duzer, 81]

One must be careful when applying magnetic fields to a superconductor, however, as they can weaken the superconducting state. Fields perpendicular to the tunnel junction, or to the other films in the device are particularly damaging. These fields have very complex effects on the critical current [Miller, 85; Gubankov, 92], and can cause excess subgap current at finite voltages, resulting in excess shot noise.[Fulton, 77; Uchida, 83; Golubov, 88] In addition, the vortices created in the superconducting films by such fields are regions of depressed gap, which can trap quasiparticles away from the junction. Thus, it is of utmost importance to accurately align the magnetic field parallel to the junction.

Although vortex formation is unlikely for fields parallel to thin films, these fields will weaken superconductivity by suppressing the superconducting gap. The reduction in the superconducting gap can result in a decreased quasiparticle lifetime. Calculations of the reduced lifetime [Holdik, 85] indicate that thin aluminum films at 0.3 K can exhibit lifetimes as short as $0.6\tau_{ro}$ in a 30 G parallel field, or $0.8\tau_{ro}$ in a 20 G parallel field, where τ_{ro} is the quasiparticle recombination lifetime for B = 0. The effect might be somewhat reduced in our films, as they are significantly thicker than the London penetration depth, so the superconducting gap will not be suppressed uniformly across the film. The regions of depressed gap will be at the edges of the film, and can serve to trap quasiparticles near the junction -- or on the other side of the film, away from the junction. The effect of parallel magnetic fields is certainly important, as experiments with Sn films [Holdik, 85] show qualitative behavior similar to the calculations, even for thick films. The magnitude of parallel field necessary to suppress the critical current is dependent on both the cross-sectional area presented by the junction to the field, and on the shape of the junction (as seen *perpendicularly* to the field). One can thus design the tunnel junction to require the minimum magnetic field for critical current suppression.

4.2.2 Tunnel Junction Shaping

A rectangular tunnel junction having uniform Josephson current density (Josephson penetration depth >> junction dimensions) will exhibit a $|\sin(\alpha B)/\alpha B|$ dependence on applied magnetic field, where α is a constant linear in L, the junction length as seen by the field.[Van Duzer, 81] Figure 4.2.2a shows a representative curve of I_c vs. B for a rectangular junction. By increasing L, the required magnetic

field to achieve the first zero in critical current will be reduced. The junction area can be kept constant if one decreases the junction width by the same factor. Thus, the most simple trick to reduce the required field is to make the junction long and narrow. (Section 4.2.3 will, however, dictate a limit on how long we will want to make the junction.)

By changing the junction shape (as opposed to just the dimensions), one can achieve extremely good sidelobe suppression as compared to the $|\sin(\alpha B)/\alpha B|$ pattern of a rectangular junction. This is important because in realistic junctions, spatial current density variations can prevent true zeros in the $|\sin(\alpha B)/\alpha B|$ pattern. Because of self-field effects or other nonidealities in the barrier, one often must bias the field at higher zeros of the I_c vs. B curve to achieve adequate suppression of the critical current.[Van Duzer, 81] Thus, even if the junction is made long enough to give a zero in the critical current at 2 G, it might be necessary to bias at 50 G or more.

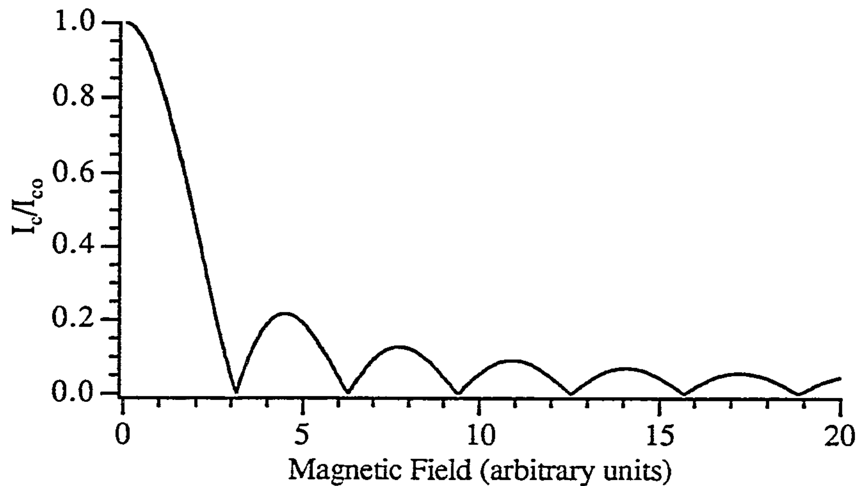

Figure 4.2.2a: I_c vs. B characteristic typical for a rectangular tunnel junction.

Theoretical calculations [Peterson, 91] and experimental investigations [Gaidis, 93; Houwman, 91] show that junctions with edges (viewed perpendicular to the applied magnetic field) given by a quartic shape result in extremely good sidelobe suppression. This shape of tunnel junction causes the I_c vs. B sidelobes to fall off like B^{-4} rather than the 1/B dependence of the rectangular junction. The quartic shape defines the juntion edges by

$$f(x) = y_o\,[1 + (c-3)x^2 + 2(1-c)x^3 + cx^4]\ ,$$

where y_o and c are constants, with c greater than or equal to -3, and the junction is symmetric about y = 0. Figure 4.2.2b shows representative junction shapes for the junctions discussed above.

Both techniques of junction shaping and stretching were used to some extent in our work. Data describing the I_c vs. B relation for our quartic tunnel junctions is given in Chapter 6. With these design techniques, we were able to stably bias below 10 G for 1500 μm^2 area tunnel junctions (Al-Al oxide-Al). Typical biasing fields were located at the third, fourth, or fifth minimum of the I_c vs. B curve -- although the zero-voltage current was adequately suppressed at the first or second minimum, adequate suppression of Fiske modes did not occur until higher fields were applied.

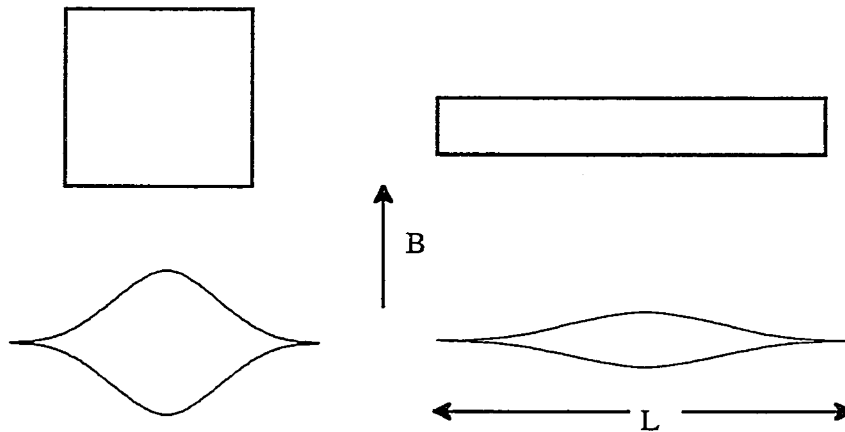

Figure 4.2.2b: Representative junction shapes. Clockwise from top left: square, rectangle, stretched quartic, standard quartic.

4.2.3 Fiske Modes

Upon application of a magnetic field parallel to a tunnel junction, stripline type (Fiske) resonance modes can exist inside the tunnel junction.[Fiske, 64; Swihart, 61; Eck, 65] Such standing waves couple with the Josephson current to give step-like jumps in current whenever the DC bias voltage resonates the Josephson current with the standing wave. For a simple rectangular junction, with field aligned perpendicular to a junction face, these voltages occur at

$$V_{Fiske} = n\frac{\hbar\bar{c}\pi}{2eL}, \qquad (4.2.3)$$

where n is any integer, $\bar{c}$ is the velocity of light in the junction cavity, and L is the junction length perpendicular to the applied field. For shaped junctions, the dependence of the resonance voltages on junction dimensions is less clear, but the lowest voltage resonance can be approximated by using the junction length L in Equation 4.2.3.

The resonances result in a steplike structure in the subgap I–V characteristic when a DC current bias is used. The resonances are actually peaks, as would be seen with a DC voltage bias. These steps cause excess current (and noise), and can result in unstable biasing, as switching between resonances can occur with current bias. The height of the current steps obeys a magnetic field dependence related to that which the zero-voltage Josephson current obeys (the Josephson current at zero voltage can be understood as a Fiske mode with $n = 0$). The magnetic field must thus be adjusted to suppress the zero-voltage Josephson current, *and* any low voltage Fiske modes which might interfere with the DC current bias stability. Because of the strict requirements that both Josephson current and Fiske modes be suppressed, the applied magnetic field will generally need to be larger than that used to suppress the Josephson current alone. The junction, however, can be designed small enough such that no Fiske modes will be present in the low voltage region desired for biasing the device as a low noise x-ray detector.

In Al-Al oxide-Al tunnel junctions, equation 4.2.3 indicates a Fiske mode at ≈ 90 μV for a junction length of 200 μm. In our 200 μm long quartic devices, one begins to see substantial current increase (and dynamic resistance decrease) at about 75 μV, and a minimum in dynamic resistance at about 90 μV, consistent with the above formula. This resonance reduces the dynamic resistance substantially at desired DC bias voltages (≈ 80 μV, based on shot noise, dynamic resistance, and preamp linearity considerations), and thus reduces the x-ray signal to noise ratio.

Some designs of our tunnel junctions used 100 μm lengths, to push the Fiske mode up to voltages far beyond where we might bias. This met with only marginal success, as a mode at ≈ 130 μV developed, presumably due to the non-rectangular shape of the device (i.e., a two-dimensional mode is likely present). I–V characteristics displaying such current steps are presented in Chapter 6.

With the above techniques, we were able to reliably use a current source to bias the tunnel junction. The current source is comprised of +9V and -9V batteries through a potentiometer and a 10 kΩ or 1 MΩ resistor. This gives continuous current adjustment from negative to positive values with minimal complexity. To guard

against preamplifier oscillation, the batteries for the DC bias were separate from the batteries used for the preamplifier.

4.3 Discussion

Future work on the DC biasing of the tunnel junctions must address the suppression (or elimination) of Fiske modes to ensure high dynamic junction resistances at the DC bias point. A DC voltage bias might offer some advantage over a current bias in this respect, as it might allow more stable biasing at voltages between the (zero voltage) Josephson current and the first Fiske mode (see the discussion in Section 6.2.2). Some relatively complex voltage source biasing circuits (transimpedance amplifiers) have been used at Yale, but appear to require magnetic field suppression of the pair currents to remain stable. DC circuit design in the near future will concentrate on improving the noise and stability of such voltage bias circuits.

The discussion in this chapter illustrates the failure of the ideal op-amp model in adequately describing our charge amplifier. The finite open loop gain of standard op-amps (and the low dynamic junction resistance) results in a nonzero voltage at the inverting input terminal, thus causing current to flow through the junction as well as in the feedback loop. As a result, energy resolution broadening of over 150 eV is likely -- simply due to this mechanism. Reducing this broadening does not appear excessively difficult, but since higher open loop gain is difficult to obtain while still maintaining amplifier stability, one must attempt to increase the dynamic junction resistance, or use a different type of amplifier. Faster current pulses will also reduce the broadening, but will probably require higher current density tunnel barriers, and will make it more difficult to obtain high dynamic junction resistance.

The noise of the preamp results in significantly less energy resolution broadening ($\approx$ 50 eV), but will need to be reduced in the future. The signal to noise ratio is degraded most by two factors: the input voltage noise of the input stage FET, and the noise gain of the amplifier. Again, increasing the junction dynamic resistance should help significantly here. Cooling the FET stage, and bringing it closer to the STJ device will also reduce the noise. It does not appear excessively difficult to bring the noise below $\approx$ 10 eV in the near future.

5. Device Design and Fabrication

As illustrated in Figure 5, our STJ x-ray detector is a very complex device. (An expanded view of the trap and tunnel junction region is presented in Section 5.4.) The Yale group's STJ device fabrication experience has allowed us to optimize nearly every aspect of the processes involved within a STJ detector. Because of its flexibility and accurate control of pattern dimensions, photolithography is used to

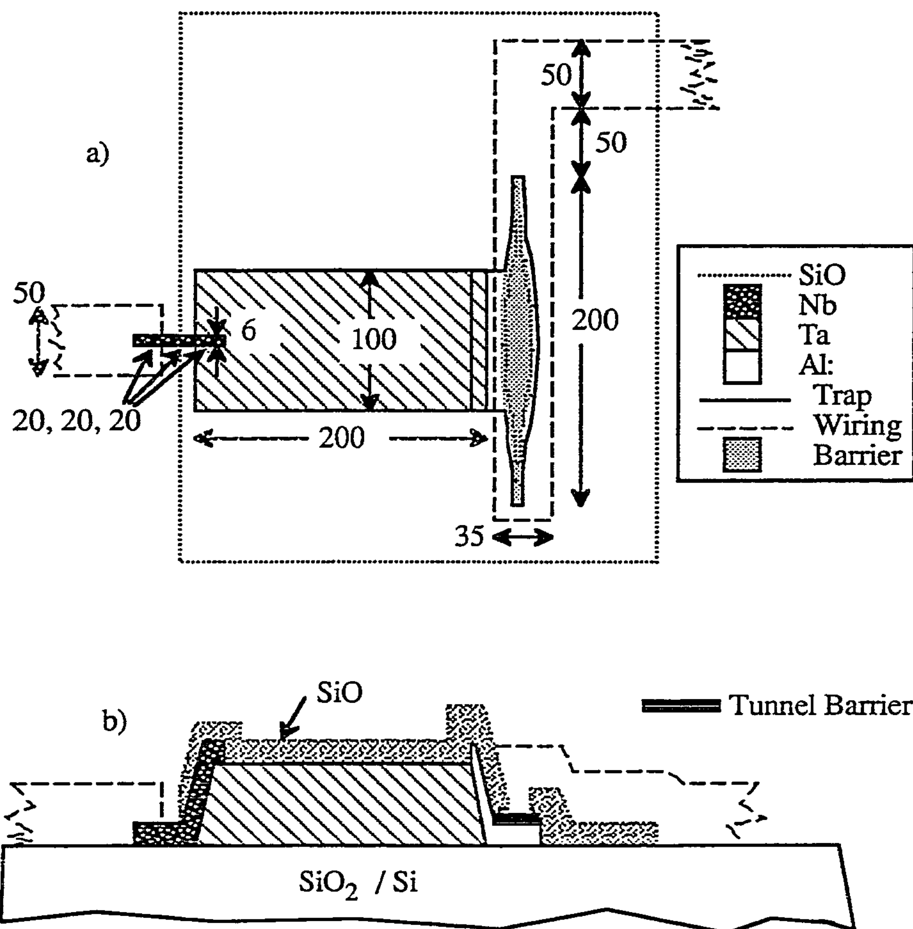

Figure 5: The specific device design used for most of this work's STJ x-ray detectors. All dimensions in microns. Film thicknesses are approximately: 6000 Å Ta; 1500 Å Nb; 1500 Å SiO; 2000 Å Al trap; 700 Å Al counter-electrode; and 4000 Å Al wiring. Top view (a) and side view (b). An expanded view of the trap region is presented in Section 5.4.

define all device geometries. With our device design, we have addressed each of the "important processes" covered in Chapter 2, the "detector requirements" and bandgap engineering discussed in Chapter 3, and the DC and high frequency device electrical performance covered in Chapter 4. In this chapter we describe the specific device design in detail, and mention a few more design techniques which were, or soon will be, implemented to make the device more effective. The reasons for choosing the materials and geometries for the device are discussed below, along with specific fabrication techniques used or developed in this work. The complete fabrication procedure is detailed in Appendix 1, and some specific issues related to device fabrication are dicussed in Chapter 6.

5.1 The Substrate: SiO_2 / Si

The substrate beneath the tunnel junction films plays a surprisingly important role in determining the device's energy resolution. One must be concerned particularly with phonon transmission from the superconducting films to the substrate, and from the substrate to the superconducting films. Because phonons can travel from the superconducting films into the substrate, x-ray energy absorbed by a superconducting film can be lost to the substrate, reducing the detected quasiparticle signal. X-ray absorptions in the substrate can send pair-breaking phonons into the superconducting films, resulting in a quasiparticle signal. The strength of this signal will depend on the proximity of the x-ray absorption to the films. Thus, the substrate absorption signals continuously span the entire energy range of observation, but will more commonly result in small signals (simply because of the larger substrate volume available at larger distances from the device). These signals are difficult or impossible to distinguish from x-ray absorptions in the actual superconducting films, and can thus result in a background which masks the low energy x-ray peaks.

With these and other concerns in mind, the ideal substrate should

1) be readily available and inexpensive,
2) be useful for high quality, uniform superconductor film growth (possibly at elevated temperatures),
3) thermally cycle between room temperature and 0.3 K without deformation or severe stress to the superconducting films,
4) passivate the superconductor film surfaces to prevent depressed gap regions and related quasiparticle losses,
5) form superconductor film – substrate interfaces opaque to quasiparticles and selectively opaque to different energy phonons,

6) possibly be micromachinable.

While it will be impossible to find a substrate to ideally satisfy all requirements, we find that thermally oxidized silicon substrates adequately satisfy the majority of the above characteristics.

Silicon is of course widely available, and low resistivity, <100>, polished 2" substrates, ≈ 12 mils thick (the match to our deposition equipment) can be found for less than $5 each (Virginia Semiconductor Corp.). The silicon wafers are oxidized at Yale in a wet furnace to give ≈ 3000 Å of amorphous SiO_2 at the substrate surface. As described in Section 5.2, these substrates allow growth of high quality sputtered Ta films at ≈ 700° C. Our devices have been thermally cycled between 0.3 K and room temperature as many as 10 times without any evidence of device degradation. The devices have been stored for more than 1.5 years at room temperature in ambient air without any noticeable film or device degradation as well.

While no explicit tests have been performed to judge the effectiveness of the substrate in passivating the superconductor films at the substrate - film interfaces, the high charge output for a 6 keV x-ray in our devices (see Chapter 7) indicates that any quasiparticle losses at the substrate–film interfaces are minimal. SiO_2 is a very effective insulator, and will not allow quasiparticle transmission from the superconducting films into the substrate. However, phonon transmission between the films and the substrate is possible, in at least three particularly important cases: $\Omega > 2\Delta_{Ta}$ phonons leaving the superconductors, $2\Delta_{Al} < \Omega < 2\Delta_{Ta}$ phonons leaving the superconductors, and $\Omega > 2\Delta_{Al}$ phonons produced in the substrate, entering the superconductors.

$\Omega > 2\Delta_{Ta}$ Phonons

Ideally, the interface would not allow $\Omega > 2\Delta_{Ta}$ phonons to travel from the superconducting films into the substrate. The loss of such phonons from the Ta absorber film creates a STJ signal dependent on the x-ray's absorption height within the Ta film. X-rays absorbed in regions of the Ta film closer to the substrate will lose more high energy phonons to the substrate during the hotspot expansion, and will thus produce fewer quasiparticles. This absorption height dependence gives varied signal amplitudes for the same x-ray energy input, thus broadening the energy resolution. We are optimistic, however, that the poor phonon transmission from Ta to SiO_2,[Kaplan, 79] and the fast phonon pair breaking time in Ta [Kaplan, 76] will result in very little energy loss via this process. Future tests will be performed on

devices with various thicknesses of Ta absorbers, and with various energy x-rays, to determine the importance of energy resolution broadening due to this process.

$2\Delta_{Al} < \Omega < 2\Delta_{Ta}$ Phonons

Ideally, the interface would be perfectly transparent to $2\Delta_{Al} < \Omega < 2\Delta_{Ta}$ phonons, and the underlying substrate would cause rapid anharmonic decay of these phonons before they could re-enter the superconducting films. This ideal substrate would return STJ signals independent of the x-ray's lateral absorption position (Section 3.4.1). Amorphous SiO_2 is known to exhibit relatively strong inelastic phonon scattering for $\Omega > 2\Delta_{Al}$, but the mean free path of such phonons in SiO_2 is likely several times the thickness of our thermally grown SiO_2.[Dietsche, 80] Thus, the interfaces created around the SiO_2 might exhibit more influence on the phonons than the SiO_2 film itself. Our STJs apparently exhibit a significant response to these $2\Delta_{Al} < \Omega < 2\Delta_{Ta}$ phonons (see Section 7.3), but it is not yet clear if these phonons enter the substrate before they break pairs in the Al. High energy Ta quasiparticles can diffuse in or near the trap, emitting relaxation phonons directly into the trap, and bypassing the substrate alltogether. If, however, the STJ response is due to phonons which enter the substrate and then reenter the trap, it does not appear that the substrate is very effective in downconverting the phonons or in preventing the phonons from reentering the Al trap. We therefore rely primarily on the masking techniques described in Section 3.4.1 to control the energy broadening due to $2\Delta_{Al} < \Omega < 2\Delta_{Ta}$ phonons. The masking techniques should prevent the above mechanisms from delivering $\Omega > 2\Delta_{Al}$ phonons to the trap.

$\Omega > 2\Delta_{Al}$ Substrate Phonons

Ideally, the interface would be perfectly opaque to all phonons generated by absorption events in the substrate. Such an interface would remove any substrate events from the data. The Al films will be sensitive to the substrate phonons because of the low Al energy gap, and the Ta films will be sensitive because of the high probability of phonon pair-breaking (Section 2.2.3). Unfortunately, most useful substrates couple phonons relatively well into Al and Ta, so highly opaque interfaces are not realistic. More practical is a substrate which induces downconversion of phonon energy so only $\Omega < 2\Delta_{Al}$ phonons will enter the superconducting films. Because single crystal substrates such as Si and Al_2O_3 perform poorly in this respect,[Kraus, 91; Rando, 93; Hebrank, 93] we have adopted an approach which uses an *amorphous* thin SiO_2 film at the surface of the relatively thick Si substrate.

Hopefully, this film, or the extra interface it creates, will cause rapid phonon scattering -- elastic *or* inelastic.

Used to disrupt ballistic phonon propagation, elastic scattering can be benficial in reducing the STJ signal from substrate absorptions. The TUM group [Peterreins, 88; Probst, 89] studied STJ signals resulting from substrate absorptions. The largest such signals come from ballistic phonons generated at absorption positions in a phonon focussing direction. An elastic scatterer in the path of these fast ballistic phonons will redirect the phonons, giving them more time to decay before they reach the superconductor films. Since $\Omega > 2\Delta_{Al}$ phonon wavelengths are of order 100 Å, a 3000 Å thick film of amorphous SiO_2 (and/or its interfaces) should have some scattering effect on these phonons.

If there is inelastic scattering as well, phonons can be downconverted to $\Omega < 2\Delta_{Al}$, rendering them virtually invisible to our superconducting films. As mentioned in the previous section, it appears inelastic scattering might not be fast enough to downconvert $2\Delta_{Al} < \Omega < 2\Delta_{Ta}$ phonons. However, higher energy phonons will scatter more quickly (inelastically, as Ω^5, and elastically as Ω^4 [Kraus, 91]), and thus will be influenced more by the SiO_2 film. For these high energy phonons, the amorphous SiO_2 can result in effective downconversion, and disruption of phonon focussing.

Our experimental results (Chapter 7) show that 6 keV x-rays absorbed in the substrate give signals more than a factor of 10 lower than Ta film absorption signals, a significant improvement over the single crystal substrates used by others.[Rando, 93; Hebrank, 93] Thus, some combination of the elastic and inelastic phonon scattering caused by the amorphous interface appears useful in reducing background counts in the energy spectrum. Even with these encouraging results, it is not entirely obvious that SiO_2 / Si films are the best substrates to use. Some x-ray masking technique or an improved substrate will still be necessary to keep substrate events from overwhelming the very low (< 600 eV) energy x-ray peaks.

Micromachined Si less than 2 μm thick, with 1000 μm^2 area has been used as a substrate for STJ detectors,[Lemke, 93] and might provide solutions to two of the three major interface problems. The number of x-ray absorptions in the substrate will be negligible for such thin substrates, so phonons entering the superconductors will not be a significant problem. In addition, $\Omega > 2\Delta_{Ta}$ phonons which leave the Ta film will re-enter the film within nanoseconds, likely without downconverting. Some problems still remain with such substrates, however. Because they cannot be made

infinitely large, there can be a signal dependence on lateral x-ray absorption position due to phonon escape to the thick (supporting) portion of the substrate. Also, there is no fast mechanism for removing $2\Delta_{Al} < \Omega < 2\Delta_{Ta}$ phonons. Because of this difficulty in phonon removal, DC bias self-heating in the device can become troublesome as well. Finally, the extra complexity involved in substrate micromachining erases one advantage STJs hold over microcalorimeters -- ease of two dimensional array fabrication. This extra complexity and the potential problems with phonon escape/removal have kept us from using such substrates in our work to date.

5.2 The X-Ray Absorber: Ta

As alluded to in the first three chapters, Ta is our choice for the x-ray absorbing superconductor film. It has the shortest x-ray absorption depth of any convenient T_c superconductor (Section 3.1). It is a refractory material which thermally cycles well. Its bandgap is intermediate among common superconductors, making it useful for superconductor bandgap engineering with higher gap wiring and a lower gap trap. Tantalum's electron-phonon coupling characteristics make it one of the better performing superconductors regarding hotspot dissipation. In addition, quasiparticle recombination losses are expected to be minimal because of phonon trapping and the low operating temperature. Ta surfaces are well passivated by oxygen,[Face, 87] without metallic suboxides like those observed on Nb surfaces,[Halbritter, 87] and expected on V surfaces.[Reed, 71] These metallic suboxides will have depressed gap, possibly forming quasiparticle loss centers. Perhaps the only drawback to using Ta is the difficulty in obtaining high purity, single phase films with large diffusion constants.

5.2.1 BCC Ta Film Growth

Ta thin films can be produced with two different crystallographic phases, each possessing very different electrical properties. The tetragonal (β) phase of Ta has a room temperature resistivity of $\approx$ 150 $\mu\Omega$-cm, and a superconducting transition temperature of $\approx$ 0.5 K.[Read, 65] The more desirable phase of Ta for our x-ray detectors is bcc, with room temperature resistivity of $\approx$ 14 $\mu\Omega$-cm, and transition temperature of $\approx$ 4.4 K.

It is generally found that for low temperature deposition (< 300° C), Ta films are stabilized in the β phase by oxygen or OH on the substrate surface.[Feinstein, 73; Hieber, 82; Sato, 82] Amorphous SiO_2 substrates generally form β–Ta for nominally room temperature despositions. We experimented with the use of a thin (< 50 Å) Nb [Face, 83; Face, 89] or a thin Al underlayer depositied less than two seconds before the Ta film. Each of these techniques resulted in bcc Ta ($T_c \approx 4.4$ K), but with RRR always below 10.

For x-ray detectors, one requires very clean Ta for a long quasiparticle diffusion length, and good surface passivation to prevent quasiparticle losses. To increase the RRR (and thus the diffusion length), and to eliminate possible low gap absorber–substrate interfaces, we utilized elevated temperature Ta deposition. Our research finds that for deposition temperatures above ≈ 400° C, the Ta films will form in the bcc phase on amorphous SiO_2 / Si substrates, as determined by resistivity and T_c. Higher RRR is obtained for higher temperature deposition. Our maximum heater temperature is ≈ 700° C, for which we obtain RRR ≈ 20 on amorphous SiO_2 / Si substrates. This corresponds to a quasiparticle diffusion constant D ≈ 500 cm^2/sec (mean free path ≈ 1100 Å).

The lamps used to heat the substrate during deposition illuminate only a ≈ 2" diameter spot, the same size as the substrate. One therefore sees various effects from nonuniform heating of the substrate, such as peeling or cloudiness of the film. To reduce this problem, the substrate holder is coated with a ≈ 0.5 μm SiO film, and a 2 inch diameter, 1/8 inch thick polished stainless steel disk is placed between the substrate and the lamps. This appears to keep the substrate edges close to the temperature of the substrate center. We have not performed any thorough tests of the actual substrate temperature during depositon; the value quoted above is from thermocouples placed near the lamps. However, it has been verified that the sample attains temperatures high enough to melt aluminum ($T_m \approx 660°$ C).

The background pressure is ≈ 3 x 10^{-7} torr at the elevated deposition temperature, mostly water and nitrogen. To minimize such impurity incorporation into the Ta film, we sputter deposit the Ta at ≈ 40 Å/sec. An ion beam cleaning of the amorphous SiO_2 / Si substrate is performed ≈ 5 minutes prior to the Ta deposition, primarily to remove any foreign material from the substrate. If the absorber–substrate interface proves to be an important quasiparticle loss region because of β-Ta inclusions or other impurities, future device designs can use a relatively thick ($d > \xi$) Nb layer to prevent quasiparticles from sampling the SiO_2 substrate surface.

The need for high temperature Ta deposition puts some restrictions on the device design. The Ta must be deposited before any of the aluminum films because of aluminum's low melting temperature, and because aluminum oxide tunnel junctions typically do not survive well above 200° C.[Bhushan, 91; Feautrier, 92; Shiota, 92] There is a benefit, however, to such restricted device designs. If we find that higher purity Ta films are necessary for good device operation, we can perhaps obtain UHV-deposited Ta from an outside vendor, and then proceed with our standard device fabrication process.

5.2.2 Stress Minimization and Columnar Growth

The Ta film stress was minimized for room temperature deposition using the simple technique of observing the behavior of photoresist beneath the deposited Ta film.[Przybysz, 89] Because of photoresist's low tensile strength, even small amounts of stress in the overlying Ta films result in wrinkling (compressive stress) or cracking (tensile stress) of the photoresist. The typical procedure for minimizing stress utilizes the film stress dependence on Ar sputter gas pressure. We varied the Ar pressure between 3 and 40 mtorr, with stress varying (as is typical) from compressive at low pressure to tensile at high pressure. A minimum stress level was found for ≈ 35 mtorr Ar. Films grown at this Ar pressure gave reasonable T_c, but room temperature resistivity from 22 to 25 μΩ-cm and RRR ≈ 2. Similar results, with slightly lower resistivity and slightly higer RRR were obtained for high temperature deposition at ≈ 35 mtorr Ar. Such films are not ideal for x-ray absorbers because their small diffusion constant inhibits hotspot dissipation and rapid quasiparticle trapping.

We believe that the mechanism for stress relief in these films is columnar growth.[Thornton, 75; Thornton, 86; Haghiri-Gosnet, 89; Mattox, 92] At relatively low deposition temperature with respect to Ta melting point (T_m ≈ 3000° C), the mobility of the Ta atoms on the SiO_2 surface is low, and incident atoms adhere where they impinge. There is a shadowing effect during growth, because high points on the substrate surface receive more coating flux than valleys. This is enhanced at high Ar sputter gas pressure due to an increased randomization of the angle of Ta atom incidence. Resulting Ta films have a fine vertical fibrous structure with wide boundaries typically enclosing voids. These boundaries are stable due to the low adatom mobility and the tendency of the boundaries to entrap impurities.[Haghiri-

Gosnet, 89] The relatively high film resistivity likely results from poor electron transport across such boundaries.

The adatom mobility can be increased by raising the substrate temperature, or by increasing the kinetic energy of the incident adatoms.[Thornton, 75] Raising the substrate temperature is straightforward; the kinetic energy can be increased by reducing the Ar sputter gas pressure (given a constant DC sputter bias voltage). For lower Ar pressure, the Ta atoms will experience fewer collisions before reaching the substrate. Thus, they will be somewhat more directional, and have somewhat higher kinetic energy when they impinge on the substrate. We believe that our adjusted deposition conditions ($T_{dep} \approx 700°$ C, 6 mtorr Ar) move us out of the regime of wide grain boundary formation (zone I in Thornton's [75] description), and into a regime of more densely packed grains (zone T). For these deposition parameters, the adatom mobility is sufficient to overcome the shadowing effect, so the grains are separated by fine boundaries without voids. Figure 5.2.2 illustrates the different grain structure in Ta films grown at high Ar pressure, or grown at low Ar pressure and high temperature. Note especially the voids and thick grain boundaries in the zone I film. Rapid indiffusion of oxygen or other impurities can take place along grain boundaries in zone I Ta films, causing increased electrical resistivity and changes in film stress with time.[Yoshihara, 93] The more dense structure does not allow such rapid oxygen indiffusion, and will form more stable high quality x-ray absorbing films. The room temperature resistivity for such films is significantly lower, $\approx 14\ \mu\Omega$-cm, and the RRR increases to ≈ 20. As the boundary voids disappear, the electrical properties of the Ta improve significantly. However, the stress also increases, primarily because the voids are no longer present to relieve the stress within the Ta grains.

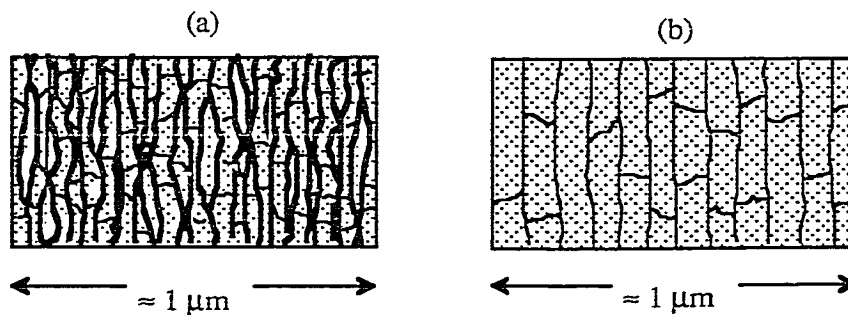

Figure 5.2.2: Schematic representation of Ta grain growth. a) High Ar pressure (zone I), b) low Ar pressure and high temperature (zone T).[Thornton, 75]

Pressures lower than 6 mtorr of Ar are not used in our work because of the sensitivity of film stress to Ar pressure; ≈ 6 mtorr Ar results in Ta films which do not exhibit extreme stress. Films grown at ≈ 3 mtorr Ar often show peeling from the SiO_2 beneath. In an effort to grow Ta films with even higher diffusion constant, we tested crystalline MgO as a substrate. For 6 mtorr Ar, ≈ 700° C deposition, we obtained RRR greater than 30. The use of this substrate with our deposition equipment might form Ta of high enough diffusion constant to support 0.5 mm long devices, although the use of a thick crystalline substrate might result in poor device performance (see Section 5.1).

Note also that Figure 5b shows Ta edges which are somewhat sloped. The fabrication procedures detailed in Appendix 1 report that we use a wet chemical etch to pattern the Ta films. This wet etch is used intentionally to give sloped Ta edges for better step coverage of subsequently deposited films. This can be quite important for the thick Ta films (d ≈ 0.6 µm, or, eventually, ≈ 2 µm) and thin trap films (d ≈ 0.2 µm) we use. Although the superconducting gap in the Ta could be somewhat depressed at the edges where the film thickness is less than a coherence length,[Kraus, 93] this does not appear to be a cause of significant quasiparticle losses in our devices. If necessary in the future, we can use RIE to trim the edges which are not covered by other films.

5.3 Absorber Wiring: Nb

The absorber wiring is ≈ 1500 Å of Nb (T_c ≈ 9 K, RRR ≈ 5) sputter deposited on the Ta at nominally room temperature. Argon sputter gas pressure is 11 mtorr, chosen to minimize film stress as indicated by photoresist deformation.[Przybysz, 89] For simplicity, and to eliminate the need for an etch stop beneath the Nb, image reversal photoresist liftoff is used to pattern the Nb.[Meier, 91] The deposition rate is ≈ 10 Å/sec (the maximum for the available power supply), with ≈ 1×10^{-7} torr background pressure. Compared to Ta, there is relatively little difficulty in obtaining good quality, high gap Nb films. Aside from the need to obtain a high gap, there is no restriction on the purity of the Nb film because it is not involved in the quasiparticle diffusion process. We obtain $T_c \geq 9$ K for deposition rates above ≈ 9 Å/sec, with a gradual decrease in T_c for reduced deposition rate, presumably due to contamination from the nonzero background pressure. Room

temperature resistivity is slightly above the bulk value, due to the residual impurity, surface, and grain boundary scattering.

As mentioned in Sections 2.2.5 and 3.2, it is desirable to use a high gap superconductor such as Nb to prevent quasiparticle losses from the absorber due to outdiffusion. Niobium is preferable to higher T_c compound superconductors because of the relative ease in forming good films. The only other elemental superconductors with higher gap than Ta are V and Pb. Vanadium is undesirable because its energy gap is only slightly higher than that of Ta, and thus does not form a very effective outdiffusion barrier for energetic Ta quasiparticles (Section 3.2). Lead is undesirable because of its incompatibility with clean vacuum systems, because it is a soft metal much less resistant to the effects of thermal cycling and aging, and because of its short x-ray absorption depth.

Niobium has a significantly longer x-ray absorption depth than Ta. This longer absorption depth, in conjunction with the relatively small volume Nb film we use to form the wiring, results in relatively few absorption events in the Nb film. Absorptions in the Nb film will give varied STJ response, primarily due to the lack of an outdiffusion barrier, and will thus broaden the energy resolution. To reduce the number of absorption events in the wiring, an Al film completes the wiring $\approx 20\ \mu m$ from the Ta absorber (see Figure 5). Because $\Delta_{Al} << \Delta_{Nb}$, any quasiparticles generated by x-ray absorptions in this Al wiring will be blocked from entering the Ta absorber, and will thus give negligible signals in the STJ. Future device designs will bring the Nb under an x-ray mask to so that only near-gap-edge Ta quasiparticles will sense the Nb wiring (Section 3.2).

5.4 The Tunnel Junction Region

An expanded view of the tunnel junction region is presented in Figure 5.4. The tunnel junction area and the SiO via area are designed as large as possible within the trap area, with constraints that the tunnel junction be quartic shaped and that $2\ \mu m$ alignment tolerances are allotted.

5.4.1 The Tunnel Barrier: Al Oxide

The shape of the barrier is based on Peterson's [91] calculations showing quartic junctions to be highly effective in low field critical current suppression. The $\approx$ $2\ \mu m$ wide pedestal on the edge of the junction shown in Figure 5.4 is reduced to a

fine point by the wet etch used to define the tunnel barrier, and does not appear to adversely affect the critical current suppression. The junction is somewhat "stretched" (Section 4.2.2) to present more area to the applied magnetic field, thus reducing the field necessary to thread a flux quantum through the junction. This device exhibits strong zeros in critical current every ≈ 1.5 G. Unfortunately, the largest junction dimension (≈ 200 μm) places a Fiske mode at ≈ 90 μV, which apparently causes a significant reduction in the maximum achievable dynamic resistance. The smaller tunnel junctions we have tested (≈ 580 μm^2, longest

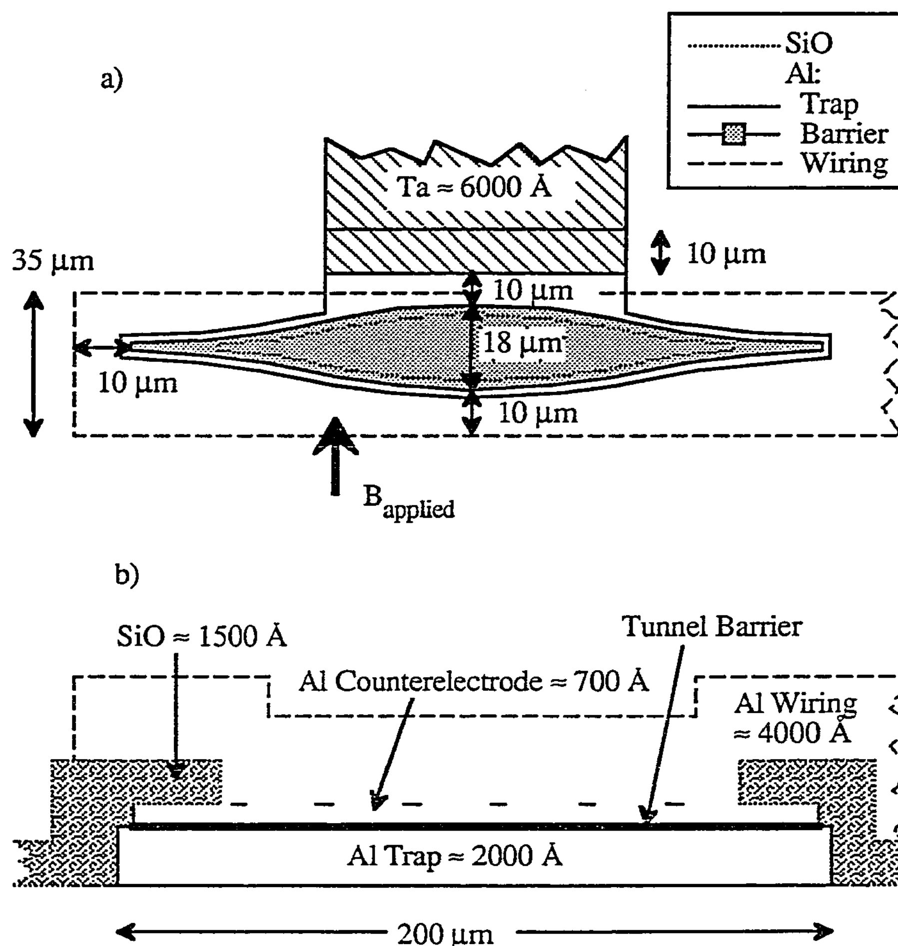

Figure 5.4: The tunnel junction region of Figure 5. Top view (a) and side view (b). The dotted line above the Al counterelectrode represents an interface which has been exposed to atmosphere before ion beam cleaning and Al wiring layer deposition.

dimension ≈ 100 μm) give a somewhat higher R_{dyn}/R_{nn} ratio, but still possess a Fiske mode at ≈ 130 μV. These Fiske modes typically force us to apply magnetic fields greater than 5 G to achieve stable biasing with high dynamic resistance.

The current density of the tunnel barrier is somewhat sensitive to the deposition rate of the Al trap layer (higher rate gives higher current density), to the oxidation time and pressure (as expected), and to the Al counterelectrode deposition rate (higher rate gives higher current density). A systematic study was not performed, but a general characterization of the junctions can be made: for 2000 Å thick Al traps thermally evaporated at ≈ 200 ± 20 Å/sec, exposure to 500 mtorr dry oxygen for 2 hours, followed by counterelectrode deposition at ≈ 20 ± 5 Å/sec gives current densities between 25 A/cm^2 and 50 A/cm^2.

The specific capacitance of these barriers is ≈ 40 fF/μm^2. [Houwman, 90; Mayer, 91] To obtain negligible electronic noise, we must keep the junction capacitance below ≈ 75 pF (Section 4.1.2). The junction shown in Figure 5.4 has area ≈ 1800 μm^2, with capacitance ≈ 75 pF. Other junctions were designed and tested with area ≈ 580 μm^2 and capacitance ≈ 25 pF, but did not perform as well, possibly due to slower tunneling out of the trap volume (see Chapter 7).

During the ion beam clean of the Ta and the Al/AlOx/Al trilayer deposition, a copper disk is placed on the back of the sample substrate, but is not attached with vacuum grease. It does not appear that the substrate is significantly heated by the ion beam clean and Al evaporations, as inferred from the successful photoresist liftoff of the similarly deposited Al wiring layer (which also follows an ion beam clean). However, because of the significant effects of substrate heating on tunnel barrier quality seen in Nb trilayer junctions,[Bhushan, 91; Feautrier, 92; Shiota, 92] our STJs will be fabricated in the future with thermal grease securing the substrate to the copper. Concerns about the tunnel barrier quality also prevent us from placing any portion of the tunnel barrier above the Ta film. The deposition parameters, etching parameters, and thickness of the Ta layer result in a textured surface, which might prove harmful to tunnel barrier quality.

5.4.2 The Trap: Al

So that tunnel times are not limited by diffusion from the absorber to the tunnel junction, and that impurity-induced quasiparticle recombination does not cause excess quasiparticle loss in the trap, the Al trap film is deposited at a very high rate in

good (1×10^{-7} torr) vacuum. This gives high quality films: $T_c \approx 1.2$ K, RRR ≈ 8, limited by boundary scattering, $D \approx 1300$ cm^2/sec.

The Al trap is designed to optimize the effective *lateral* trapping. For a given trap volume, lower junction resistances are preferable to minimize recombination losses, provided one can still obtain ideal subgap I-V characteristics. Thus, a large surface area thin film is used to form the trap, and the tunnel junction covers as much of the trap as possible (subject to the capacitance constraint mentioned above). The barrier must be quartic shaped; therefore, the trap is also designed with a quartic lobe. A large absorber–trap interface area is desirable for faster trapping, but because the tunnel junction is not placed on the thick Ta/Al bilayer, larger interfaces imply excess trap volume and longer tunnel time. The junction is spaced ≈ 10 μm from the Ta absorber to avoid film overlap problems with the very thick Ta. (More recent mask designs used stricter alignment tolerances, and successfully brought the junction only 5 μm away from the absorber.) The trap is *thick* enough that step coverage on the (wet etched) Ta absorber is straightforward, and that the junction definition etch has enough error margin, as there is no etch stop (see Appendix 1). The trap is *thin* enough that the tunnel time is of order a few microseconds for readily achievable current density junctions.

Future designs of these STJ devices will utilize double junction geometries [Kraus, 89a] for positional resolution. To obtain good positional resolution, fast trapping is necessary. To obtain fast trapping while maintaining short tunnel times, we are performing tests to determine the optimal ion beam parameters for cleaning the Ta surface immediately before the Al trap deposition. Better ion beam cleaning will allow us to shrink the trap–absorber interface area for a given trapping time. The trap–absorber interface is now approximately 10 μm x 100 μm. Presently, the "excess" Al trap volume on the Ta lengthens the tunnel time by an extra factor of 1/2. Devices with 5 μm x 100 μm interfaces have successfully detected x-rays, but with relatively inefficient charge collection (Chapter 7).

5.4.3 The Counterelectrode: Al

The counterelectrode is formed of Al, slowly evaporated (≈ 20 Å/sec) to reduce the possibility of barrier damage from excess substrate heating.[Bhushan, 91; Feautrier, 92; Shiota, 92] The film is kept thin (≈ 700 Å) for good error margin in the junction definition etch, but thick enough so that it will easily withstand an ion beam clean before the Al wiring deposition. Even at only ≈ 20 Å/sec, we obtain good

quality films, as indicated by the $T_c \approx 1.2$ K. The counterelectrode and wiring films are intentionally made clean to promote rapid outdiffusion with minimal backtunneling.

5.4.4 The SiO Passivation

A ≈ 1500 Å thick thermally evaporated SiO film is used to passivate the junction edges. Excessive junction heating during the SiO evaporation is prevented with a copper disk (with vacuum grease) heat sinking the substrate. This film has been tested to be free of pinholes, thus forming a very good insulator. To minimize quasiparticle backtunneling, the area of the via (≈ 1000 μm^2) above the junction is maximized, within the constraints of alignment tolerance. Our tests on this type of junction, and on other junctions where the via area is intentionally reduced, indicate that the counterelectrode–wiring interface is quite transparent to quasiparticles, and that backtunneling is not an issue even for ≈ 20 μm^2 vias (Section 7.7). Present devices use the SiO as a passivation layer on top of the Ta absorber. This is likely not necessary, and future device designs will eliminate passivation layers on the Ta absorber to remove any dead layer for low energy x-rays.

The DC I-V characteristics of our junctions (Chapter 6) show some excess subgap current characteristic of S-I-N tunneling regions. It is quite possible that such regions exist at the perimeter of the tunnel junction, where the aluminum oxide barrier contacts the SiO. Tests are planned to determine if the excess current is due to a "perimeter" defect or an "area" defect in the barrier. If the perimeter is to blame, we will likely switch to e-beam evaporated Al_2O_3 for the passivation layer, with the hope that removal of Si from the tunnel barrier edges might eliminate edge leakage. If the excess current appears to be an area effect, we will address different oxidation methods, as well as active prevention of substrate heating during and after tunnel barrier formation.[Bhushan, 91; Feautrier, 92; Shiota, 92]

5.4.5 The Al Wiring

After an *in situ* ion beam cleaning, the Al wiring is deposited on the counterelectrode and on the Nb wiring. For simplicity, and to avoid perturbing the sensitive Al already on the wafer, this layer is defined by photoresist liftoff. To minimize possible tunnel barrier degradation, vacuum grease and a copper disk are used to heatsink the substrate during the ion beam cleaning and film deposition. The wiring is made relatively thick (≈ 4000 Å) to promote rapid outdiffusion with minimal

reverse tunneling and backtunneling. The deposition conditions (1×10^{-7} torr, ≈ 30 Å/sec) ensure that the film is clean, with a high diffusion constant. For device testing to date, the x-rays have been of high enough energy that we can neglect any absorption in the wiring layer. The shorter absorption depth of low energy x-rays will require that we mask off the Al wiring, or replace it with a normal metal (with fast electron-phonon scattering) a short distance from the STJ.

The thick wiring also serves two other purposes. Its rather good thermal conductivity reduces junction self-heating, and it forms rugged contact pads. We use spring-loaded contacting pins (manufactured by Augat Corp. or IDI Corp.) because of the potentially more rapid device turn-around time. An upper limit on the contact resistance at cryogenic temperatures can be placed at 1 Ω, as determined by a simple two wire measurement.

5.5 Discussion

The STJ device is surprisingly complicated, given the rather simple operating principle. In our design, each film material and shape has been chosen to optimize the device performance. There are numerous cases where the design actually does work as planned. The amorphous SiO_2 layer on the substrate appears to significantly reduce STJ signals from the absorption of x-rays in the substrate. High quaility Ta films are now relatively straightforward to deposit, and result in high charge output for 6 keV x-rays (see Chapter 7). The Nb absorber wiring effectively prevents quasiparticle outdiffusion (Chapter 7). The aluminum oxide tunnel barrier performs well, with low subgap current, and good critical current suppression at low fields (Chapter 6).

There are three aspects of the device design and fabrication which must be addressed in the very near future. Firstly, a reliable technique must be developed to mask x-rays from the trap region (Section 3.4.1). Secondly, the dynamic resistance of the tunnel junction must be increased, either by replacing the SiO with a different dielectric film, or by modifying the junction design to eliminate Fiske modes in the low bias voltage region (Section 6.2). Finally, the absorber–trap interface must be made as transparent as possible to quasiparticles. As shown in Figure 3.3.2, slower trapping does not significantly reduce quasiparticle recombination losses in the trap. Slow trapping, however, can result in lost absorption position information, and in longer current pulses with integrated height very sensitive to the electronic time constants in the amplifier (Section 4.1.1).

6. DC Device Characterization

The DC electrical behavior of a STJ device can give a good amount of information indicative of the device's high frequency pulse response. The device and amplifier pulse response is also determined to a large extent by the characteristics of the DC junction bias. The junction resistance for $V_{bias} >> 2\Delta$ gives us the (approximate) quasiparticle tunnel time. DC measurements of the current density of the various film interfaces can give us the trapping time as well as an idea of the backtunneling probability. The x-ray current pulse shape can be estimated if one knows the tunnel time, the trapping time, and the backtunneling probability. The DC magnetic field dependence of the tunnel junction can determine to a large extent how successful the DC biasing of the tunnel junction will be. Adequate suppression of the critical Josephson current and of Fiske modes are a must for stable, low noise DC biasing. Ideal SIS DC current-voltage (I-V) characteristics will ensure that the subgap current is low at our typical operating temperature, thus giving low shot noise. Ideal SIS subgap I-Vs can also give high dynamic resistance for low preamplifier noise gain and undistorted preamplifier signal response.

6.1 Interface Characterization

For optimal device performance, we must be able to form highly transparent interfaces between our superconducting films. The effectiveness of quasiparticle trapping relies on the nature of the absorber–trap interface; the likelihood of backtunneling is controlled in part by the transmissivity of the counterelectrode–wiring interface. The other superconductor film interfaces in the device are not as critical, but must support pair currents in excess of any DC bias current, and any quasiparticle current we expect an x-ray to generate. To obtain highly transmissive interfaces, ion beam cleaning is used *in situ*, immediately before the formation of each superconductor–superconductor interface. Ideally, this ion beam cleaning will remove any oxides or impurites that have formed on the surfaces of previously deposited films. Quasiparticle transmission between superconducting films should then be determined primarily by the superconductor bandgaps and the intentionally grown tunnel barrier.

One can use the tunnel time formula, Equation 2.2.4a, to estimate the time to cross any interface. (The density of states factor in this equation belongs to the film from which the quasiparticles begin [de Korte, 94], and the factor due to the enhanced

density of states can be taken as ≈ 1.) So, simply by measuring the current density of the absorber–trap interface, we can find the trapping time. We have performed measurements on the current density of 10 μm x 10 μm Ta–Al interfaces formed in the same processing step as the absorber–trap interfaces on two particular STJ device wafers (X-C93 and X-N93). The ion beam cleaning and film deposition parameters are given in Appendix 1. For the X-C93 interface, we find $J_c \approx 20{,}000$ A/cm^2. (Because of the interface overlap geometry and the small interface dimensions ≈ λ_J, current saturation should not be a problem here. See, e.g., Johnson [70], and Section 5.3 in Barone [82].) Plugging into Equation 2.2.4a, we obtain the time for a quasiparticle to travel from the absorber to the trap: $\tau_{a\text{-}t} \approx 1.2$ μsec. (This assumes the absorber volume is 10^4 μm^3, and the absorber–trap interface is 10 μm x 100 μm. This corresponds to the *short* trap devices in Chapter 7.) Traveling in the other direction is somewhat faster because of the smaller volume trap (850 μm^3), and the smaller density of states. We thus have a time to travel back into the absorber $\tau_{t\text{-}a} \approx$ 30 nsec. To estimate the trapping time, we note that the inelastic scattering time (Section 3.2) in the Al trap is ≈ 20 nsec, somewhat shorter than $\tau_{t\text{-}a}$. We can thus get a rough estimate for the trapping time as simply $\tau_{trap} \approx 1.5$ μsec ($\geq \tau_{a\text{-}t}$). It is interesting to note that the $J_c \approx 20{,}000$ A/cm^2 interface in this device corresponds to a probability of one part in 10^5 that incident quasiparticles will traverse the interface. Even with such a high degree of reflection, we still calculate trapping times of ≈ μsec. The extended trap devices (where the absorber–trap interfaces are ≈ 100 μm x 200 μm) discussed in Chapter 7 will also be limited in trapping time by the absorber/trap interface transparency. For these devices, however, the large area interface gives τ_{trap} ≈ 100 nsec.

The interface test of device X-N93 gave $J_c \approx 15{,}000$ A/cm^2, somewhat less transmsmissive than X-C93, but not disastrously so. It is quite probable that the absorber–trap interface is not as clean in the X-N93 device. The ion beam cleaning of the absorber prior to the trap deposition was performed with essentially the same parameters in both wafers, but the base pressure in the chamber prior to the X-C93 cleaning was ≈ 4 x 10^{-8} torr, and was ≈ 1 x 10^{-7} torr prior to the X-N93 cleaning. The only other significant difference in the processing of the devices is the etch used to define the Ta absorber. In X-C93, the Ta was etched with an SF_6 RIE, whereas the X-N93 devices used the wet chemical etch outlined in Appendix 1.

Because the time from the end of the ion beam cleaning to the start of the Al trap deposition is at most two seconds, it is surprising that base pressure variations of < 1 x 10^{-7} torr would have any effect on interface transparency. More than six

months elapsed between the fabrication of X-C93 and the X-N93 devices, so it is conceivable that the characteristics of the ion gun changed enough to give a significantly worse cleaning to the latter devices. A more likely scenario involves the effects of the wet etch on the Ta surface. The use of the $FeCl_3$:HCl:HF:H_2O etch solution can leave a tough residual oxide or Fe precipitates on the Ta surface.[Gaidis, 94] With such surface contamination, the ion beam cleaning might not be as effective.

An extensive optimization of the ion beam cleaning procedure has been started at Yale, using the orthogonal design method.[Yin, 87] Specific parameters which will be examined include:

1) vacuum chamber base pressure,
2) Ta absorber etch / surface preparation prior to ion beam cleaning,
3) reproducibility of ion beam etch as a function of time (> 6 months),
4) beam voltage,
5) Ar^+ ion current density impinging on the Ta,
6) ion beam etch time, and
7) time between ion beam etch and Al trap deposition.

Parameter number 4, the beam voltage, warrants some extra discussion. The high beam voltage presently used (500 V) can result in an amorphous layer at the Ta surface, as well as significant incorporation of Ar into the Ta surface.[Kondo, 93] Either result is detrimental to the formation of a clean interface for ideal quasiparticle transmission. Lower beam voltages should reduce the severity of these problems, while still providing reasonable etch rates. Tantalum should etch reasonably quickly even for 150 eV Ar ions.[Laegreid, 61; Face, 87]

The other critical interface in the device is between the Al counterelectrode and the Al wiring layer. No explicit tests of the interface have been performed to date, but we can infer that the interface must be clean enough to prevent backtunneling (Section 7.7). We believe an important factor in obtaining the high quality Al–Al interface was the use of molybdenum ion optics in our Kaufman-type ion gun. While no quantitative measurements were made, it was found that carbon grids did not give high quality interfaces. Apparently, the Mo which is (unintentionally) sputtered from the grids to the sample surface does not form insulating compounds as the carbon might.

6.2 Magnetic Field Suppression of Pair Currents

As discussed in Section 4.2, applied magnetic fields are used to stabilize the DC current source bias. High magnetic fields can depress or destroy superconductivity, so minimization of the necessary magnetic field is a critical aspect of good device performance. Figure 6.2a displays the critical current suppression due to an applied magnetic field for one of our (unstretched) quartic junctions. L, the junction length presented to the magnetic field, is approximately 50 μm, giving a theoretical value of ≈ 7 G for the first minimum of I_c. The location of the zeros in the experimental curve agrees well with theory. The zeros are strong, and relatively broad in terms of magnetic field, thus allowing very stable DC junction biasing even for small drifts in the applied magnetic field. The peaks of the sidelobes decrease in an envelope given approximately by B^{-3}, slightly worse than the theoretically expected B^{-4} [Peterson, 91], but significantly better than the B^{-1} from rectangular junctions. The discrepancy can be attributed to slightly asymmetric junction patterns, which were the result of low resolution mask fabrication equipment.

Similar quartic junctions "stretched" to different lengths L give qualitatively the same behavior. Junctions with L ≈ 200 μm exhibit spacing between zeros of ≈ 1.5 G at low fields. Higher fields tend to give smaller spacing. Junctions with L ≈ 100 μm exhibit zeros every ≈ 2.5 G at low fields (< 10 G), with spacing ≈ 1 G at higher fields. Although the first or second zero in each of these quartic junctions is strong enough to adequately suppress the zero voltage Josephson current, Fiske modes are not so well behaved, and force us to bias at higher order zeros of I_c.

Fiske Mode Suppression

The steps in subgap current arising from geometrical junction resonances (Fiske modes) give rise to instabilities in the DC current bias, and result in degraded device noise performance. From our point of view, the most important effect of the Fiske modes is the degradation of device noise performance through decreased dynamic resistance (larger noise gain) and increased DC bias current (increased shot noise). These effects are very difficult to circumvent because the Fiske resonances are relatively broad, and are located near desired bias voltages. Subgap I-V characteristics ($eV_{bias} < \Delta_{Al}$) for a L ≈ 100 μm "stretched" quartic junction are presented in Figure 6.2b. For best device noise performance, the magnetic field is tuned to give the maximum stable dynamic resistance through modulation of the Fiske resonance. Tuning the magnetic field for good Fiske mode suppression will

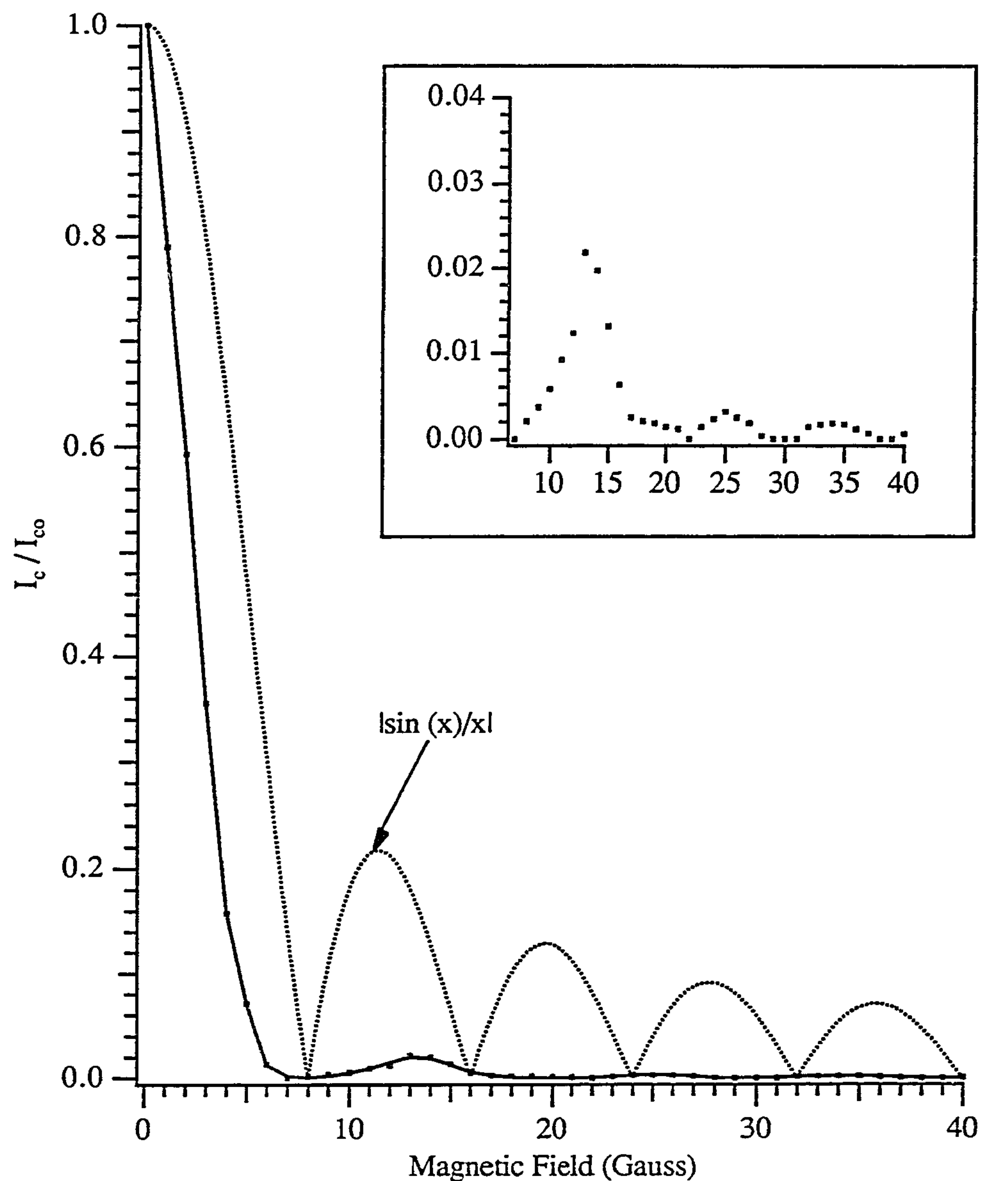

Figure 6.2a: Suppression of the critical current with a magnetic field for one of our quartic junctions. The device is aluminum–aluminum oxide–aluminum, with $J_c \approx 35$ A/cm^2, and junction length $L \approx 50$ μm. The operating temperature is ≈ 0.35 K ($\approx T_c/3.5$). The |sin(x)/x| curve representative of a similar sized rectangular junction is shown for comparison. An expanded view of sidelobe suppression at the higher fields is shown in the inset. (X-H92, 4/14/92)

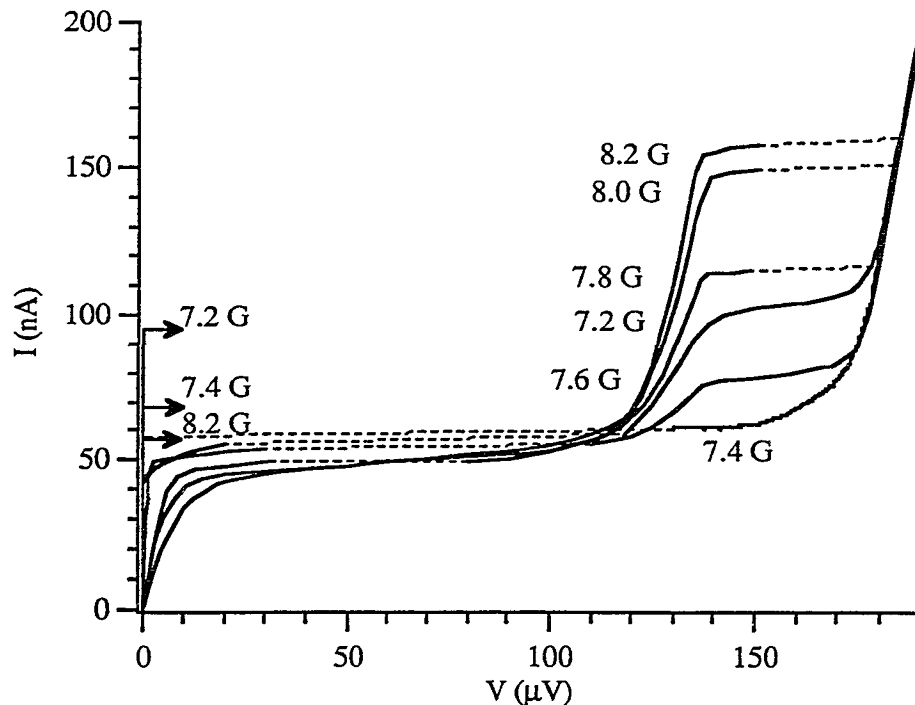

Figure 6.2b: Fiske mode dependence on applied magnetic field for 100 μm long device. I-V curves for 7.8 G and 8.0 G are stable for all $V_{bias} \leq 150\ \mu V$. DC current bias load line is 1 MΩ. All curves for $V_{bias} > 0$ are displayed for current swept in a decreasing fashion. Dashed lines indicate hysteretic switching. (X-D94, 4/10/94)

detune the zero voltage critical current suppression, as also seen in Figure 6.2b. Stable current source biasing requires that the zero voltage critical current be less than the subgap DC bias current. To achieve Fiske mode suppression and critical Josephson current suppression simultaneously, it is most practical to apply higher magnetic fields, at which the zero voltage critical current is much less sensitive to applied field (ideally falling as B^{-4}), and then fine tune the field to reduce the influence of Fiske modes.

The Fiske mode in Figure 6.2b is located at ≈ 140 μV, approximately 75% of the 180 μV predicted for a one dimensional mode in a cavity of length L ≈ 100 μm. This low voltage is likely a two dimensional effect [Nerenberg, 76] which can be difficult to predict for non-rectangular junctions. The large current step in Figure 6.2b at ≈ 180 μV coincides with $eV_{bias} \approx \Delta_{Al}$, and is likely the result of undesired NIS tunneling regions in the device. Note that the current increase at ≈ 180 μV can

be partially attributed to the first one dimensional Fiske mode in the tunnel barrier cavity. The combination of Fiske modes and NIS tunneling regions makes it difficult to determine the intrinsic tunnel junction quality. The temperature, field, and voltage dependencies of these two mechanisms are different, and, in principle, allow one to separate the two effects. In practice, however, this is quite difficult because of the great number of variable parameters involved in the theory for the two processes.

Figure 6.2c shows the low voltage I-V curve for a barrier of length L ≈ 200 μm. The first resonance appears at ≈ 90 μV as predicted for the first one dimensional mode in a rectangular cavity of length L ≈ 200 μm. As indicated in the figure, the resonance voltage does not change significantly with temperature. There is a second resonance at ≈ 120 μV, which can be attributed to a two dimensional mode. The slope of the I-V for voltages less than ≈ 80 μV is significantly larger than predicted by theory for SIS devices [van Duzer, 81], due perhaps to NIS tunneling regions, or to a broad (two dimensional) Fiske resonance.

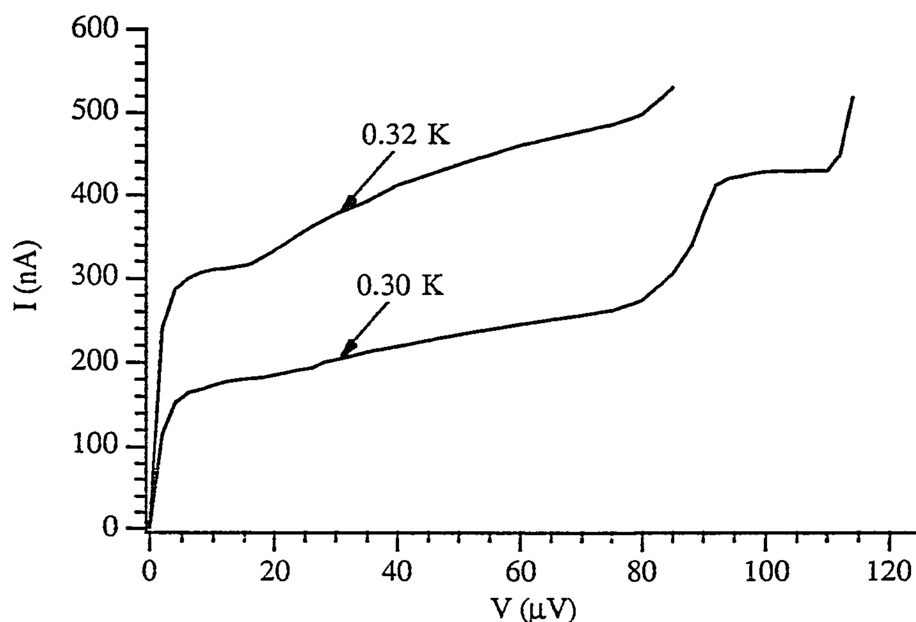

Figure 6.2c: Subgap I-V characteristic for 200 μm long quartic junction. Applied field ≈ 4.8 G. (X-C93, 4/12/94)

In general, the Fiske modes cause much difficulty for stable, low noise DC current source biasing. Although the Fiske resonance currents are ≈ 1000 times

smaller than the zero field Josephson current, they are particularly troublesome for STJ devices used as x-ray detectors. The low bias currents necessary for our device operation can be overwhelmed by the Fiske resonance currents, and the decreased dynamic resistance in the subgap region can result in poor matching to the charge amplifier, in terms of both noise and pulse shape distortion.

As indicated by the hysteretic behavior in Figure 6.2b, there is some hope that a DC load line of resistance less than ≈ 1 kΩ could allow biasing in a very high dynamic resistance region below the Fiske mode. In the near future, a low noise, stable DC voltage source will be developed to bias devices at higher dynamic resistance, potentially resulting in much improved device electrical performance.

6.3 DC Junction Current–Voltage Characteristics

The DC I-V traces presented in this section were all obtained with a high impedance (1 MΩ) current source. The voltage across this 1 MΩ bias resistor was amplified by either an Analog Devices AD624C or a Burr-Brown INA110KP instrumentation amplifier (inamp) to give the vertical (current) component on the trace, and the voltage across the junction was fed directly to either an AD524C or an INA110KP inamp to give the horizontal (voltage) component. The inamp voltages were then fed to Burr-Brown ISO100BP isolation amplifiers, and then sent to a Hewlett-Packard x-y plotter. The temperature was measured with a Lake Shore GRT (GR-200A-50), and, due to a temporary heatsinking difficulty, might be in error (high) by as much as 0.01 K at the lowest temperatures recorded (≈ 0.29 K).

The I-V trace for the L ≈ 100 μm stretched quartic junction is presented in Figure 6.3a. For reasonable bias voltages, the maximum subgap dynamic resistance is ≈ 9 kΩ, giving a ratio $R_{dyn}/R_{nn} \approx 5600$ at $T \approx T_c/4$. This is indicative of a relatively good quality tunnel barrier, and should result in low noise at the output of the charge amplifier. The Fiske mode at ≈ 140 μV (see Figure 6.2b) apparently does cause increased subgap conductance at bias voltages above 50 μV, and is at least partially responsible for limiting the ratio R_{dyn}/R_{nn} at ≈ 5600. The trap volume in this device is ≈ 500 μm^3, giving an expected tunnel time of ≈ 4.8 μsec. This value is approximately half the effective quasiparticle lifetime in the Al trap at 0.3 K. The device should therefore perform better at lower temperatures (where quasiparticle lifetimes are longer).

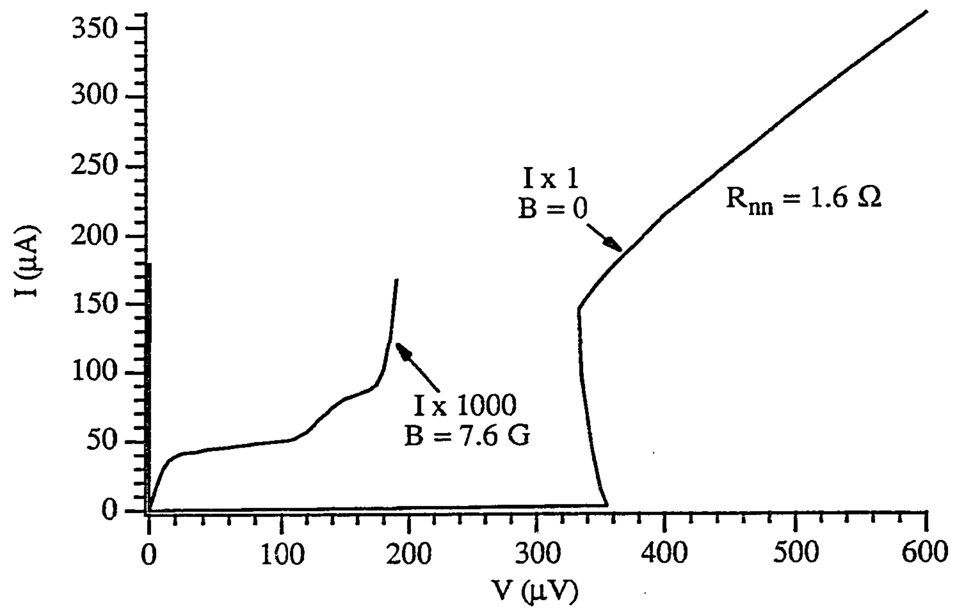

Figure 6.3a: DC I-V characteristic for a small quartic junction at T ≈ 0.3 K. Junction area is ≈ 580 μm^2, J_c ≈ 30 A/cm^2, I_{co} ≈ 180 μA. (X-D94, 4/10/94)

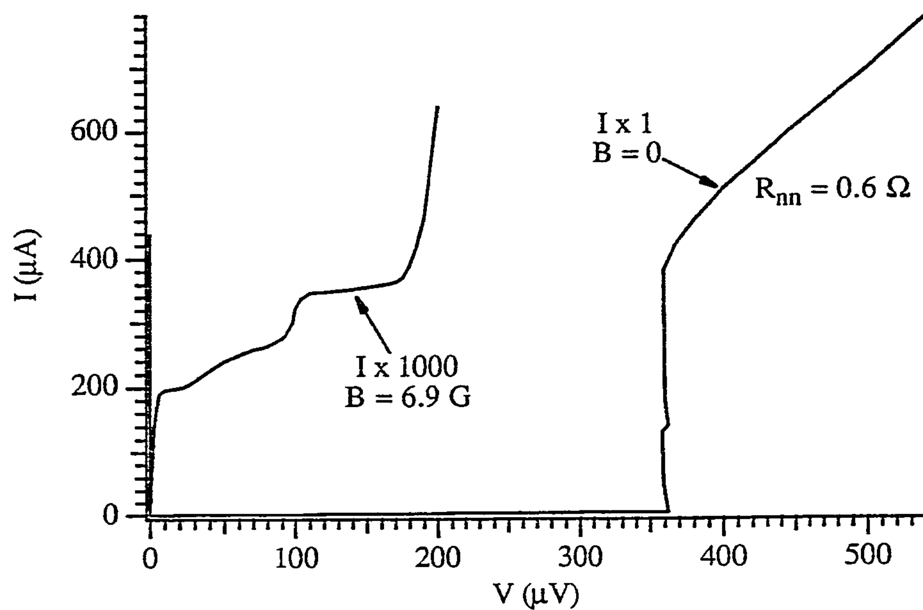

Figure 6.3b: DC I-V characteristic for a large quartic junction at T ≈ 0.3 K. Junction area is ≈ 1800 μm^2, J_c ≈ 25 A/cm^2, I_{co} ≈ 440 μA. (X-N93, 1/25/94)

For comparison, Figure 6.3b shows the I-V characteristic for a larger area stretched quartic junction ($L \approx 200\ \mu m$). Note that even though the current density is slightly lower than that of the device in Figure 6.3a, this device exhibits higher subgap current relative to the current at $eV_{bias} > 2\Delta_{Al}$. This could be due simply to the lower voltage Fiske resonances (corresponding to the larger junction dimensions), or it could be due to junction damage caused by substrate heating during fabrication. The device in Figure 6.3b was not heatsunk during the SiO via or Al wiring depositions, but the device in Figure 6.3a was.

In spite of the excess subgap current in the device in Figure 6.3b, its larger trap volume ($\approx 850\ \mu m^3$) and shorter tunnel time ($\approx 3\ \mu sec$) relative to the device in Figure 6.3a result in reduced quasiparticle recombination and larger signal output. However, primarily due to the higher noise gain, the signal-to-noise ratio is not significantly better than in the device of Figure 6.3a.

The sharp current rise at $\approx 180\ \mu V$ corresponds to $eV_{bias} \approx \Delta_{Al}$, and is likely due to normal conducting regions in the films surrounding the tunnel barrier. NIS tunneling is possible through these regions, and can result in increased subgap tunnel current. The effect is particularly noticeable for low temperatures and high voltages ($eV_{bias} \approx \Delta_{Al}$) where the NIS currents are larger than SIS currents (for the same R_{nn}). The NIS tunneling component will have a sharp increase at $eV_{bias} \approx \Delta_{Al}$, and, if the area of the barrier which allows NIS tunneling is large enough, this component will dominate the SIS current for bias voltages above Δ_{Al}/e. The normal conducting regions near the barrier can be due to tunnel junction defects or to trapped flux which may penetrate one or both of the junction superconductors.

The negative resistance portion of the curves in Figures 6.3a and 6.3b near $V \approx 350\ \mu V$ is likely a consequence of an inhomogeneous gap state in the superconductors created by the intense injection of quasiparticles at $eV_{bias} \approx 2\Delta$.[Gray, 78b] Due to inhomogeneities in the Al films, some slightly smaller gap regions will exist. Tunnel current will effectively heat these regions, causing them to grow until they engulf the entire film. The I-V characteristics will then appear to have been generated by lower gap films. This process is not a factor in x-ray detector devices, as we typically bias at very low currents, but it might be useful for determining the homogeneity of the films surrounding the tunnel barrier.

The low voltage region I-V of the device in Figure 6.3a is shown for several temperatures in Figure 6.3c. For voltages above $\approx 20\ \mu V$, these traces are not well fit by theory for ideal SIS junctions.[Van Duzer, 81] The magnitude of the subgap

current is comparable to the SIS theory, but the slope is not. The theoretical calculations (which are in fact well matched for some junctions [Zehnder, 94]) predict a negative differential resistance region above ≈ 40 μV in the I-V curves for our devices. This predicted negative resistance arises from the increasing bias voltage shifting the densities of states, such that the singularities on opposite sides of the barrier no longer overlap. The existence of such a negative resistance region would give us the ability to tune the junction dynamic resistance to arbitrarily high values by adjusting the bias voltage. It is possible that with the device characterized in Figures 6.2b, 6.3a, and 6.3c, a lower source impedance ($R_{source} < |R_{dyn}|$) bias circuit could find such negative resistance regions for specific values of applied magnetic field.

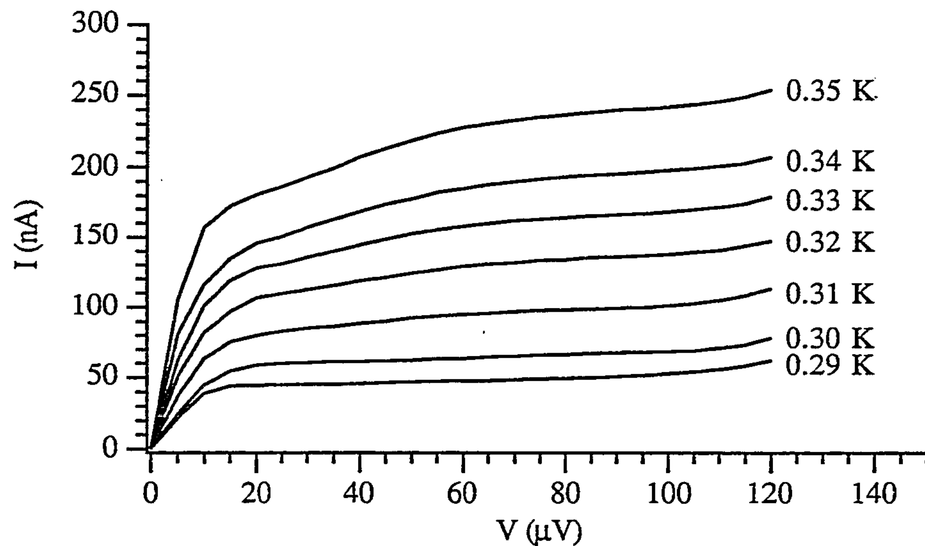

Figure 6.3c: Subgap I-V characteristics vs. temperature for a 100 μm long stretched quartic device. $R_{nn} \approx 1.6\ \Omega$, $J_c \approx 30\ A/cm^2$, $B \approx 7.8$ G. (X-D94, 4/10/94)

The encouraging aspects of Figure 6.3c involve the general temperature dependence of the subgap current. Down to the lowest temperatures measured, the subgap current decreases (and the maximum dynamic resistance increases) as the temperature is decreased. We are therefore not yet limited in performance by any barrier defect which might give a temperature-independent current. Lower temperatures should further improve the signal-to-noise ratio of this and our other devices by reducing the amplifier noise gain through increased junction dynamic resistance.

6.4 Discussion

The DC electrical characteristics presented above reveal that our devices should be useful for detecting x-rays, but that there is significant room for improvement. The interface between the Ta absorber and the Al trap may be suspect, and will require careful quantitative examination. Trapping times less than 1 μsec will likely be necessary for high performance devices, based on the amplifier response and the desire for imaging detectors. For a given interface transparency, this places a limit on the absorber volume. The interfaces must be as clean as possible to allow the large absorber volumes desired by x-ray astronomers.

In addition, the need for fast tunnel times (≈ 1 μsec) for minimal electronic pulse shape distortion limits the product of trap volume and R_{nn}. (Equations 2.2.4b and 4.1.1e). Tunnel barriers with lower R_{nn} can reduce the tunnel time, and thus reduce the quasiparticle losses due to recombination in the trap. As is evident from Equation 4.1.1e, however, reduction of the tunnel time by reducing R_{nn} will not reduce pulse distortion unless R_{dyn} is held constant (or increased). To date, our devices show very good characteristics, indicating that R_{dyn} will likely scale approximately linearly with R_{nn}. The best x-ray detectors will have $R_{dyn} / R_{nn} >$ 10,000, for large signal-to-noise ratio and minimal pulse shape distortion, about a factor of two better than our junctions. The achievement of such high R_{dyn} / R_{nn} ratios is of utmost importance, and will form the focus of much work in the near future at Yale. Lower temperatures, better suppression of Fiske modes, DC voltage biasing, and modification of junction fabrication processes will all be explored to increase this ratio.

7. X-Ray Detection

The best of our devices give energy resolution better than 200 eV for ≈ 6 keV x-rays, with ≈ 30% absorption efficiency, and active surface area of ≈ 100 μm x 100 μm. This chapter describes the x-ray data useful for understanding the present devices, and predicts future performance for modified devices and electronics. The relationship between the STJ current pulses and the electronically integrated charge pulses is shown in detail, experimentally demonstrating the need for reduced pulse shape distortion (theoretically described in Section 4.1.1). The effects of $2\Delta_{Al} < \Omega < 2\Delta_{Ta}$ phonons on pair-breaking in the Al trap, and the STJ response to substrate absorptions are examined. Our statements regarding trapping times and backtunneling probabilities are discussed as well. We are highly optimistic that only small modifications to these tunnel junction devices will give better than 100 eV energy resolution, and better than 50% absorption efficiency for 6 keV x-rays.

7.1 Cryogenic Testing

The STJ detectors described in the previous chapters detect x-rays. As we are not working in an EMI shielded room, the STJ detectors can also detect a great many other disturbances (elevators, electric motors, fluorescent lights, crying babies, ...). We have taken pains to eliminate the bulk of the unwanted disturbances, and have used mechanical shuttering of the x-ray source to verify that the observed pulses indeed result from x-rays. The x-rays used in this work come from radioactive ^{55}Fe, which emits x-ray lines at 5.9 keV (≈ 88%) and 6.5 keV (≈ 12%). The source is a thin film of the radioactive ^{55}Fe isotope, with ≈ 500 μCi activity, in a ≈ 1 cm^3 sealed container which thermally cycles well (available from Isotope Products Laboratories).

The devices are mounted on a copper cold plate at pumped ^{3}He temperatures. The dewar is an Infrared Systems type with closed-cycle ^{3}He charcoal pumping. Wires for junction current biasing and for thermometry are 5 mil manganin (≈ 50 cm long, ≈ 40 Ω at room temperature) from room temperature to the liquid ^{4}He stage, and are 5 mil NbTi (≈ 15 cm long) from the liquid ^{4}He stage to the sample. The wires for junction voltage sensing and for the magnet current are 34 awg Cu (< 5 Ω at room temperature) to the liquid ^{4}He stage. The sample leads continue as 5 mil NbTi to the sample. The wires are heatsunk at each cold stage using fired glass feedthroughs (available from Electrical Industries Corp, Murray Hill, NJ) which are soldered in copper sheets. The copper sheets are securely attached to the cold plates

with screws, Bellville washers, and thermal paste. Contact to the devices is made with spring-loaded pins from either of two companies, IDI or Augat (available from Newark Electronics). These pins are placed in a phenolic mount, which is then screwed to the pumped ^{3}He copper cold plate so as to contact the Al pads on the device chip.

7.2 Pulse Shapes

The current pulse generated by an x-ray is shaped by the STJ device's quasiparticle trapping time, tunneling time, and recombination time. The integrated charge pulse at the output of the charge amplifier is shaped by the input current pulse and the electronic decay time, as discussed in Section 4.1.1. Figure 7.2a displays four such integrated charge pulses from ≈ 6 keV x-rays (two pulses in the center overlap). A hasty observation of the ripple in the pulses gives a S/N of ≈ 100, consistent with the finding of ≈ 50 eV electronic noise in section 4.1.2. The integrated charge pulses are filtered with a single pole low pass (300 kHz) and a single pole high pass (100 Hz) RC-CR filter.

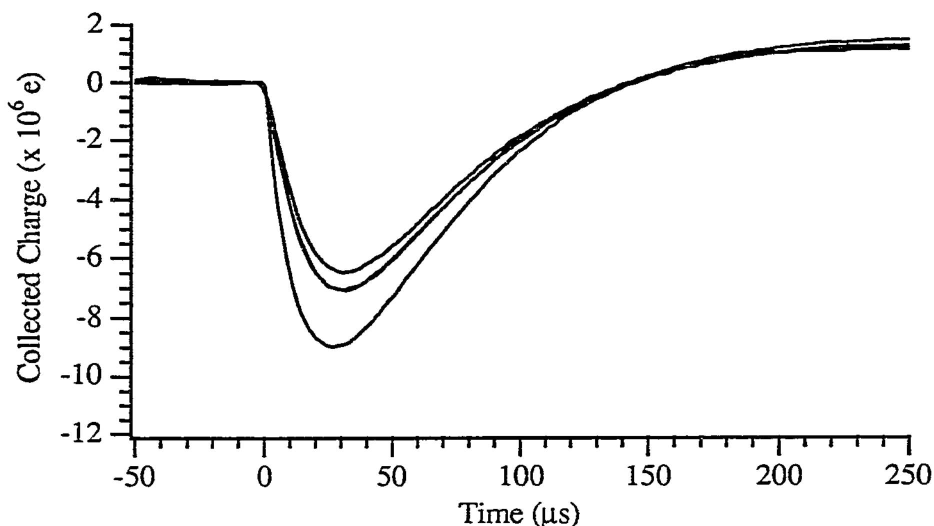

Figure 7.2a: Four integrated charge pulses for ≈ 6 keV x-rays. (X-N93, 3/9/94)

We have numerically differentiated one of the digitized pulses from Figure 7.2a. The integrated charge pulse and the scaled derivative (≈ -1 x current pulse) are presented in Figure 7.2b. Due to the effects of AC coupling and small values of τ_E, the junction current will differ from this calculated current pulse, particularly for long

times. Several aspects of Figure 7.2b warrant identification. Note that these pulses are inverted with respect to the pulse shapes shown in Figure 4.1.1c. This has no significance in terms of signal response (indeed, if the junction were DC biased at the negative of its present bias voltage, the pulses would switch polarity). In the following discussion, the leading edge of the current pulse is correlated with τ_{rise}, as used in Section 4.1.1, even though the leading edge has negative slope. The other risetimes are defined similarly.

The collected charge on the amplifier feedback capacitor is approximately *six million* electrons, a factor of a thousand more charge than the best semiconducting *p-n* junction detectors deliver. This corresponds to an effective minimal ionizing energy, ε, of $\approx$ 1 meV $\approx 1.4\ \Delta_{Ta}$. It is likely that there is some charge multiplication due to trapping and some charge loss due to premature electronic pulse decay, so we cannot immediately infer that only $\approx 1 - 1/1.4 \approx 30\%$ of the initial x-ray energy is lost to subgap phonons, although this is a good first approximation. It is evident that the Ta absorber must perform relatively well as an x-ray to quasiparticle converter, and that we can expect the Fano-factor limited energy resolution will be less than 10 eV, as predicted in Chapter 1.

The rise and fall times of the pulses in Figure 7.2 can be evaluated in light of the calculations of Section 4.1.1. This charge pulse has leading edge time constant

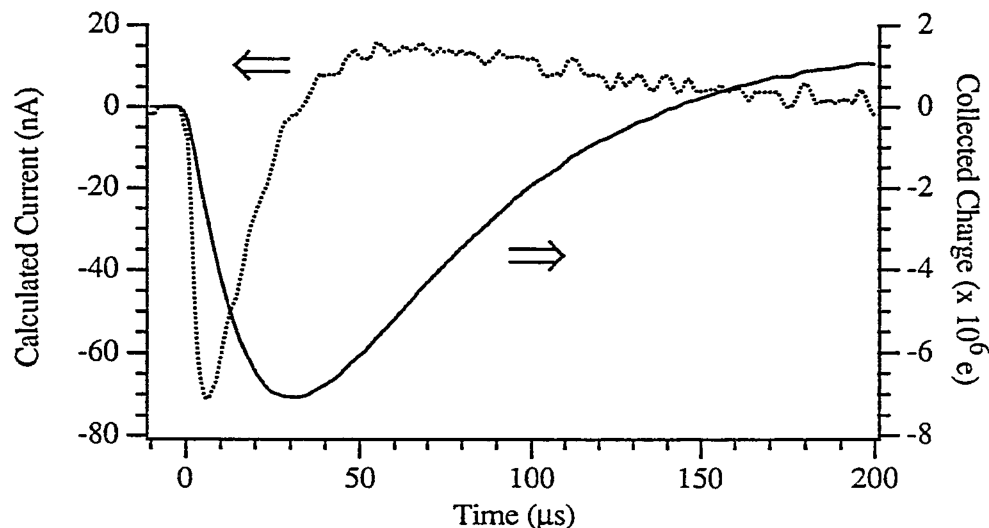

Figure 7.2b: Charge pulse from a ≈ 6 keV x-ray, and its computer-generated derivative. (X-N93, 3/9/94)

(τ_{fall} from Figure 4.1.1c) of ≈ 12 μsec. The plots presented in the remainder of the chapter frequently contain pulse "risetime"; this is defined as the 10% to 90% risetime of the charge pulse, as computed by the digital oscilloscope, and is ≈ 1.5 τ_{fall}. (Note that the pulse is not a perfect exponential, so the risetime is not ≈ 2.2 τ_{fall}.) To avoid confusion, the characteristic time constant will be referred to as τ_{fall}, and the 10-90 time will be referred to as "risetime." The charge pulse in Figure 7.2 exhibits a *risetime* of ≈ 17 μsec. The decay *time constant* of the pulse is $\tau_E \approx 60$ μsec. The pulse derivative exhibits a peak at $t_{max} \approx 7$ μsec, a leading edge time constant $\tau_{rise} \approx 3.5$ μsec, and a decay time constant $\tau_{fall} \approx 12$ μsec.

Fitting such amplifier output with the equations of Section 4.1.1, we could infer that $\tau_{trap} \approx 15$ μsec, $\tau_{loss} \approx 2$ μsec, and $\tau_t \approx 3$ μsec. However, we could obtain the same amplifier output $V_{out}(t)$ from $\tau_{trap} \approx 2$ μsec, $\tau_{loss} \approx 15$ μsec, and $\tau_t \approx 3$ μsec. (Backtunneling or reverse tunneling would be necessary to give $\tau_{loss} > \tau_t$.) We do not presently understand the mechanism for the long trap or loss time. Backtunneling could lengthen the loss time such that $\tau_{loss} \approx \tau_r$, and could possibly give ≈ 15 μsec with phonon trapping, but it appears that we do not have significant backtunneling (Section 7.7), and the factor of ≈ 2 lifetime enhancement needed from phonon trapping appears somewhat excessive (Section 2.2.3). A long trap time could give the observed pulse shapes, but measurements of the current density of the absorber-trap interface indicate that $\tau_{trap} < 3$ μsec (Section 6.1).

Experiments with different trap geometries (Section 7.6) give very different pulse shapes, indicating that the trapping process is actually responsible for the lengthy current pulses, rather than backtunneling or some other mechanism like long-lived phonons. In addition, x-rays which are absorbed in the Ta closer to the trap result in much faster charge pulse risetimes, giving some indication that anomalously slow quasiparticle diffusion might be responsible for a long trapping time. The quasiparticles and phonons should not be well coupled at times greater than ≈ 1 nsec (Section 2.2.1), so quasiparticle transport at a reduced *phonon* diffusion "velocity" is not likely. The diffusion velocity of quasiparticles in Ta is currently under investigation by our group, using a multijunction injector–detector structure similar to that of Hsieh and Levine [68]. These tests should give some indication of the reduction of the quasiparticle diffusion velocity by the curvature in the dispersion curve.

7.3 X-Ray Energy Spectra

Charge amplifier output pulses like those in Figure 7.2a were digitized and measured for the maximum pulse amplitude and for the 10% to 90% leading edge "risetime." The resolution for the majority of the following plots is ≈ 200 nsec for the risetime, and 8 bits for the pulse amplitude (≈ 0.4%, or ≈ 25 eV for 6 keV x-rays). Although 10 or more bits will eventually be necessary to resolve the ideal peak (< 10 eV FWHM for 6 keV x-rays), the energy resolution of our devices is not sufficiently high to warrant the extra complexity of 10 bit A/D conversion at present. The pulseheight (collected charge) histograms shown below were computed with one bin per bit (256 bins full scale).

Figure 7.3a shows the energy spectrum obtained with one of our STJ detectors (X-N93) illuminated by ^{55}Fe x-rays. The device employs a 100 μm x 200 μm x 0.6 μm thick Ta absorber. The trap is ≈ 850 μm^3 in volume, overlaps the Ta over a ≈ 10 μm x 100 μm area, and has a ≈ 1800 μm^2 area stretched quartic tunnel junction (J_c ≈ 25 A/cm^2). The junction normal state resistance is ≈ 0.6 Ω, and has ≈ 1 kΩ dynamic subgap resistance at the operating temperature ≈ 0.32 K. The collected charge can be assumed approximately linear in x-ray energy, with the histogram peak corresponding to the 5.9 keV ^{55}Fe x-rays. The peak of the distribution is at ≈ 5 x 10^6

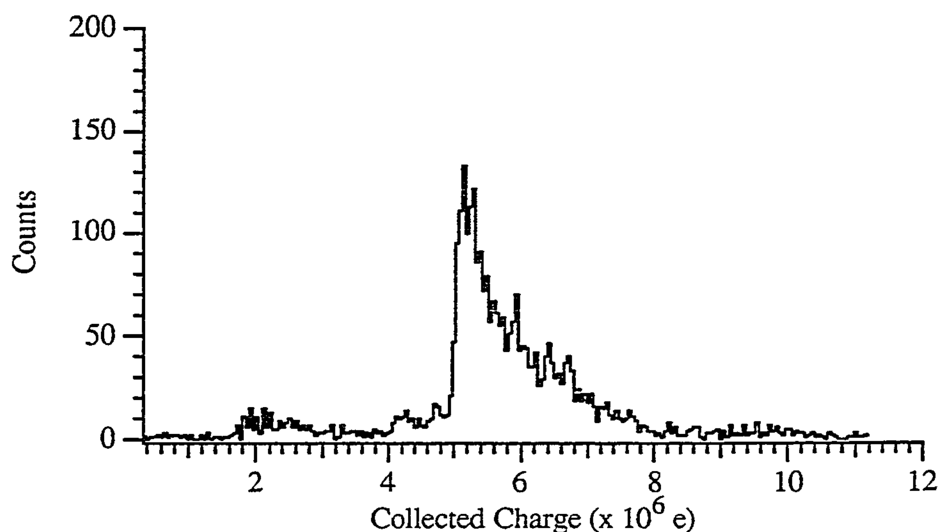

Figure 7.3a: X-ray spectrum from ^{55}Fe x-rays. (X-N93, 3/4/94)

electrons collected, with FWHM ≈ 350 eV. Perhaps more disconcerting than the large FWHM is the "tail" of pulses at high energy instead of a more symmetric peak (at 350 eV FWHM, the 6.5 keV x-rays should not appreciably affect the peak symmetry, actually not even being resolved). This high energy tail is due to x-ray absorptions near the Al trap, and will be discussed in detail in Section 7.4. The sharp low energy edge of the peak indicates that absorption-position-dependent quasiparticle losses are minor (given the broad 350 eV FWHM).

The discrimination level for accepting pulses was set at ≈ 1.8 x 10^6 electrons, thus giving the rolloff in counts below this value. The low number of counts for energies between the discrimination level and the peak at ≈ 5 x 10^6 electrons indicates that substrate absorptions do not give large pulseheights. If substrate events made a major contribution, then a low-energy background, with increasing counts at lower energies, would be evident in the spectrum. The effects of substrate absorptions are discussed in more detail in Section 7.5.

The stability of the junction and the DC biasing can be inferred from Figure 7.3b, where the pulseheights are plotted against pulse number (measured from the start of the data collection; 4000 pulses were collected for the histogram in Figure 7.3a). The horizontal axis is approximately linear in time with ≈ 1 pulse per second measured by the electronics. The pulseheights appear quite stable with time, except for a small time window approximately half way through the run. This is likely a result of an external magnetic field causing temporary DC bias switching to a lower

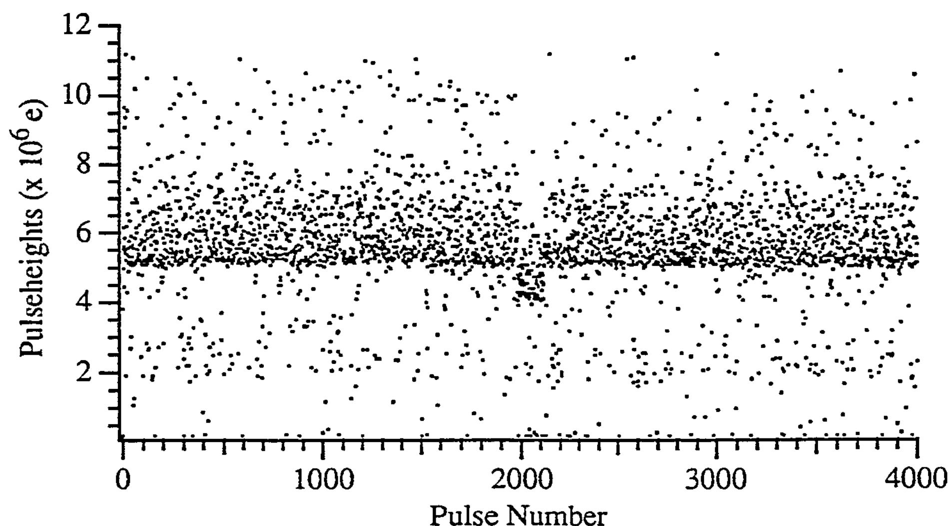

Figure 7.3b: Pulseheights vs. pulse number (≈ 1 pulse/sec). (X-N93, 3/4/94)

resistance. Similar switching occurs approximately once every 3 hours of data collection, and can possibly be eliminated with better device shielding.

The histogram of risetimes for the run of Figures 7.3a and 7.3b is presented in Figure 7.3c. Note the peak in the risetime histogram corresponds to the peak in the pulseheight histogram, as is evident from the pulseheight–risetime plot in Figure 7.3d. The faster pulses correspond to high collected charge, and occur for x-ray absorptions in the Ta region closer to the trap (Section 7.4). Using software to include only the events with risetimes between 14.5 μsec and 16 μsec gives an energy spectrum FWHM ≈ 250 eV, and significantly reduces the number of counts in the high energy tail. The resulting histograms are presented in Figure 7.3e.

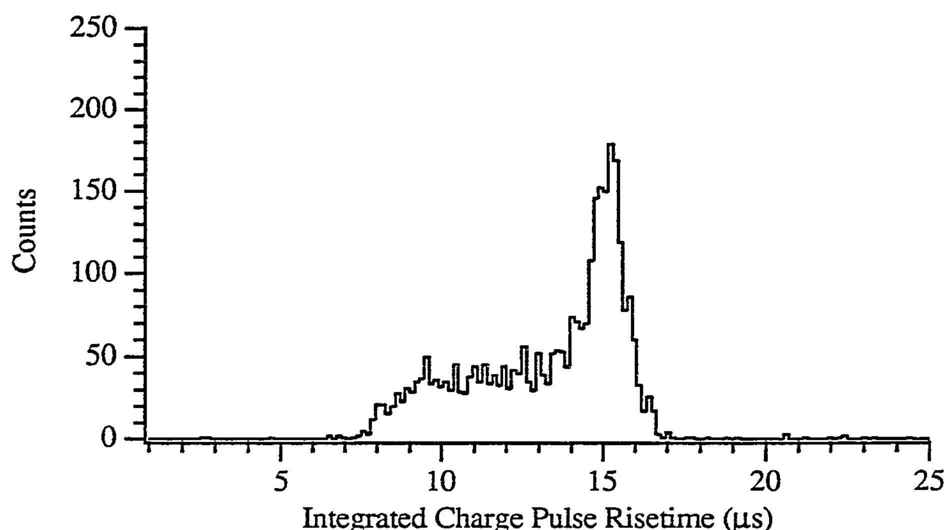

Figure 7.3c: Histogram of charge pulse risetimes. (X-N93, 3/4/94)

As there is a strong peak in the risetime histogram, it appears as though there is some mechanism responsible for the faster pulses which has a rather abrupt change in character for some different initial conditions (e.g., absorptions a certain distance from the trap). The number of counts in the peak of the risetime histogram is approximately 1/2 of the total number of counts, indicating that approximately 1/2 of the Ta absorber is responsible for the fast pulses, and ≈ 1/2 of the absorber is responsible for the slower pulses in the peak. Because of its large x-ray absorption length, the Al in the device should give only a very small contribution to the total number of counts. The change in character of the pulseheight–risetime plot for collected charge greater than ≈ 8×10^6 electrons is indicative of a different

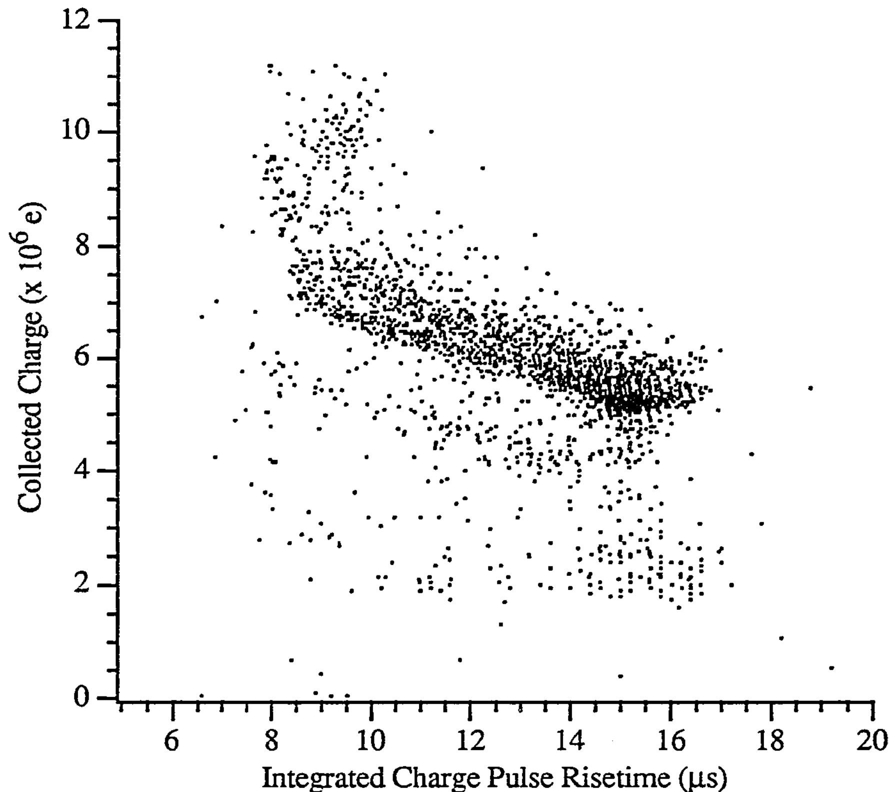

Figure 7.3d: Pulseheight–risetime plot for Figures 7.3a and 7.3c.

quasiparticle collection process, and can probably be assumed to be absorptions in or very near the Al trap. The risetime of such events is probably indicative of the intrinsic behavior of the tunnel junction, i.e., with zero trapping time. This is consistent with a τ_{loss} somewhat less than 8 μsec, which can be accounted for by tunnel time alone, with relatively minimal backtunneling. Such a short loss time would suggest the use of a long trapping time to explain the pulse shapes of Figure 7.2b.

The low energy pulses (< 5 x 10^6 electrons) are primarily due to substrate absorptions, and as such exhibit significant risetime variation. The lowest energy substrate events seem to cluster at slow risetimes, as if the substrate phonons are absorbed in the Ta film. The phonon-created quasiparticles must trap and tunnel as in a typical Ta film x-ray absorption, so they will show comparable pulse risetimes.

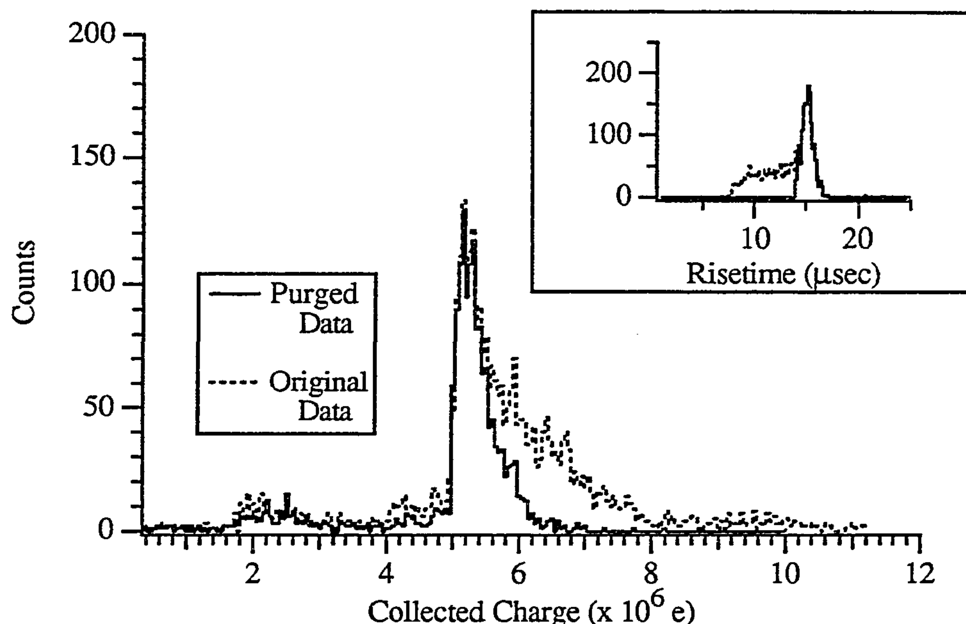

Figure 7.3e: Histograms resulting from software purging of fast risetime pulses. (X-N93, 3/4/94)

7.4 X-Ray Energy Spectra with Trap Masking

From Figure 7.3d, we can infer that the fast risetime pulses are responsible for the bulk of our energy resolution broadening. As it is most probable that the faster events arise from x-ray absorptions in the Ta closer to the trap, we might be able to remove the fast events by preventing x-ray absorptions near the trap. This was done with a 1/32" thick copper foil mounted above the devices such that the Ta within ≈ 50 μm of the trap was not illuminated by x-rays. The energy spectrum resulting from the ^{55}Fe x-rays is presented in Figure 7.4a. The device is identical to the one which produced the histogram in Figure 7.3a, but the operating temperature is slightly lower here, ≈ 0.30 K as opposed to ≈ 0.32 K.

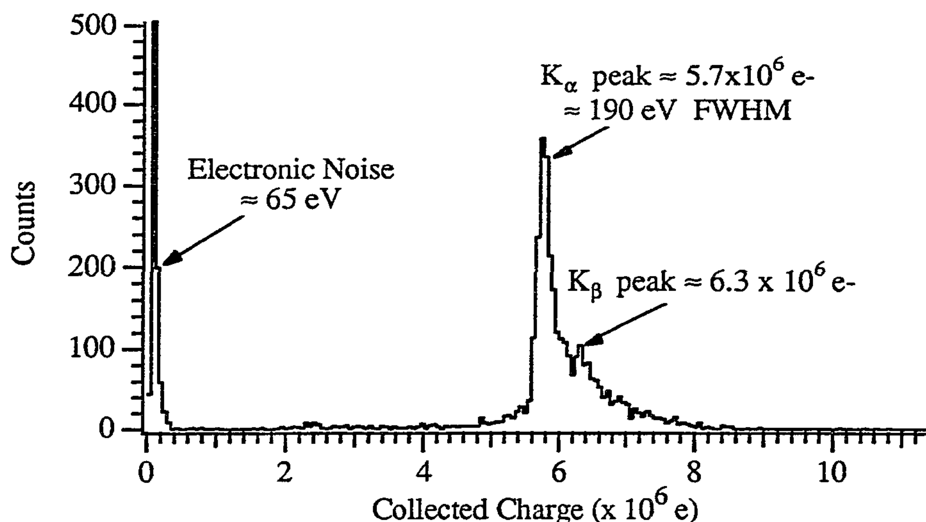

Figure 7.4a: X-ray spectrum for device with trap masking. (X-N93, 3/15/94)

The peak height is slightly larger than that in Figure 7.3a, partly because of the slightly lower temperature, and partly because an amplifier with higher open loop gain was used. The energy resolution is much sharper, ≈ 190 eV FWHM, with a significantly reduced high energy tail. The 6.5 keV x-ray peak can now be seen above the high energy tail. Comparing the 5.9 keV and 6.5 keV peaks, we find that the device linearity is perfect to within the experimental resolution (< 1%). This indicates that quasiparticle self-recombination does not significantly contribute to the quasiparticle losses. In the Al trap, this might be the result of long quasiparticle trapping times (see Figure 3.3.2). In the Ta absorber, phonon trapping apparently increases the effective quasiparticle lifetime such that losses are minimal.

The electronic noise is measured by digitizing auto-triggered scope waveforms (without x-ray pulses, but with the junction connected), and binning the peak height of this "noise" trace. The histogram location of the resulting noise peak gives a measure of the average electronic noise, or approximately the contribution of noise to the x-ray peak's E_{FWHM}. Although this is not a sophisticated method of measuring the contribution of electronic noise to the energy resolution, other methods (such as depositing a calibrated charge on the device, with same pulse shape as the x-ray pulses) are much more complicated, and are unnecessary at present, given the relatively large E_{FWHM} of the x-ray peak. Our measure of electronic noise is

consistent with the derivation in Section 4.1.2, which predicted ≈ 50 eV FWHM broadening from electronic noise.

The energy resolution broadening from electronic noise is much smaller than the observed E_{FWHM} in these masked trap devices. From the discussion in Section 4.1.1, it appears as though one main source of energy resolution broadening is incomplete collection of charge in the charge amplifier.. Because τ_E is only ≈ 60 μsec, and the typical charge pulse leading edge time constant is as much as ≈ 10 μsec, a 1 μsec variation in pulse risetime will give more than 200 eV energy resolution broadening. The risetime histogram (10% to 90%) shown in Figure 7.4b indicates that risetimes do vary by ≈ 1 μsec in this masked device. (Note that the unmasked device exhibits even greater risetime variations.) Risetimes in Figure 7.4b are slightly longer than those in Figure 7.3c because of a larger amplifier open loop gain, and correspondingly larger τ_f^*.

The pulseheight–risetime plot presented in Figure 7.4c, however, reveals that such electronic energy resolution broadening cannot account for the full pulseheight–risetime variation. The 5.9 keV K_α and 6.5 keV K_β lines are broadened even for a single risetime, although this is rather difficult to estimate reliably from such a scatter plot. We also see that the pulses with risetime below ≈ 15 μsec have pulseheights much larger than those with risetime greater than 16 μsec, a difference far greater than would be predicted by a simple electronic effect. We presently believe that these resolution broadening effects are a result of a pulseheight dependence on the (possibly two-dimensional) horizontal absorption position. With the trap masking techniques mentioned in Section 3.4.1, and possibly a constriction in the Ta to eliminate the dependence on the other lateral dimension, we hope to eliminate this energy resolution broadening mechanism.

Based on the marked decrease in the number of fast risetime pulses due to the x-ray mask, we can attribute the fast pulses to x-ray absorptions near the trap region. These absorptions give wide variations in signal height for the same x-ray input energy, and therefore are most undesirable. The success of the crude Cu mask used in this experiment indicates that only small refinements in device geometry and x-ray masking techniques will be necessary to sufficiently remove such signals from the energy spectra.

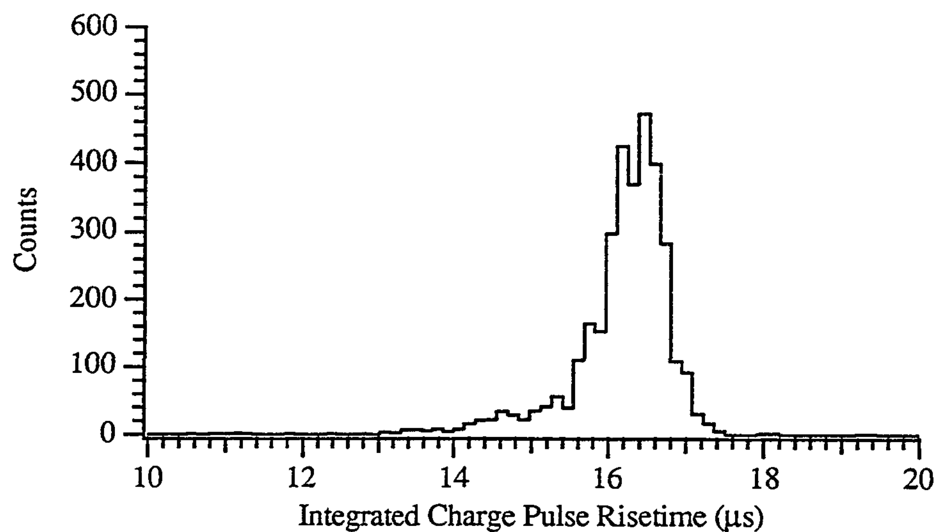

Figure 7.4b: Risetime histogram for the masked trap experiment. (X-N93, 3/15/94)

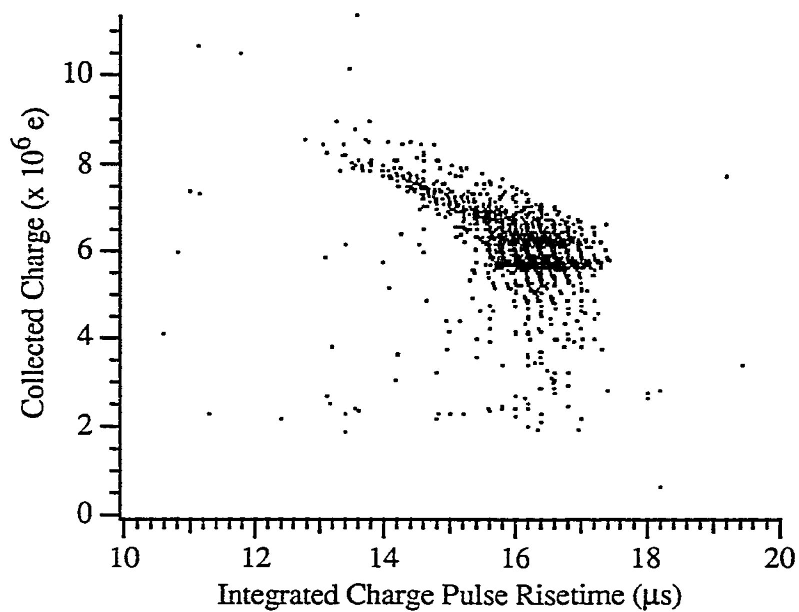

Figure 7.4c: Pulseheight–risetime for the masked trap experiment. (X-N93, 3/15/94)

7.5 Substrate Absorptions

As indicated in Section 7.2, substrate x-ray absorptions result in significantly lower signal than Ta absorptions. A more thorough test of this device characteristic was performed by placing a ≈ 25 μm thick Pt foil above the device, with x-ray illumination of only the substrate and wiring at distances greater than 200 μm from the device. Figure 7.5a presents the resulting pulseheight histogram for ≈ 6 keV x-rays producing signals above the discrimination level (≈ 5×10^5 e). A significant contribution from the substrate events sets in below ≈ 20% of the full pulseheight seen for Ta absorptions (> 5×10^6 e), and a drastic increase in the number of counts is evident below ≈ 15% of the Ta absorption pulseheight. The general shape of the histogram is as expected, with a larger number of counts at lower energies from more distant x-ray absorptions. It is actually somewhat surprising to see so many events at pulseheights > 5×10^6 e, indicating that we might have some phonon focussing[Young, 90], or inadequate shielding from the Pt foil.

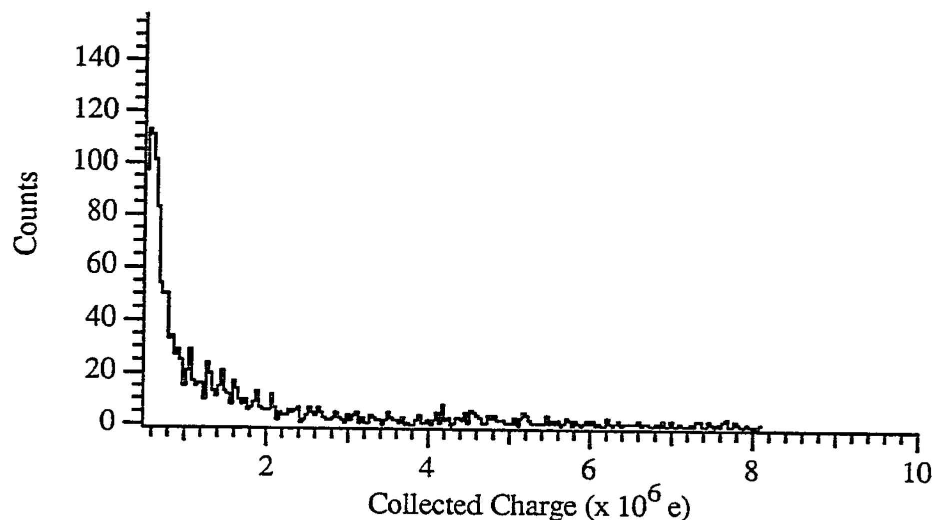

Figure 7.5a: Pulseheight histogram from substrate events. (X-N93, 4/15/94)

The risetime histogram presented in Figure 7.5b (corresponding to the pulseheight histogram in Figure 7.5a) shows two interesting features. The peak at fast risetimes is apparently due to phonon absorption primarily in the Al trap, and the broad peak at slower risetimes is due to phonon absorption primarily in the Ta absorber. It would be inconsistent to assume that the fast events are from phonons absorbed primarily in the Ta, because quasiparticles produced by such phonon

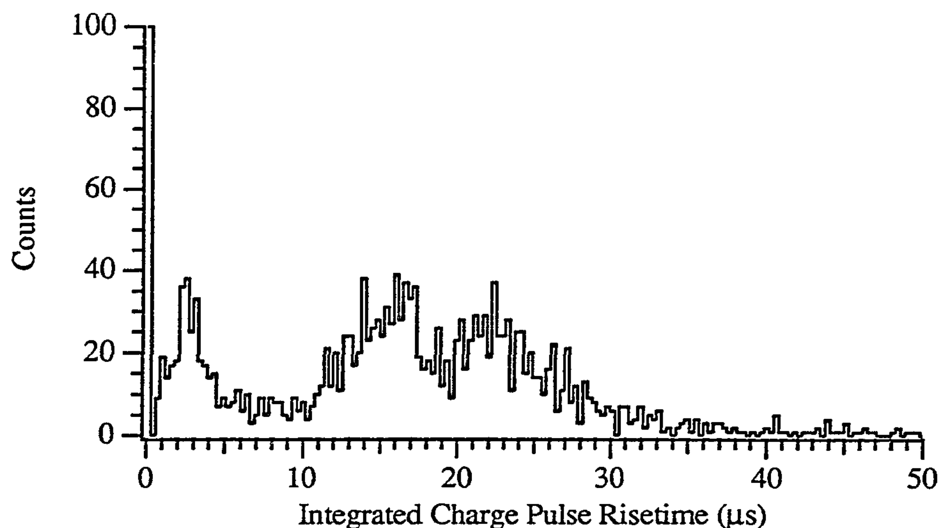

Figure 7.5b: Risetime histogram from substrate events. (X-N93, 4/15/94)

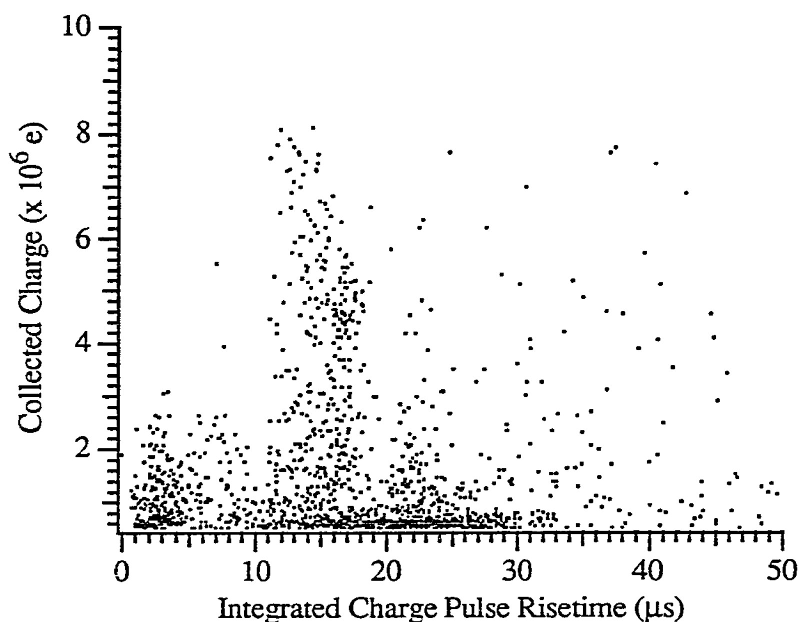

Figure 7.5c: Pulseheight vs. risetime from substrate events. (X-N93, 4/15/94)

absorptions must undergo the additional time-consuming trapping process.

The pulseheight–risetime plot in Figure 7.5c reveals that the faster risetime events result in lower pulseheights, while the slower risetime events are spread over a wide range of pulseheights. The absorption of phonons in the Al is predicted to be much less efficient than the absorption of phonons in the Ta (Section 2.2.3), thus

explaining a consistently low pulseheight for phonons absorbed in the Al, and a somewhat variable pulseheight resulting from phonon absorption in the Ta. The pulseheights from phonons in the Ta will depend on the distance of the x-ray absorption from the device; pulseheights from phonons in the Al will only be above the discrimination level if the x-ray is absorbed nearby.

The relatively low number of counts at risetimes between the fast and slow peaks is consistent with a somewhat directional phonon pulse emanating from the x-ray absorption. This directionality causes the phonon absorption to be dominated by either the trap or the absorber film, giving us two dominant pulse risetimes. Pulses at much longer risetimes than either of the peaks show the effects of nonzero phonon travel times. Based on the maximum phonon velocity in the Si substrate [Kaplan, 79] and the slowest observed pulse risetimes, one can estimate that the most distant detected substrate x-ray absorptions could be observed as far as a half inch from the junction, approximately the size of the device substrate after cleaving into test chips (0.75" x 0.25").

From the above analysis, we find that substrate absorptions are sufficiently suppressed for the detection of 6 keV x-rays. The amorphous SiO_2 film on the substrate appears to perform much better than single crystal substrates in this respect.[Kraus, 91; Rando, 93; Hebrank, 93] However, the intended energy window for these devices is ≈ 100 eV to ≈ 10 keV. With our device, substrate absorptions of the high photon flux iron lines near 6 keV will likely cause significant background counts in the < 1 keV range. It also appears that substrate absorptions as much as 1/2 inch from the device will give such signals. Micromachined substrates or a thorough masking over the entire test chip will probably be necessary to sufficiently reduce the contribution of substrate absorptions.

7.6 Extended Trap Devices

The results presented in the first five sections of Chapter 7 were all taken from one set of identical devices (X-N93), during several cryogenic runs. Two other wafer fabrication runs (X-C93, and X-D94) provided devices which were useful for testing certain aspects of the quasiparticle dynamics in the STJ devices. This section will discuss the X-C93 devices, in which the quasiparticle trapping process is explored through the use of an extended absorber–trap interface. Section 7.7 covers the X-D94 devices, with which we were able to rule out backtunneling as an important process in our devices.

Figure 7.6a schematically illustrates the difference between the extended trap devices (X-C93) and the shorter trap devices discussed previously (X-N93). The primary differences between the two devices are 1) an extended trap in device X-C93 which covers the entire Ta absorber, where in X-N93, the trap only covers ≈ 10 μm of the absorber length, 2) the extended trap device has a slightly thinner Ta absorber: $d_{abs} \approx 0.4$ μm in the extended trap device, compared to $d_{abs} \approx 0.6$ μm in the short trap device, and 3) the normal state junction resistance, R_{nn}, is somewhat lower for the extended trap device: $R_{nn} \approx 0.3\ \Omega$ for the extended trap device, compared to $R_{nn} \approx 0.6\ \Omega$ for the short trap device. The difference in R_{nn} is due to different conditions for the formation of the tunnel barrier (the junction shapes and sizes are identical), and not due to any variation in the length of the absorber–trap interface. Because the trap volume in the extended trap device is significantly larger (≈ 4500 μm^3, compared with ≈ 850 μm^3), the calculated tunnel time will be longer as well: ≈ 8 μsec for the extended trap device, while only ≈ 3 μsec in the short trap device. Note that we do not expect significant trapping from the proximity enhanced Al to the lateral Al because of the small energy gap difference; thus, we have used the full trap volume in the calculation of tunnel time.

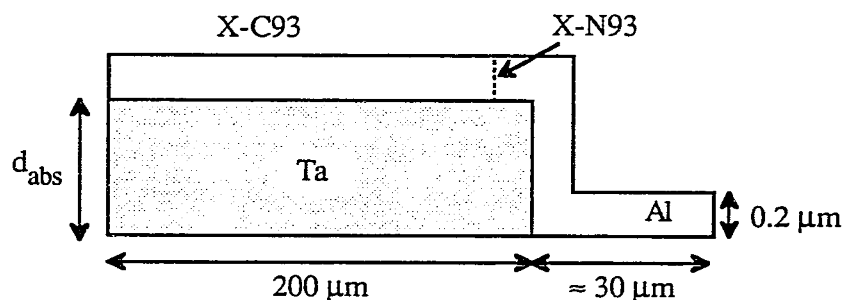

Figure 7.6a: Absorber and trap film geometry in extended trap and short trap devices (side view).

The pulseheight histogram for the extended trap device is presented in Figure 7.6b. Perhaps the most striking feature is the much less efficient charge collection; the 6 keV peak now corresponds to the collection of less than 2 x 10^6 electrons. This can be primarily attributed to the long tunnel time in the device, which allows for more quasiparticle recombination. The peak width is rather broad, probably due to the detection of substrate events and a dependence of signal height on x-ray absorption position (lateral *and* vertical). X-rays absorbed closer to the Al trap might

produce more quasiparticles from the intial hotspot because the diffusion constant is larger in Al, and the electron-phonon coupling characteristics of the Al might make it better for hotspot dissipation than Ta (see Section 2.2.1).

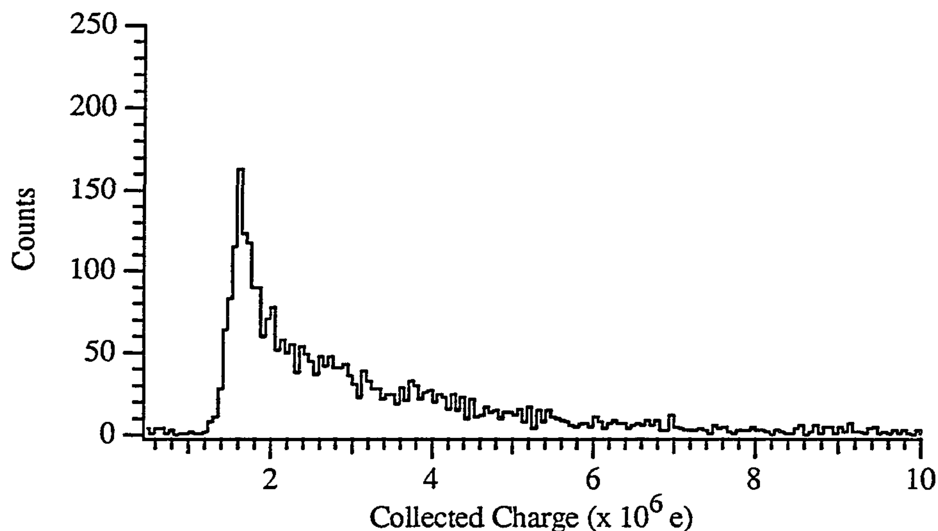

Figure 7.6b: Pulseheight histogram for the extended trap device. (X-C93, 4/12/94)

The risetime histogram for the extended trap device, shown in Figure 7.6c, gives support to the idea that a long trapping time is responsible for the long current pulses seen in the short trap device (Section 7.2). The peak in risetimes for the extended trap device is approximately 8 μsec, which agrees with the calculated 8 μsec tunneling time (assuming some proximity enhancement of the gap in the Al above the Ta). The trapping time for the pulses in this device can be assumed equal to zero on the time scale of interest because of the very large area coverage of a high current density interface. We thus see in Figure 7.6c the result of quasiparticle dynamics primarily in the Al. The majority of quasiparticle pulses exhibit tunneling with $\tau_t \approx 7$ μsec, and do not exhibit backtunneling. If backtunneling were significant, we would expect to see much larger collected charge, and a much larger number of counts at the slower pulse risetimes. In fact, as shown in the pulseheight–risetime plot in Figure 7.6d, the slower pulses generally contribute the same or only slightly more charge. We presently believe that the slower pulses are from substrate events where the phonons must diffuse for long times before reaching the device films. This conclusion is not firm, however, and will require an experiment similar to that in

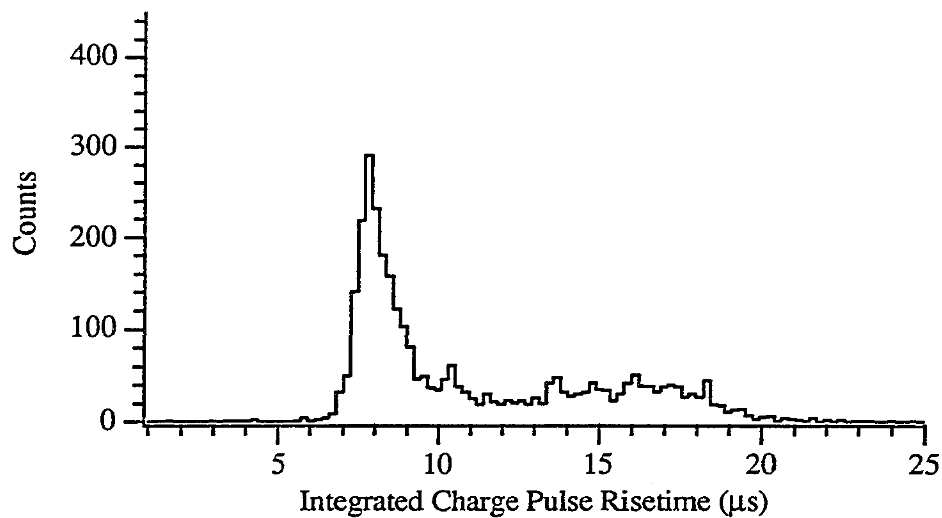

Figure 7.6c: Risetime histogram for the extended trap device. (X-C93, 4/12/94)

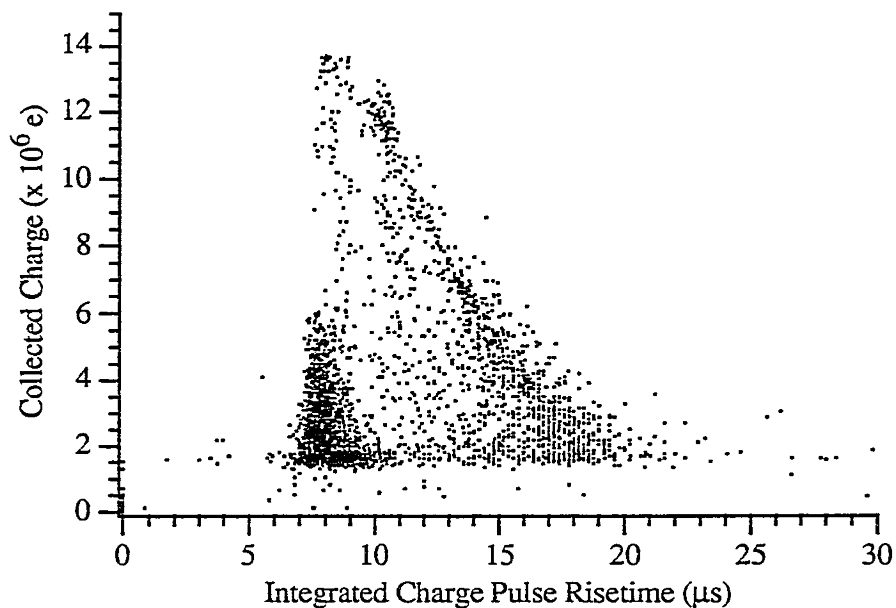

Figure 7.6d: Pulseheight–risetime for the extended trap device. (X-C93, 4/12/94)

Section 7.5 to be verified. It is possible that the Ta film contains some grains surrounded by poorly transmissive grain boundaries, or even some low gap, low diffusion constant regions of β-Ta. The slow pulses could then be a result of x-ray

absorptions in such regions, from which quasiparticles could not rapidly escape to the trap. A device such as the double-junction, one dimensional imaging x-ray detector [Kraus, 89a] might shed some light on such processes.

7.7 Investigation of Backtunneling

Much of the discussion in the previous sections in Chapter 7 gives indication that delayed trapping is responsible for the unexpectedly long charge pulse risetimes we observe. The discussion in this section lends further support to this idea by offering convincing evidence that backtunneling is not responsible for the long pulse risetimes. In addition, by showing that backtunneling is insiginificant, we can infer that the high collected charge in the short trap device (X-N93) is truly indicative of good hotspot dissipation properties in Ta absorber films, and is not due to current gain seen in devices with significant backtunneling.[Mears,93]

The device used in the backtunneling tests (X-D94) is schematically illustrated in Figure 7.7a. There are a few major differences between this device and the one analyzed in the first part of Chapter 7 (X-N93): 1) the absorber–trap interface is approximately half the size in the new device, only ≈ 5 μm x 100 μm instead of ≈ 10 μm x 100 μm, 2) the absorber is slightly thicker in the new device, $d_{abs} \approx 0.8$ μm instead of ≈ 0.6 μm, and 3) the tunnel junction region exhibits significant design changes. The new tunnel junctions are only ≈ 100 μm long stretched quartic shapes (as opposed to ≈ 200 μm long junctions in X-N93), designed to push the Fiske modes up to higher voltages (see Section 6.2). On a single test chip, we have placed devices either with large or with small vias between the counterelectrode and the wiring layer. The large via area is ≈ 150 μm^2, and the small via area is ≈ 20 μm^2. Figure 7.7b better illustrates the effect of the via on the motion of quasiparticles.

If the interface between the Al counterelectrode and the Al wiring layer were a very poor conductor for quasiparticles, nearly identical pulse shapes should result from the two devices because quasiparticles would not outdiffuse appreciably through either via. We can rule out this case because the DC I-V characteristics are identical for the two devices -- in dynamic resistance, normal state resistance ($R_{nn} = 1.6\ \Omega$ in both devices), and magnetic field dependence. Each of these characteristics would be greatly altered if the counterelectrode–wiring interface were the dominant barrier. We would thus be observing the counterelectrode–wiring interface "tunnel barrier" in our DC measurements, which would be different by a factor of ≈ 8 for the two devices.

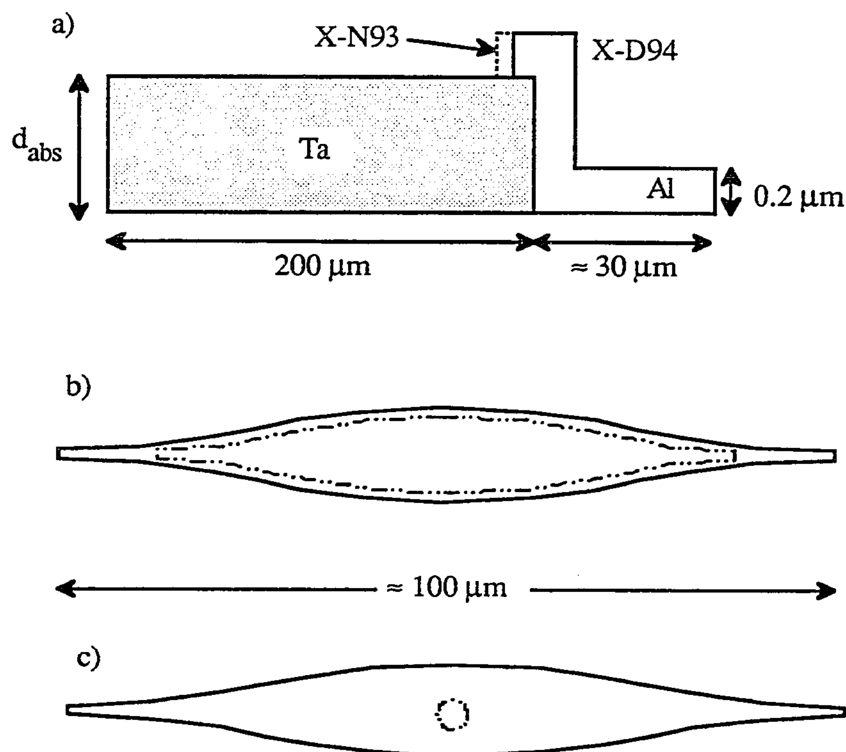

Figure 7.7a: Schematic geometry of device X-D94, used for backtunneling tests. a) Side view of absorber and trap regions (expanded vertical scale). b) Top view of tunnel junction (solid) with large via (dotted). c) Top view of junction with small via.

If backtunneling exists because of a partially reflecting counterelectrode–wiring interface, the small via device should exhibit enhanced backtunneling. If the interface is highly transmissive, backtunneling in the large via device should be minimal, and backtunneling in the small device will only occur if the speed of quasiparticle diffusion out through the via is slow -- which should not be the case for our Al films. Note that this analysis assumes the backtunneling will be negligible for quasiparticles which have travelled into the wiring film. This is almost surely the case, as the ≈ 35 μm wide, 4000 Å thick Al wiring will give rapid quasiparticle outdiffusion (see Section 2.2.7).

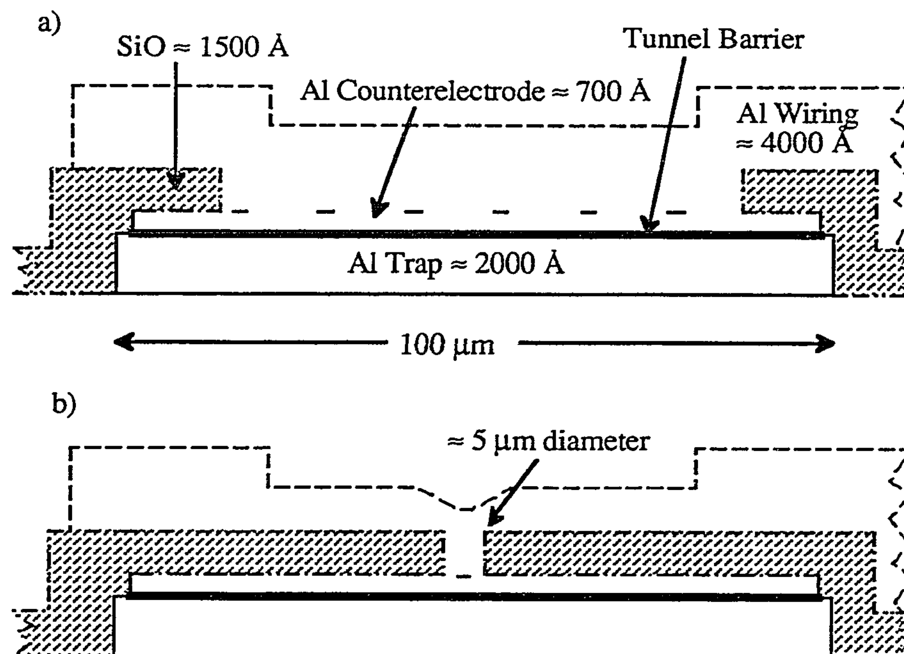

Figure 7.7b: Side view of SiO vias in the two different backtunnel test devices. a) Large via device, and b) small via device.

The arguments from the above paragraph are applicable to the process of *reverse* tunneling in our junctions. Because quasiparticle scattering in Al is relatively slow, many quasiparticles will be able to either backtunnel or reverse tunnel (see Section 2.2.6). The scattering time for quasiparticles in Al at energy $\approx eV_{bias} \approx 80$ μeV above the Al gap will be ≈ 1 μsec.[Kaplan, 76] If the counterelectrode–wiring interface were the major source of quasiparticle reflection, the reverse tunneling time, τ_{rt}, would be only ≈ 0.4 μsec in these devices. As the backtunneling time is actually equal to the forward tunneling time (Section 2.2.6), we have $\tau_{bt} = \tau_t \approx 5$ μsec. After ≈ 1 μsec, most of the quasiparticles in the counterelectrode and wiring films will have scattered to lower energy such that reverse tunneling is no longer allowed, and backtunneling dominates any transmission of quasiparticles from the counterelectrode to the trap. However, in this ≈ 1 μsec, more than 75% of the quasiparticles will have reverse tunneled. Thus, for a partially reflecting counterelectrode–wiring interface, we see that reverse tunneling is a more important process than backtunneling. We can use the same arguments as in the previous paragraph to understand that for *partially* reflecting interfaces, the reverse tunneling current is higher for the small via devices,

and *smaller* pulseheights should result. The charge pulse risetime would be set by quasiparticle recombination, as outdiffusion would not provide a sufficiently fast quasiparticle outlet. *Highly transmissive* interfaces between the counterelectrode and wiring layer, with little or no reverse tunneling or backtunneling, should result in nearly *identical* pulse heights and risetimes for the two different via size devices, provided quasiparticles diffuse through the via faster than τ_{rt}. In either case, the charge signal risetime of the small via devices should be equal or longer to the risetime in the large via devices, because quasiparticle outdiffusion must be more effective in the large via devices.

The pulseheight histograms for adjacent large via and small via devices on a single chip were obtained in the same cryogenic run, at the same temperature, and with the same charge amplifier. These histograms are presented in Figure 7.7c. Due to an error in the setting of the discriminator level, pulses from the large via device were truncated below $\approx 1.1 \times 10^6$ e. A different cryogenic run of large via devices verified that the low energy side of the main peak is nearly equal for small and large via devices, as shown in Figure 7.7d. Note that the histograms in Figure 7.7c were obtained with a Cu mask over the device traps, while the large via device histogram shown in Figure 7.7d was obtained with no x-ray masking. This accounts for the additional high energy pulses recorded for this large via device.

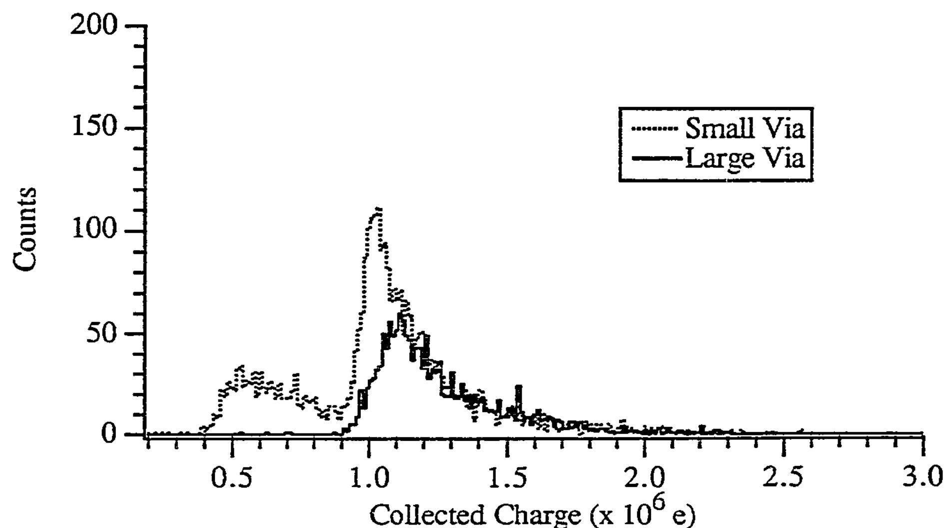

Figure 7.7c: Pulseheight histograms for large and small via devices. A Cu mask was used over both traps. (X-D94, 4/10/94)

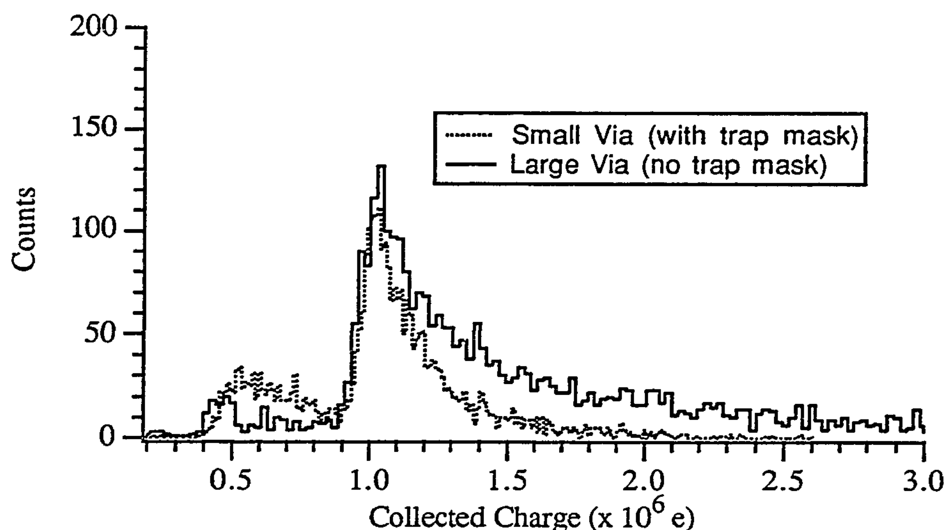

Figure 7.7d: Pulseheight histograms for small via device and a large via device from different cryogenic runs. (X-D94, 3/25/94, 4/10/94)

The low energy pulses in the small via device are likely from substrate absorptions, with phonons pair-breaking in the Al trap. Similar substrate pulses are seen in the adjacent large via device, as is evident from the risetime histogram in Figure 7.7e, and the pulseheight–risetime plots in Figures 7.7f and 7.7g. Because such events are visible, we can infer one of two conclusions: the amorphous SiO_2 layer on this wafer does not effectively reduce the effect of substrate absorptions, or there are significant quasiparticle losses in the Ta absorbers, so x-ray absorptions in the Ta deliver charge to the trap comparable to that produced by pair-breaking phonons in the trap from substrate absorptions. A substrate absorption test similar to that in Section 7.5 will be necessary to verify that these are indeed substrate absorptions, and a double junction test [Kraus, 89a] will be necessary to evaluate quasiparticle losses in the Ta absorber.

The obvious similarity in pulseheights and risetimes between the small and large devices gives strong evidence that we do not have additional backtunneling or reverse tunneling greater than the resolution of the experiment ($\approx 1\%$). These devices were processed nearly identically to the previously discussed X-N93 devices, so we can infer that the X-N93 devices have little or no reverse tunneling or backtunneling as well. The relatively low charge collection efficiency in the backtunnel test devices might result from a combination of longer tunneling time (increased trap quasiparticle

recombination), and poor quasiparticle trapping due to a smaller area absorber–trap interface (increased quasiparticle losses in the Ta).

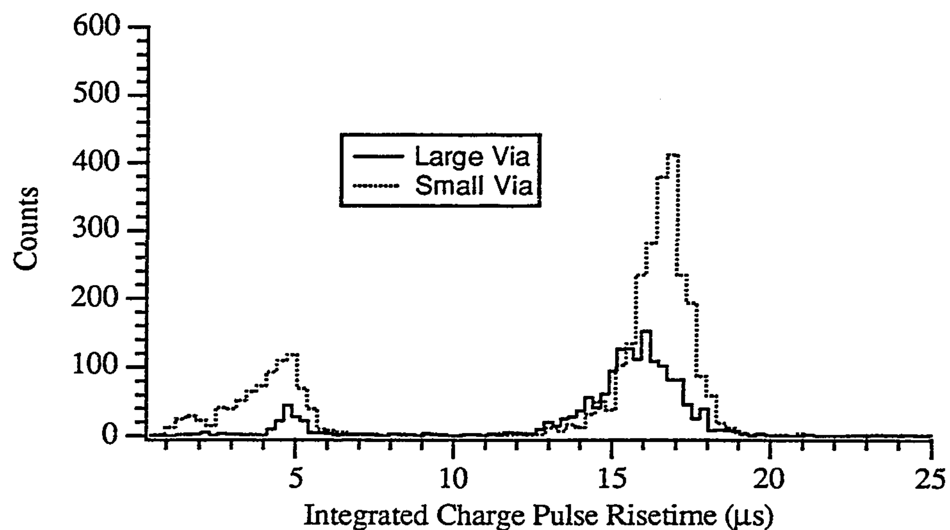

Figure 7.7e: Risetime histograms for small and large via devices. (X-D94, 4/10/94)

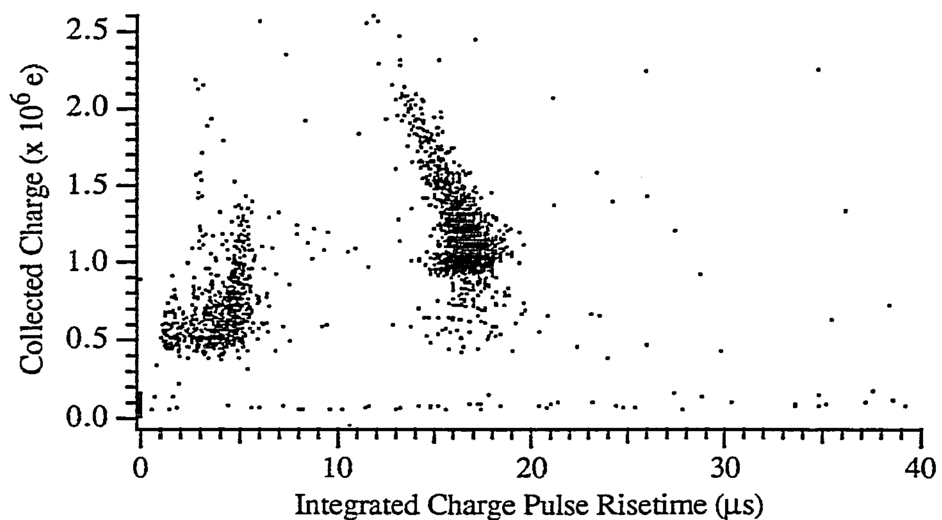

Figure 7.7f: Pulseheight–risetime plot for the small via device. (X-D94, 4/10/94)

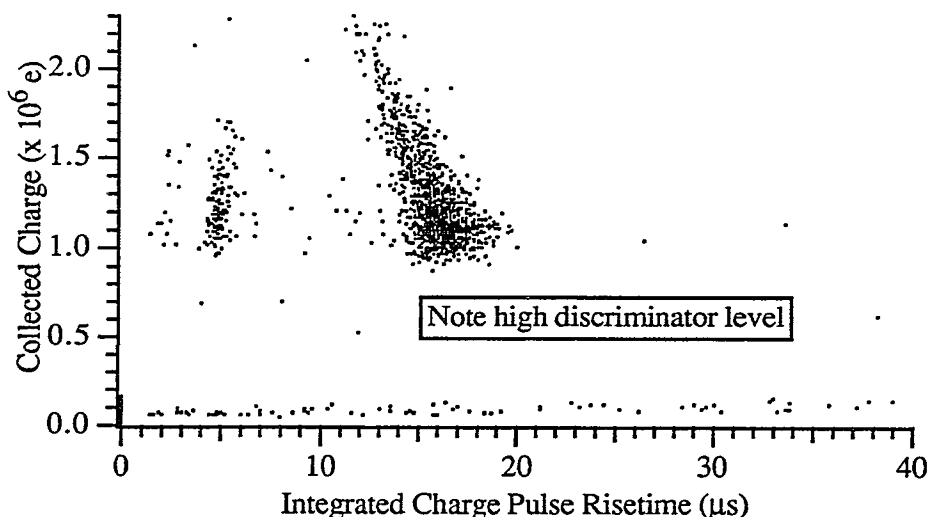

Figure 7.7g: Pulseheight–risetime plot for the large via device. (X-D94, 4/10/94)

7.8 Discussion

It is apparent that the quasiparticle trapping process is critical to the response of the devices. Unfortunately, it is one of the least well understood processes in the device. With new devices in the near future, we will focus on understanding this process and how sensitive it is to the various processing techniques used in device fabrication. Even with our present limited understanding, we can report some important successes from our devices.

The charge creation and collection in our devices appears quite efficient. With even the poorest devices delivering more than one million electron charges for a 6 keV x-ray absorption, the predicted Fano-factor limited energy resolution is *significantly* better than in semiconducting *p-n* junction detectors. The best devices deliver $\approx 5 \times 10^6$ electron charges. It is reasonable to assume that backtunneling (and reverse tunneling) in these devices is negligible, so we can infer that Ta films are very effective x-ray energy-to-quasiparticle converters. Taking a high estimate of $\approx$ 20% quasiparticle multiplication upon trapping, we find that *at least* 4×10^6 quasiparticles are produced in the Ta by a 6 keV x-ray. This gives a minimum ionizing energy $\varepsilon \approx 2\Delta_{Ta}$, assuming we collect every charge produced. In fact, simulations of premature pulse decay from a "low" gain amplifier (Chapter 8) indicate that as many as 6.2×10^6 quasiparticles are produced in the Ta after the initial hotspot, giving $\varepsilon \approx 1.4\Delta_{Ta}$.

This implies that more than 70% of the x-ray energy resides in the Ta quasiparticle system after the hotspot dissipation.

Although the measured energy resolution of the devices is far from the Fano-factor limit, several other aspects of our devices make them potentially useful for x-ray astronomers. The absorption efficiency is greater than 25% for the device with the best energy resolution, and as high as 35% for other devices. Device performance does not appear to set a limit on the thickness of the Ta absorber film, indicating that absorption efficiencies greater than 50% are certainly realistic. In addition, the absorber and trap geometries we have chosen will allow us to scale the devices to larger areas, realistically offering 0.5 mm x 100 μm absorbing regions. The speed of quasiparticle diffusion in the Ta might be the only limiting factor, and must be experimentally analyzed. If Ta quasiparticles scatter to the gap edge faster than predicted by Kaplan *et al.*[76], significant reduction of quasiparticle velocity and diffusion constant can be expected. If necessary, high purity epitaxial Ta films (on crystalline substrates) may be purchased from an outside vendor to give us higher diffusion constants.

The risetime histograms of the X-N93 and X-D94 devices are somewhat difficult to interpret. If the long charge pulse risetimes were due simply to slow Ta quasiparticle diffusion, one would not expect such a sharp peak in the risetime histogram for the slow pulses (with risetime > 15 μsec). Because the diffusion time is a continuous variable in diffusion distance, one would expect a broad, almost featureless peak in the risetime histogram. If, however, the absorber–trap interface forms the bottleneck in the trapping process, a sharp peak would result. This peak would have width determined by the diffusion time of quasiparticles across the entire absorber (≈ 1 μsec), and would be quite sharp for very fast diffusion. If the trapping time is indeed somewhat larger than 10 μsec because of a poor interface, diffusion should be rapid enough to make the peak width somewhat less than 1 μsec. This explanation is reasonably consistent with the results we observe, but the current density tests of our absorber–trap interfaces set the trapping time closer to 1 μsec than 10 μsec.

Quasiparticle trapping in our devices is thus somewhat unpredictable, and will require a good deal of experimental testing before we can understand all the processes involved. Whether the problem is slow Ta quasiparticle diffusion, or a poor interface, we can infer that the tunneling time of the device is indeed set by the volume of the trap. Tunnel times of ≈ 45 μsec would result from the large volume Ta absorber if trapping were not present. Thus, the lower gap trap film in our devices

appreciably prevents the trap quasiparticles from re-entering the absorber film. The collected charge from our devices appears rather sensitive to the tunnel time, implying significant quasiparticle recombination in the trap. Quasiparticle lifetime tests similar to that of Hsieh and Levine [68] should be performed on the absorber and trap films to ascertain the nature of our quasiparticle recombination and diffusion.

One other somewhat unpredictable process in our devices involves the correlation of higher pulseheights with x-ray absorptions near the trap. This is most likely attributable to $\Delta_{Ta} > \Omega > 2\Delta_{Al}$ phonons breaking pairs in the trap. What is not presently understood is how such phonons can have such a large influence from absorptions as much as 50 μm away from the trap. If these phonons are produced near the hotspot region, they will have a very large probability of entering the substrate before reaching the trap. Thus, the large signal response we see from distant x-ray absorptions might be due to one of at least three possibilities: 1) the phonons do enter the substrate, but somehow are focussed back into the trap; 2) the phonons do not enter the substrate, but exhibit some degree of total internal reflection at the Ta-SiO_2 interface, and thus travel directly to the trap; or 3) the high energy quasiparticles emerging from the hotspot can diffuse large distances before they emit relaxation phonons, and might be stimulated to emit such phonons as they contact the absorber–trap interface. We believe process number 3 is the most probable explanation for the pulseheight variation we see. Note that such high energy quasiparticles can diffuse directly into the trap before emitting relaxation phonons. These phonons will typically have higher energy than relaxation phonons from Ta gap edge quasiparticles, and therefore might be more effective in quasiparticle multiplication upon trapping. In any case, it appears likely that our devices will require some variant of the x-ray masking techniques covered in Section 3.4.1.

It is clear that there are several important experiments which must be performed to better understand the performance of our devices. The dynamics of the quasiparticle diffusion and trapping must be better understood. As varied device geometries must be used to test such processes, device response will not always be related to a single "control" sample. Thus, device response should be evaluated separately for each different test. Such investigations of our devices are underway, particularly to better understand the response of the long trap device (Section 7.6), and the backtunneling test devices (Section 7.7). Because the collected charge from x-ray absorptions in these devices is only marginally larger than the collected charge originating in substrate absorptions, we can learn a good deal from device tests with completely masked STJs. Substrate absorptions will send phonons to the absorber or

the trap, allowing us to observe the different pulse responses with or without quasiparticle transmission through the absorber–trap interface. In addition, we can perform measurements on "short" trap devices fabricated on the same wafer as the long trap devices, potentially allowing us to deconvolve the effects of absorber–trap interface area. Finally, the very useful approach of computer modelling can potentially give us reliable information, and dictate the necessary device geometries we must use for our tests.

8. Computer Simulations of Junction Response

The STJ x-ray detectors are very interesting devices because they rely on the interaction of a great number of different processes: quasiparticle generation, quasiparticle recombination, phonon trapping, quasiparticle diffusion, quasiparticle trapping, quasiparticle tunneling, quasiparticle outdiffusion, and quasiparticle backtunneling are the most important. Obviously, it will be quite difficult to analytically solve for the device charge output based on the interaction of all of these processes. The use of computers to numerically simulate the essential processes is straightforward, and gives us valuable intuition regarding these complex processes in our device.

8.1 The Equations of State

Our model is based on the iteration in time of the equations of state describing our device. This method has been proven successful in describing simple tin–tin oxide–tin tunnel junctions without bandgap engineering.[Twerenbold, 86b] We have extended the model to include the effects of quasiparticle trapping, and have adapted it for our specific film geometries. Based on the discussion in Chapters 2, 3, and 4, we can derive equations of state for the four quantities of interest:

$N_{abs}(t)$	Number of quasiparticles in the absorber
$N_{tr}(t)$	Number of quasiparticles in the trap
$N_{\Omega tr}(t)$	Number of $\Omega > 2\Delta_{tr}$ phonons in the trap
$Q(t)$	Charge on the amplifier feedback capacitor.

The charge on the feedback capacitor as calculated from the simulations can be compared directly with the digitized integrated charge pulse from our experiments. The computer model actually keeps track of the number of quasiparticles and phonons in the counterelectrode, but, as backtunneling and reverse tunneling are found negligible, we will not discuss the counterelectrode here. Our computer simulations do not explicitly calculate the hotspot dissipation dynamics, but rather use an intial number of quasiparticles in the absorber as a free parameter. These quasiparticles are assumed at the absorber gap edge, so there is no explicit energy dependence in the equations. Dropping the explicit time dependence for brevity, the equations of state are

$$\frac{\partial N_{abs}}{\partial t} \approx -\frac{N_{abs}}{\tau_{trap}} - \frac{R_{abs} N_{abs}^2}{V_{abs}} ,$$

$$\frac{\partial N_{tr}}{\partial t} = \frac{N_{abs}}{\tau_{trap}} + \frac{2 N_{\Omega tr}}{\tau_{pb}} - \frac{N_{tr}}{\tau_t} - R_{tr}\left(2 N_{tr} n_{th} + \frac{N_{tr}^2}{V_{tr}}\right) ,$$

$$\frac{\partial N_{\Omega tr}}{\partial t} = 0.33 \cdot \frac{N_{abs}}{\tau_{trap}} + \frac{R_{tr}}{2}\left(2 N_{tr} n_{th} + \frac{N_{tr}^2}{V_{tr}}\right) - \frac{N_{\Omega tr}}{\tau_{pb}} - \frac{N_{\Omega tr}}{\tau_{esc}} ,$$

$$\frac{\partial Q}{\partial t} = \frac{q N_{tr}}{\tau_t} - \frac{Q}{\tau_E} ,$$

where τ_{esc} is the escape time for phonons from the trap (and includes the minor effects of anharmonic decay), and the 0.33 factor accounts for phonon emission upon quasiparticle trapping (assuming a flat phonon emission spectrum). Phonon trapping in the absorber must be included by decreasing R_{abs}, and background thermal recombination in the absorber is assumed negligible. Phonon trapping in the trap is accounted for by the pair-breaking and phonon escape terms.

The parameters used for a first simulation of the device X-N93 are listed below:

$N_{abs}(0)$	7.5×10^6
τ_{trap}	2 μsec
R_{abs}	260/170 = 1.53 μm^3/sec
V_{abs}	11,000 μm^3
τ_{pb}	240 psec
τ_t	3.15 μsec
R_{tr}	9.6 μm^3/sec
n_{th}	6000 μm^{-3}
V_{tr}	840 μm^3
τ_{esc}	75 psec
τ_E	55 μsec

Double precision variables were used to keep track of the various quantities, and the iteration time interval was 40 psec. This was verified to be short enough by tests with 10 psec iteration times.

8.2 Comparison with Experimental Pulses

The parameters used in the "first" simulation above returned qualitatively reasonable results, and allowed us to modify certain parameters to observe their

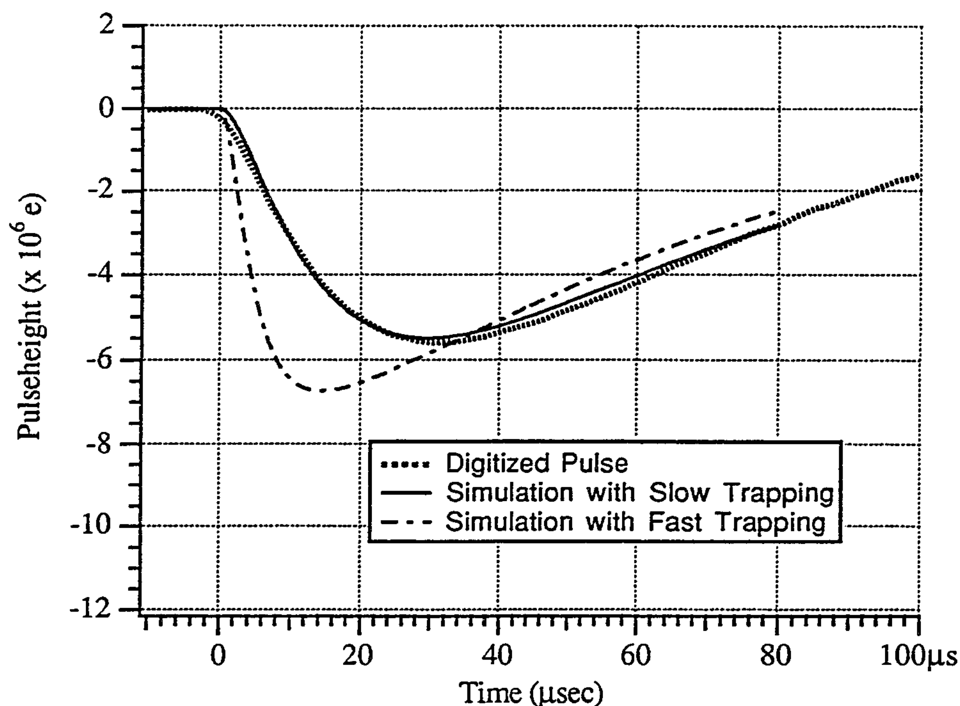

Figure 8.2: Computer simulation of x-ray induced integrated charge pulses. The fast trapping curve is found with the parameters listed in Section 8.1; the slow trapping curve is obtained with τ_{trap} = 12 µsec.

effects on the output charge Q(t). As displayed in Figure 8.2, the "first" simulation with fast trapping (τ_{trap} = 2 µsec) gives a much poorer fit to a typical data pulse than a simulation identical except for longer τ_{trap} (= 12 µsec). The quality of the fit gives us much confidence that slow trapping is indeed responsible for the unexpectedly slow charge pulse risetimes. Note that including large amounts of backtunneling and reverse tunneling in the simulations gives qualitatively similar fits, but these effects are not expected to be important in our devices, as discussed in Section 7.7.

8.3 Quasiparticles and Phonons in the STJ Detector

The computer simulation allows us to follow the quasiparticle and phonon distributions in the device as a function of time, giving us some insight into the device dynamics. The plots in Figures 8.3a and 8.3b give the number of quasiparticles in the absorber and in the trap, and the number of phonons in the trap for the τ_{trap} =12

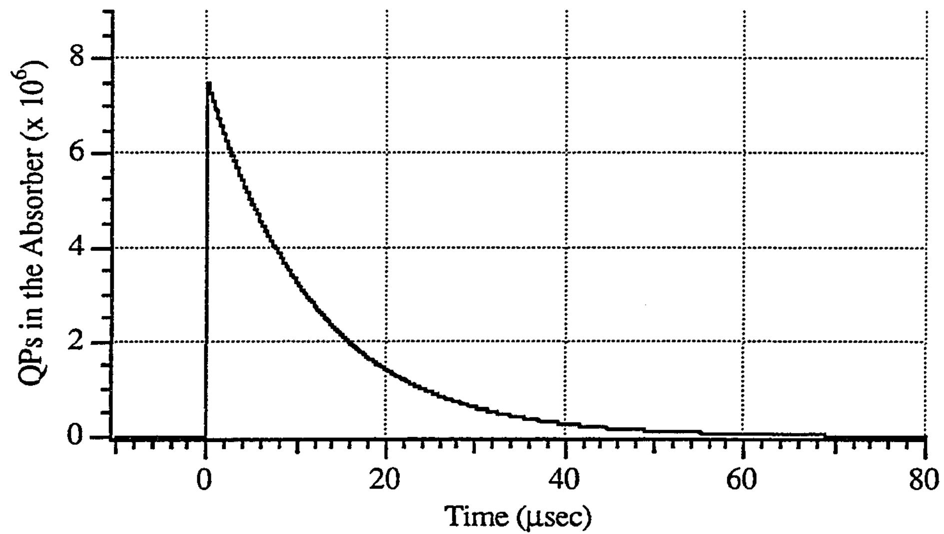

Figure 8.3a: Number of quasiparticles in the absorber as a function of time.

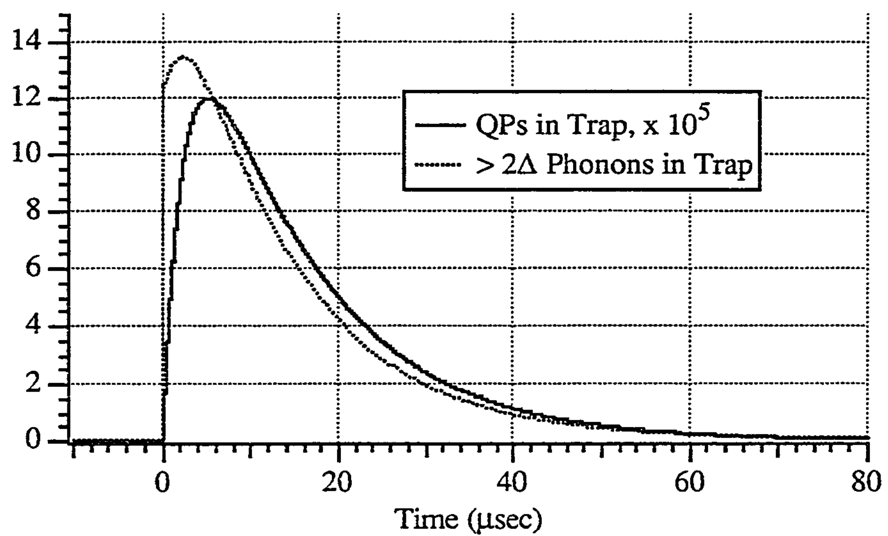

Figure 8.3b: Number of quasiparticles and phonons in the trap as a function of time.

µsec simulation. As expected, the recombination in the absorber is relatively minor, and N_{abs} closely approximates an exponential with decay time of 12 µsec. The more interesting data involves the quasiparticles and phonons in the trap. It is striking to see the huge difference in populations between the quasiparticles and $> 2\Delta$ phonons in the trap (note the x 10^5 in the quasiparticle vertical scaling). This can of course be explained by the very fast pair-breaking time of such phonons. The number of quasiparticles in the trap remains below $\approx 1.2 \times 10^6$, with the slow trapping and relatively fast tunneling keeping the population at this relatively low level. This indicates that the quasiparticle self-recombination in the Al trap will be significantly lower than the background thermal recombination, even for temperatures as low as 0.25 K. We therefore can benefit by operating our devices in a dilution refrigerator at somewhat lower temperatures.

Note that the quasiparticle population in the trap peaks at $\approx$ 7 µsec, and remains large even after 20 µsec. Obviously, the relatively short amplifier decay time constant τ_E will result in incomplete charge collection.

8.4 Effects of Amplifier Electronics

Figure 8.4a illustrates the incomplete charge collection resulting from such a short electronic decay time constant. Each simulation is identical ($\tau_{trap} = 12$ µsec) except for τ_E. The computed results indicate that our device would deliver a charge of $\approx 7.5 \times 10^6$ electrons if the amplifer were better matched to the device. This implies that the Ta absorber must be extremely efficient in converting x-ray energy to quasiparticles, with only $\approx$ 10% of the initial x-ray energy being lost in subgap phonons. It is clear that we must focus on increasing the junction dynamic resistance and the amplifier open loop gain to determine if the device will actually deliver this much charge.

Such improvements in the amplifier will also help to increase the energy resolution of the devices. Figure 8.4b shows the results of computer simulations of pulses with slightly different trapping times, with variation similar to that seen experimentally in our device (Section 7.3). Such different trapping times might result if slow quasiparticle diffusion were responsible for the long trapping time. From the simulation, we find a peak pulseheight variation of slightly more than 4%. This is not as dramatic as the simplified model of Section 4.1.1 predicts, but nonetheless shows an extremely damaging effect on device energy resolution.

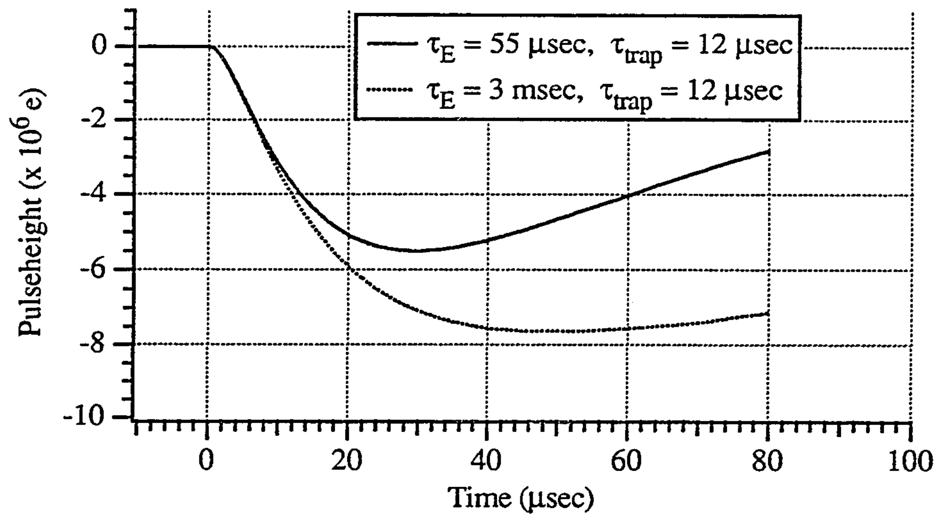

Figure 8.4a: Computer simulation of the effects of electronic decay time constant on pulseheight.

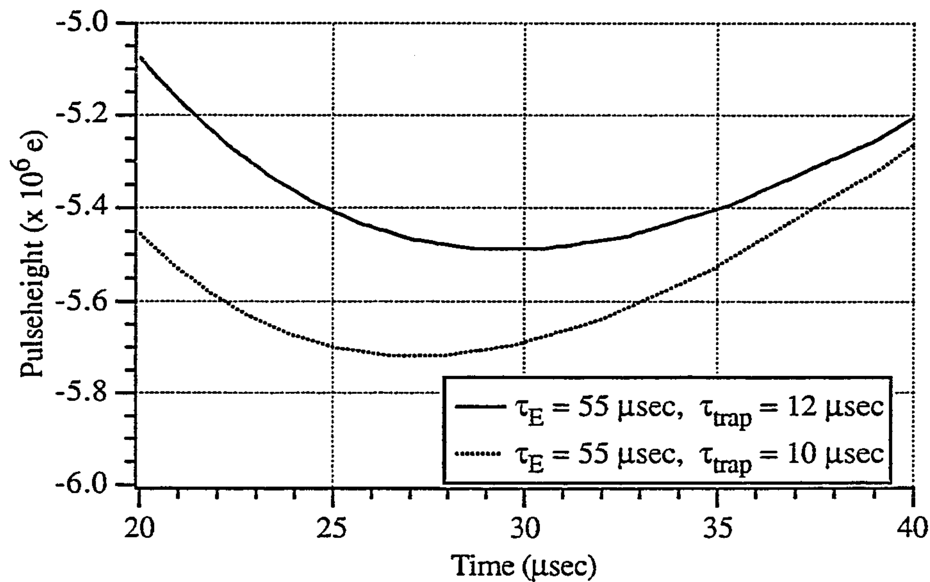

Figure 8.4b: Computer simulation of pulseheight variation with trapping time. The scale is expanded to emphasize the difference in peak pulseheight.

8.5 Discussion

The use of computer simulations to model our devices has proven useful, but by no means has been utilized to its full capability. It would be quite helpful to model the initial hotspot creation of quasiparticles to determine better just how effective Ta is in converting x-ray energy to quasiparticles -- and whether or not 90% efficiency is truly possible. The computer simulations also have not yet been used as device design tools. In the near future, our group will use them to explore the effects of film geometries and tunnel junction current densities. Work has also started on the understanding of Fiske modes in our nonstandard tunnel junction geometries. Our limited understanding of the devices at present indentifies slow quasiparticle trapping as responsible for the unexpectedly slow charge pulse risetimes. Computer models of the quasiparticle diffusion and trapping process should be developed to give insight into the mechanisms responsible for the slow pulses. Also, computer modelling of the other devices reported in this work might be helpful in understanding the wide variation in observed x-ray absorption response.

Despite their simplicity, the early attempts at computer modelling shown in this chapter have given us some valuable information. We have verified that the slow pulses we experimentally observe must be the result of some mechanism which lengthens the quasiparticle residence time on the trap side of the tunnel barrier. It is most likely that slow quasiparticle trapping is this mechanism. We have found that quasiparticle self-recombination in our traps should be negligible at temperatures above 0.25 K. Simulations with faster (2 μsec) trapping also indicate negligible self-recombination. In addition, we have verified the simple model of Section 4.1.1 which predicts severe energy resolution broadening for variable risetime pulses, given short electronic decay time constants. From these simulations, we feel that *major* improvements in our device energy resolution can be obtained with relatively simple modifications to the experiment, namely, improvements in the pulse amplifier electronics.

9. Conclusion

We have demonstrated successful x-ray detection with relatively complex superconducting tunnel junction structures. Our devices have been designed to satisfy x-ray astronomers' needs for high absorption efficiency, large area films and for high energy resolution. We have demonstrated that reliable devices can be produced with high efficiencies and large areas. The robust nature of the refractory materials used in the device allows repeated thermal cycling and little worry of device degradation with time. The energy resolution of these devices, however, is less than ideal, and will form the focus of future work in this group. With our present understanding, we do not feel the broad energy resolution is an intrinsic device property, but rather should be improved with only minor changes to the device and the amplifying electronics. Section 9.2 outlines experiments which should resolve many of the remaining puzzles in these devices.

We have attempted to optimize nearly every aspect of the charge creation and collection processes. Superconductor bandgap engineering is extensively used to modify the nature of quasiparticle transport, enhancing tunneling and preventing outdiffusion. Substrate effects are altered through the use of an amorphous SiO_2 surface layer. Shaped tunnel junction geometries are chosen to improve the DC biasing of the devices. While these design issues have resulted in improved device performance, they also make the device somewhat more difficult to analyze. The project in our group has successfully demonstrated a proof of concept, and now must continue by dissecting each process in the device to determine how we can improve the energy resolution.

9.1 Comparison with Other Work

Table 9.1 outlines most of the important device characteristics as reported by several of the groups involved in STJ x-ray detector development. While no group can yet report energy resolution near the $\approx$ 10 eV desired by astronomers, several device designs do show promise. The devices of Kraus *et al.*, Kurakado *et al.*, and Mears *et al.*, for instance, all exhibit energy resolutions limited by the electronic noise of the charge amplifier. For this reason, it appears as though energy resolution is not a major deficiency in any of these devices; simply with more effort in reducing electronic noise, these devices might offer energy resolution much closer to 10 eV.

Reference	Device Type	T_{op}	E_{FWHM} (6 keV)	Abs. Eff. (6 keV)	Thermally Cycles?	Collected Charge	Good for Large Area?	Note
This Work	Nb-Ta-Al-AlOx-Al	0.3 K	190 eV	≈ 30%	Yes	> 5 x 10^6	Yes	
Kraus, 89a	Pb-Sn-Al-AlOx-Al	0.1 K	60 eV	< 15%	No	≈ 5 x 10^5	Yes	1
Kurakado, 92b	Nb-Al-AlOx-Al-Nb	0.4 K	88 eV	≈ 10%	Yes	< 4 x 10^5	?	2
le Grand, 94	Nb-Al-AlOx-Al-Nb	1.2 K	≈ 250 eV	≈ 8%	Yes	≈ 5 x 10^5	?	
Mears, 93	Nb-Al-AlOx-Al-Nb	0.2 K	35 eV	< 25%	Yes	≈ 8 x 10^6	?	3
Twerenbold, 87	Sn-SnOx-Sn	0.3 K	90 eV	< 20%	?	≈ 2 x 10^6	No	4
Videler, 93	Nb-Al-AlOx-Al-Nb	1.2 K	130 eV	≈ 2.5%	Yes	≈ 8 x 10^5	?	
Nahum, 93	Hot Electron NIS	0.05 K	≈ 100 eV	≈ 40%	?	N.A.	?	5
McCammon, 90	Microbolometer	0.1 K	≈ 10 eV	> 75%	Yes	N.A.	Yes	6

Table 9.1: Comparison of our results with those of several competing groups. Shaded table cells indicate major deficiencies in device performance for x-ray astronomy.

Notes for Table 9.1

1) These devices use a double-junction geometry which allows one-dimensional imaging, and correction for quasiparticle losses in the absorber.
2) These results are from a $\approx$ 178 μm x 178 μm device; its capacitance is a major factor in the nonideal energy resolution.
3) Backtunneling is used in these devices to enhance the collected signal charge by a factor of $\approx$ 3.5. This will limit the energy resolution of the device to no better than $\approx$ 15 eV.[Mears, 93]
4) These devices use no quasiparticle trapping, and exhibit excessive losses out the leads. In addition, base and counterelectrode films give similar, but different, signal charge for absorbed x-rays.
5) This device is a thin film NIS junction operating as a hot electron detector (microcalorimeter).
6) This device is a micromachined calorimeter, which might be difficult to incorporate into imaging arrays. The relevant thermal time constants involved in the device operation limit incident photon rates to < 10 /sec.

Even the devices which show promising energy resolution exhibit some problems which make them less than ideal for x-ray astronomy. The Pb-Sn-Al-AlOx-Al devices fabricated by Kraus *et al.* are in principle quite similar to ours, but exhibit one major defect: the Sn–Al film interface does not survive themal cycling intact. This is unacceptable for space-qualified devices, as one must first test the devices on the ground. To give positional information, these devices utilize two junctions at opposite ends of a single absorbing film. Pulses will be observed in both junctions for each single x-ray absorption, and the ratio of pulseheights in the two junctions will give an indication of the absorption position. Adequate characterization of the devices also allows one to correct for quasiparticle losses in the absorber during the diffusion to the traps. We find such a device design to be extremely useful in device diagnostics, and eventually in imaging arrays of large area devices. Thus, we will adapt this structure in our future devices.

All of the Nb trilayer devices are rather similar in operation, and exhibit two potential deficiencies in scaling them up to sizes necessary for x-ray astronomy. Firstly, because of the long x-ray absorption depth in Nb, very thick films will be

necessary to ensure adequate absorption efficiencies. Almost 3 μm thick Nb will be necessary for 50% absorption of 6 keV x-rays, compared to 1.3 μm of Ta. Films thicker than ≈ 1.5 μm will require the development of nonstandard photolithographic processes -- perhaps not terribly difficult, but also not straightforward. Secondly, because of the quasiparticle losses associated with metallic Nb oxides, it does not appear that quasiparticle lifetimes or diffusion lengths will be long enough to support large area detectors. It is also for this reason that we have not considered the use of Nb absorber – Ta trap device designs.

Twerenbold's device works surprisingly well, considering it does not make use of any quasiparticle trapping. From this results the main problem with the device -- it most likely cannot be scaled up to the volumes necessary for x-ray astronomy. This device also shows a problem common to every device but ours and Kraus *et al.*'s: significant quasiparticle charge collected for x-ray absorptions in the films on either side of the tunnel junction. (Note that the signal will be the same polarity for absorpton on either side.) Because the devices cannot be made perfectly symmetric, this will lead to multiple (or, broadened) peaks in the pulseheight histogram for monoenergetic x-ray illumination. For such devices to be useful, one must mask off one of the films, or make the devices so dramatically antisymmetric that signals from one of the films can be neglected. This is relatively straightforward with lateral quasiparticle trapping, as used in our devices, and in Kraus *et al.*'s devices.

Based on this review of work in the field at present, we feel that for other worker's devices to be useful for x-ray astronomy, they must be significantly redesigned to eliminate the deficiencies highlighted in Table 9.1. We believe that our devices will require comparatively few design changes to be truly useful for x-ray astronomy. Of course, extensive testing of our device design will be necessary before we can firmly support this statement.

9.2 Suggestions for Future Work

Perhaps the least well understood aspect of our devices is the nature of quasiparticle trapping. Experimental tests must be performed to understand each of the processes involved. Such tests might include:

- quasiparticle diffusion in Ta and Al
- tests of short and long traps in devices from the same wafer
- tests with varied Ta absorber and Al trap volumes
- detection of substrate events (only)

• double junction experiments.

The quasiparticle diffusion properties in films can be studied in structures similar to those of Hsieh and Levine [68], where multiple tunnel junctions are distributed along a strip of the test film. Quasiparticle injection at one of the junctions with detection at another will allow determination of the quasiparticle diffusion length. It will be useful to perform this test with various quasiparticle injection energies to determine the effects of the quasiparticle dispersion curve on the quasiparticle velocity. Tests of long and short traps on very similar devices, combined with tests of varied absorber/trap volume ratios, might allow us to separate the effects of quasiparticle diffusion from interface reflection in determining the trapping time. Detection of substrate events with the device films masked from the x-ray source might give two characteristic signals: those in which phonons are primarily absorbed in the Ta, and those in which phonons are primarily absorbed in the Al trap. Differences in the characteristic times of the two signal groups should be primarily a result of the trapping process, and would thus give us another look at the nature of quasiparticle trapping in our devices. It will also be beneficial to test devices with Kraus *et al.*'s [89a] double junction geometry, from which we can learn a good deal about quasiparticle diffusion and interface transparency. Also, ion beam cleaning must be explored in detail to ensure maximal interface transparency.

The origin of the high energy "tail" in our pulseheight histograms needs to be determined, as this appears to generate a good deal of the broadening in energy resolution. One test which is relatively straightforward with our existing mask set involves thorough oxidation of the Ta surface before the trap deposition. As no quasiparticles will penetrate this oxide, we will only detect the signal from phonons entering the trap. This can tell us if the high energy tail is from phonons. If phonons are not found to be the cause, then the high energy tail in our present devices may be due to high energy Ta quasiparticles which have entered the trap. In any case, it appears that a more effective method of trap masking will be necessary in the very near future. It will be helpful to mask the Nb contact as well.

To control the effect of substrate absorptions, improvements in x-ray masking will prove useful. Thicker Ta absorbers will reduce the number of x-ray absorptions directly under the device. Also, micromachined substrates should be explored as potentially necessary to eliminate any of the low energy background counts from substrate events.

Changes in the device interaction with the electronic biasing and amplification should give the most improvement for the least amount of effort. Higher junction dynamic resistances (for a given tunnel time) will reduce the energy resolution broadening due to premature charge pulse decay. This might require modified junction shapes to reduce the influence of Fiske modes, lower impedance DC bias sources, or slightly different junction processing techniques. It would also be nice for space applications if we could eliminate the magnetic field coils in favor of "control lines."[Matisoo, 80] Such thin film wiring would run above (or below) the tunnel junction, separated from the junction by an insulating film. Current passed through these control lines would apply a local magnetic field to the junction, and give a potentially more compact device, or easier tuning of the field for individual devices in an array.

Improving the amplifier will also give much improved results for relatively small amounts of work. A larger open loop gain will allow longer electronic decay times, and smaller variation in pulseheight with risetime. The amplifier can also be modified to look at the current pulse and the integrated charge pulse simultaneously, thus giving us a better diagnostic test for evaluating the junction response.

With improved electronics and a better understanding of quasiparticle trapping, we believe our devices will fulfill the needs of x-ray astronomers in the very near future. It appears that the work before us is a refinement, rather than a redesign, of the devices characterized in this thesis. The thrill of actually observing single photons in one of our devices makes it all worthwhile.

Appendix 1: Device Fabrication Procedure

A1.1 Wafer Preparation

1) Clean 2" diameter Si <100> wafer ($\rho < 1$ Ω-cm)
   a) Trichloroethane (TCA), ultrasonic, 30 seconds
   b) Acetone (ACE), ultrasonic, 30 seconds
   c) Methanol (Meth), ultrasonic, 30 seconds
2) Blow dry wafers in N_2
3) Oxidize wafers (wet oxidation) at ≈ 1000° C to obtain ≈ 3000 Å SiO_2

A1.2 Tantalum Absorber Deposition and Definition

1) Load sample in Lesker sputter system on a SiO-coated wafer holder, with a 3/64" thick, 2" diameter stainless steel disk on the back of the wafer.
2) Pre-bake the wafer and chamber at 350° C for at least 6 hours; base pressure less than 1.5×10^{-7} torr at 350° C before deposition.

Ion Beam Cleaning Procedure

3) Ion beam clean the wafer (2 cm Kaufman ion source), with the following parameters: argon 1.5 sccm, ≈ 3×10^{-5} torr; cathode = 6 A; discharge = 35 V, 0.45 A; beam = 500 V, 4.7 mA; accelerator = 35 V, 0.7 mA; neutralizer = 3.8 A; Ar^+ current = 400 μA/cm^2; exposure time = 1.5 minutes.

---

4) Heat wafer and stainless steel disk to 675° C while presputtering Ta target (takes approximately 5 minutes)
5) Sputter Ta to desired thickness from 2" torus-2 dc magnetron sputter gun (with high-field magnet). Parameters: argon = 6 mtorr, 175 sccm (conductance controller set at 1.5); 960 W, 3A, 320 V; 38 Å/s. Source to sample distance is approximately 3 inches.
6) Cool sample at least 2 hours in vacuum, to < 30° C; remove sample.

Photoresist Patterning Procedure – Positive Photoresist

7) Spin Shipley 1400-27 photoresist at 4000 rpm for 45 seconds, giving a thickness of ≈ 1.3 μm.

8) Bake at 90° C for 3 minutes on hotplate.

9) Expose absorber pattern for 5 seconds in HTG contact mask aligner.

10) Develop ≈ 60 seconds in 3:1 Shipley Microposit Developer (endpoint determined by inspection).

11) Rinse ≈ 60 seconds in deionized water (DI).

---

12) Bake at 110° C for 10 minutes on hotplate.

13) Etch ≈ 2 minutes in 3:1 Kepro etch solution ($FeCl_3$, HCl) : HF (endpoint determined by inspection).

14) Rinse ≈ 2 minutes in DI.

15) Strip photoresist in ACE, Meth, and DI. Spin dry. Bake on 90° C hotplate for 30 seconds.

A1.3 Niobium Contact Deposition and Definition

Photoresist Patterning Procedure – Negative Photoresist

1) Spin Hoechst-Celanese 5218E photoresist at 3500 rpm for 45 seconds, giving a thickness of ≈ 1.5 µm.

2) Bake at 90° C for 3 minutes on hotplate.

3) Expose niobium contact pattern (image reversed) for 4 seconds in HTG contact mask aligner.

4) Bake at exactly 110° C for 2.5 minutes on hotplate.

5) Blanket expose the wafer for 60 seconds in HTG aligner.

6) Develop ≈ 60 seconds in 3:1 Shipley Microposit Developer (endpoint determined by inspection).

7) Rinse ≈ 60 seconds in DI.

---

8) Load sample in Lesker sputter system on a stainless wafer holder, with a 3/64" thick, 2" diameter copper disk on the back of the wafer. Base pressure should be less than 1.5×10^{-7} torr before the deposition.

9) Presputter the niobium target for at least 3 minutes.

10) Ion beam clean the wafer as above.

11) Sputter Nb to desired thickness from 2" torus-2 dc magnetron sputter gun

(with normal strength magnet). Parameters: argon = 11 mtorr, 150 sccm (conductance controller set at 4.0); 330 W, 1A, 330 V; 10 Å/s. Source to sample distance is approximately 3 inches. The Nb thickness should be kept below 2500 Å to reduce the probability of photoresist cracking or peeling during the sputter deposition.

12) Immediately remove sample from vacuum chamber, and soak in ACE for 1 to 2 hours to gently remove the niobium-coated photoresist.

13) Complete liftoff with ACE squirt, or ultrasonic ACE ($\approx$ 15 seconds), if necessary. Rinse in Meth and DI. Spin dry. Bake on 90° C hotplate for 30 seconds.

A1.4 Aluminum Trilayer Deposition

1) Load sample in Lesker sputter system on a stainless wafer holder, with a 3/64" thick, 2" diameter copper disk on the back of the wafer. Base pressure should be less than 1.5×10^{-7} torr before the deposition.
2) Premelt aluminum evaporation filaments, tune the deposition rate during the ion beam clean.
3) Ion beam clean the wafer as above.
4) Within 1 second, begin deposition of aluminum (in the argon background), at a rate of $\approx$ 200 Å/s (as desired for junction current density) to desired thickness for the trap layer.
5) Cool the ion gun and aluminum filaments for 3 to 5 minutes.
6) Isolate the vacuum chamber and sample from all pumps.
7) Bleed in pure oxygen to a pressure of $\approx$ 500 mtorr (as desired) in $\approx$ 1 min.
8) Oxidize at nominally room temperature for $\approx$ 2 hours (as desired).
9) Open cryopumps directly to the chamber, pump on the chamber for $\approx$ 5 minutes, until the base pressure is below 2×10^{-6} torr.
10) Warm up a new set of aluminum evaporation filaments; evaporate the counterelectrode at 20 Å/s to the desired thickness. Immediately remove sample from vacuum chamber.

A1.5 Aluminum Trilayer Patterning

1) Develop junction pattern in positive resist as above.
2) Dektak a certain region of photoresist to determine the exact thickness.

3) Etch for ≈ 3 minutes (at ≈ 300 Å/min) in 8:4:1:1 Phosphoric Acid: Acetic Acid: Nitric Acid: Water. This etch should be tested with the Dektak to make sure the tunnel barrier has been etched through.
4) Strip photoresist in ACE, Meth, and DI. Spin dry. Bake on 90° C hotplate for ≈ 1 minute.
5) Develop trap pattern in positive photoresist as above.
6) Etch for ≈ 1 minute in the same aluminum etch, but warm (≈ 40° C). Endpoint determined by inspection.
7) Strip photoresist in ACE, Meth, and DI. Spin dry. Bake on 90° C hotplate for ≈ 1 minute.

A1.6 SiO Deposition and Patterning

1) Develop SiO pattern in negative resist as above.
2) Load sample in Lesker sputter system on a stainless wafer holder, with a 3/64" thick, 2" diameter copper disk on the back of the wafer. This disk should be fastened to the wafer with vacuum grease. The base pressure should be less than 3 x 10^{-7} torr before the deposition.
3) Preheat the special SiO evaporation boat (R.D. Mathis model SO-10), and evaporate at ≈ 15 Å/s to the desired thickness (1500 Å gives a pinhole-free insulating film).
4) Immediately remove the sample from the vacuum chamber, and place in TCA. Soak for 1 to 2 hours to remove the vacuum grease, using a cotton swab to scrub if necessary.
5) Soak the sample in ACE for at least 1 hour to remove the SiO-coated photoresist. Follow with 15 seconds of ultrasonic to ensure liftoff of junction via regions. Verify liftoff with microscope.
6) Rinse sample in Meth and DI. Spin dry. Bake on 90° C hotplate for ≈ 1 minute.

A1.7 Aluminum Wiring Deposition and Patterning

1) Develop aluminum wiring pattern in negative resist as above.
2) Load sample in Lesker sputter system on a stainless wafer holder, with

a 3/64" thick, 2" diameter copper disk on the back of the wafer. This disk should be fastened to the wafer with vacuum grease. The base pressure should be less than 1.5 x 10^{-7} torr before the deposition.

3) Preheat fresh aluminum evaporation filaments (Tungsten coil filaments, R.D. Mathis model F5-3x.030W).
4) Ion beam clean the sample as above.
5) Within 1 second, evaporate aluminum at ≈ 30 Å/s to the desired thickness.
6) Immediately remove the sample from the vacuum chamber, and place in TCA. Soak for 1 to 2 hours to remove the vacuum grease, using a cotton swab to scrub if necessary.
7) Soak the sample in ACE for at least 1 hour to remove the Al-coated photoresist. Follow with ACE squirt (from plastic bottle) or ultrasonic to ensure liftoff.
8) Rinse sample in Meth and DI. Spin dry. Bake on 90° C hotplate for ≈ 1 minute.

Appendix 2: Summary of Device Characteristics

In this appendix, we tabulate the various relevant device characteristics for the devices which were used to generate data for this thesis.

A2.1 X-C93

Junction Shape: Stretched quartic
- L: ≈ 200 μm
- A: ≈ 1800 μm^2

Current Density: ≈ 50 A/cm^2

R_{nn}: ≈ 0.3 Ω

Tunnel Time: ≤ 8 μsec (for full trap volume)

Est. Trapping Time: ≈ 100 nsec (extended trap), ≈ 1.5 μsec (short trap)

Max R_{dyn} @ 0.3 K: ≈ 800 Ω

Fiske Modes: 90 μV, 120 μV

Fabrication:
- Ta Absorber: ≈ 4000 Å (5/27/93); volume ≈ 8000 μm^3
- Al Trap: ≈ 2000 Å @ ≈ 200 Å/sec (5/28/93)
  volume ≈ 4500 μm^3
  * overlaps entire Ta absorber (100 μm x 200 μm)
- Barrier: ≈ 450 mtorr O_2 for 2 hours
- Al C.E.: ≈ 650 Å @ ≈ 30 Å/sec
- Nb Contact: ≈ 800 Å
- SiO Via: ≈ 1000 Å @ ≈ 20 Å/sec
- Al Wiring: ≈ 3000 Å @ ≈ 12 Å/sec, sputtered

X-Ray Response:
- Peak: ≈ 1.8 x 10^6 electrons collected
- Risetime: peak at ≈ 8 μsec; significant contribution to ≈ 18 μsec

A2.2 X-N93

Junction Shape:	Stretched quartic
L:	≈ 200 μm
A:	≈ 1800 μm^2
Current Density:	≈ 25 A/cm^2
R_{nn}:	≈ 0.6 Ω
Tunnel Time:	≈ 3 μsec
Est. Trapping Time:	≈ 2 μsec
Max R_{dyn} @ 0.3 K:	≈ 1000 Ω
Fiske Modes:	90 μV
Fabrication:	
Ta Absorber:	≈ 6000 Å (12/8/93); volume ≈ 12,000 μm^3
Nb Contact:	≈ 2000 Å
Al Trap:	≈ 1500 Å @ ≈ 185 Å/sec (12/9/93)
	volume ≈ 850 μm^3
	* small Ta absorber overlap (10 μm x 100 μm)
Barrier:	≈ 600 mtorr O_2 for 3 hours
Al C.E.:	≈ 700 Å @ ≈ 15 Å/sec
SiO Via:	≈ 1500 Å @ ≈ 14 Å/sec
Al Wiring:	≈ 3000 Å @ ≈ 40 Å/sec
X-Ray Response:	
Peak:	≈ 5.7 x 10^6 electrons collected
Risetime:	peak at ≈ 16.5 μsec; significant contrib. to ≈ 8 μsec

A2.3 X-D94

Junction Shape:	Stretched quartic
L:	≈ 100 μm
A:	≈ 580 μm^2
Current Density:	≈ 30 A/cm^2
R_{nn}:	≈ 1.6 Ω
Tunnel Time:	≈ 5 μsec
Est. Trapping Time:	≈ 4 μsec
Max R_{dyn} @ 0.3 K:	≈ 9 kΩ
Fiske Modes:	120 μV
Fabrication:	
Ta Absorber:	≈ 8000 Å (3/7/94); volume ≈ 16,000 μm^3
Nb Contact:	≈ 1500 Å
Al Trap:	≈ 2000 Å @ ≈ 220 Å/sec (12/9/93)
	volume ≈ 500 μm^3
	* small Ta absorber overlap (5 μm x 100 μm)
Barrier:	≈ 500 mtorr O_2 for 2 hours
Al C.E.:	≈ 800 Å @ ≈ 14 Å/sec
SiO Via:	≈ 1500 Å @ ≈ 17 Å/sec
Al Wiring:	≈ 6000 Å @ ≈ 30 Å/sec
X-Ray Response:	
Peak:	≈ 1 x 10^6 electrons collected
Risetime:	peak at ≈ 16.5 μsec

References

Allessandrello, A., *et al.*, "High Z Bolometers for Analysis of Internal β and α Activities,"*J. Low Temp. Phys.* **93**, 815 (1993).

Ashcroft, N.W., and Mermin, N.D., Solid State Physics, Philadelphia: Saunders College, 1976.

Bardeen, J., Cooper, L.N., and Schrieffer, "Theory of Superconductivity," *Phys. Rev.* **108**, 1175 (1957).

Barone, A., and Paterno, G., Physics and Applications of the Josephson Effect, New York: Wiley and Sons, 1982.

Barone, A., ed., Superconductive Particle Detectors, New Jersey: World Scientific, 1988.

Barone, A., Cristiano, R., and Pagano, S., X-Ray Detection by Superconducting Tunnel Junctions, New Jersey: World Scientifiec, 1991.

Bhushan, M., and Macedo, E.M., "Nb/AlOx/Nb Trilayer Process for the Fabrication of Submicron Josephson Junctions and Low-Noise DC SQUIDs," *Appl. Phys. Lett.* **58**, 1323 (1991).

Booth, N.E., "Quasiparticle Trapping and the Quasiparticle Multiplier," *Appl. Phys. Lett.* **50**, 293 (1987).

Booth, N.E., "Solar Neutrinos with an Indium Detector," p. 69 in G. Waysand And G. Chardin, eds., Superconducting and Low Temperature Particle Detectors, New York: Elsevier Science Publishers, 1989.

Booth, N.E., *et al.*, "Single Crystal Superconductors as X-Ray Detectors," p. 125 in A. Barone, R. Cristiano, and S. Pagano, eds., X-Ray Detection by Superconducting Tunnel Junctions, New Jersey: World Scientific, 1991.

Booth, N.E., and Salmon, G.L., Low Temperature Detectors for Neutrinos and Dark Matter IV, Gif-sur-Yvette Cedex, France: Editions Frontieres, 1992.

Brennan, S., *et al.*, "A Suite of Programs for Calculating X-Ray Absorption, Reflection, and Diffraction Performance for a Variety of Materials at Arbitrary Wavelengths,"*Rev. Sci. Inst.* **63**, 850 (1992). Also, C.K. Stahle, personal communication, 1994.

Brogiato, L., Camin, D.V., and Fiorini, E., Low Temperature Detectors for Neutrinos and Dark Matter III, Gif-sur-Yvette Cedex, France: Editions Frontieres, 1990.

Buckner, S.A., Chen, J.T., and Langenberg, D.N., "Current-Voltage Characteristics of Small Josephson Tunnel Junctions," *Phys. Rev. Lett.* **25**, 738 (1970).

DeGennes, P.G., "Boundary Effects in Superconductors," *Rev. Mod. Phys.* **36**, 225 (1964).

de Korte, P.A.J., *et al.*, "Superconductive Tunneljunctions for X-Ray Spectroscopy,"*Proc. SPIE* **1743**, 24 (1992).

de Korte, P.A.J., "Superconductive X-Ray Photon Detectors," Proc. ESA Symposium on Photon Detectors for Space Instrumentation, ESTEC, Noordwijk, the Netherlands, Nov., 1992, ESA SP-356, 41 (1992b).

de Korte, P.A.J., personal communication, April, 1994.

Dietsche, W., and Kinder, H., "Inelastic Phonon Scattering in Glass," p. 37 in Phonon Scattering in Condensed Matter, ed. H.J. Maris, New York: Plenum Press, 1980.

Eck, R.E., Scalapino, D.J., and Taylor, B.N., "Tunnel Junction RF Modes Driven by the AC Josephson Current," in *Proc. 9th Intl. Conf. on Low Temp. Phys.*, ed. J.G. Daunt (New York: Plenum), 415 (1965).

Eisenmenger, W., "Nonequilibrium Phonons," Chapter 3 in K.E. Gray, ed., Nonequilibrium Superconductivity, Phonons, and Kapitza Boundaries, New York: Plenum Press, 1981.

Face, D.W., Ruggiero, S.T., and Prober, D.E., "Ion-Beam Deposition of Nb and Ta Refractory Superconducting Films," *J. Vac. Sci. Tech. A* **1**, 326 (1983).

Face, D.W., and Prober, D.E., "Nucleation of Body-Centered-Cubic Tantalum Films with a Thin Niobium Underlayer," *J. Vac. Sci. Tech. A* **5**, 3408 (1987).

Face, D.W., and Prober, D.E., "Fabrication and DC Characteristics of Small-Area Tantalum and Niobium Superconducting Tunnel Junctions," *J. Appl. Phys.* **62**, 3257 (1987).

Fairstein, E., and Hahn, J., "Nuclear Pulse Amplifiers – Fundamentals and Design Practice (Part 3)," *Nucleonics* **23**, 50 (1965).

Fano, U., "Ionization Yield of Radiations. II. The Fluctuations of the Number of Ions," *Phys. Rev.* **72**, 26 (1947).

Feautrier, P., Hanus, M., and Febvre, P., "Nb/Al-AlOx/Nb Junctions for a 380 GHz SIS Receiver," *Supercond. Sci. Tech.* **5**, 564 (1992).

Feinstein, L.G., and Hutteman, R.D., "Factors Controlling the Structure of Sputtered Ta Films," *Thin Solid Films* **16**, 129 (1973).

Fiorini, E., "Cryogenic Thermal Detectors in Subnuclear Physics and Astrophysics," *Physica B* **169**, 388 (1991).

Fiske, M.D., "Temperature and Magnetic Field Dependences of the Josephson Tunneling Current," *Rev. Mod. Phys.* **36**, 221 (1964).

Frederiksen, T.M., Intuitive Operational Amplifiers, New York: McGraw Hill, 1988.

Fulton, T.A., "Externally Shunted Josephson Junctions," *Phys. Rev. B* **7**, 1189 (1973).

Fulton, T.A., *et al.*, "Tunneling Between Thin Film Superconductors Containing Single Flux Vortices," *Sol. State Comm.* **22**, 493 (1977).

Gaidis, J.M., personal communication, 1994.

Gaidis, M.C., *et al.*, "Superconducting Al-Trilayer Tunnel Junctions for use as X-Ray Detectors," *IEEE Trans. Appl. Superconductivity* **3**, 2088 (1993).

Gaitskell, R.J., "Non-Equilibrium Superconductivity in Niobium and its Application to Particle Detection," Ph.D. Thesis, Univ. of Oxford, Dept. of Physics, 1993.

Gatti, E., and Manfredi, P.F., "Present Trends and Realisations in Readout Electronics for Semiconductor Detectors in High Energy Physics," *Nucl. Inst. Meth.* **226**, 142 (1984).

Gilabert, A., "Effet de Proximite entre un Metal Normal et un Supraconducteur," *Ann. Phys.* **2**, 203 (1977).

Goldie, D., *et al.*, "The Statistical Noise due to Tunneling in Superconducting Tunnel Junction Detectors," to be published in *Appl. Phys. Lett.*, June 1994.

Golubov, A.A., and Kupriyanov, M.Yu., "Theoretical Investigation of Josephson Tunnel Junctions with Spatially Inhomogeneous Superconducting Electrodes," *J. Low Temp. Phys.* **70**, 83 (1988).

Golubov, A.A., and Kupriyanov, M.Yu., "Josephson Effect in SNINS and SNIS Tunnel Structures wiht Finite Transparency of the SN Boundaries," *Sov. Phys. JETP* **69**, 805 (1989).

Gray, K.E., "Steady State Measurements of the Quasiparticle Lifetime in Superconducting Aluminum," *J. Phys. F: Metal Phys.* **1**, 290 (1971).

Gray, K.E., "A Superconducting Transistor," *Appl. Phys. Lett.* **32**, 392 (1978a).

Gray, K.E., and Willemsen, H.W., "Inhomogeneous State of Superconductors by Intense Tunnel Injection of Quasiparticles," *J. Low Temp. Phys.* **31**, 911 (1978b).

Gray, K.E., "Tunneling: A Probe of Nonequilibrium Superconductivity," Chapter 5 in K.E. Gray, ed., Nonequilibrium Superconductivity, Phonons, and Kapitza Boundaries, New York: Plenum Press, 1981.

Gray, K.E., "Nonequilibrium Superconductivity for Particle Detectors," p. 1 in A. Barone, ed., Superconductive Particle Detectors, New Jersey: World Scientific, 1988.

Gubankov, V.N., *et al.*, "Influence of Trapped Abrikosov Vortices on the Critical Current of the Josephson Tunnel Junction," *Supercond. Sci. Tech.* **5**, 168 (1992).

Haghiri-Gosnet, A.M., *et al.*, "Stress and Microstructure in Tungsten Sputtered Thin Films," *J. Vac. Sci. Tech. A* **7**, 2663 (1989).

Halbritter, J., "On the Oxidation and on the Superconductivity of Niobium," *Appl. Phys. A* **43**, 1 (1987).

Hebrank, F., *et al.*, "Spatial and Temporal Dynamics of Superconducting Nb/AlOx/ Nb Tunnel Junction Detectors," *IEEE Trans. Appl. Superconductivity* **3**, 2084 (1993).

Hieber, K., and Mayer, N.M., "Structural Changes of Evaporated Tantalum During Film Growth," *Thin Solid Films* **90**, 43 (1982).

Holdik, K., Welte, M., and Eisenmenger, W., "Quasiparticle Recombination Time of Superconducting Tin Films in a Parallel Magnetic Field," *J. Low Temp. Phys.* **58**, 379 (1985).

Houwman, E.P., *et al.*, "Fabrication and Properties of Nb/Al, Alox/Nb Josephson Tunnel Junctions with a Double Oxide Barrier," *J. Appl. Phys.* **67**, 1992 (1990).

Houwman, E.P., *et al.*, "On the Suppression of the Sidelobes of the Supercurrent in Small Josephson Tunnel Junctions," *Physica C* **183**, 339 (1991).

Hsieh, S.Y., and Levine, J.L., "Diffusion of Quasiparticles in Superconducting Aluminum Films," *Phys. Rev. Lett.* **20**, 1502 (1968).

Hu, P., *et al.*, "Quasiparticle Propagation and Recombination in Bulk, Superconducting Pb," *Phys. Rev. Lett.* **38**, 361 (1977).

Jochum, J., *et al.*, "Dynamics of Radiation Induced Quasiparticles in Superconducting Tunnel Junction Detectors," *Ann. Physik* **2**, 611 (1993).

Johnson, W.J., and Barone, A., "Effect of Junction Geometry on Maximum Zero-Voltage Josephson Current," *J. Appl. Phys.*, **41**, 2958 (1970).

Kaplan, S.B., *et al.*, "Quasiparticle and Phonon Lifetimes in Superconductors," *Phys. Rev. B* **14**, 4854 (1976).

Kaplan, S.B., "Acoustic Matching of Superconducting Films to Substrates," *J. Low Temp. Phys.* **37**, 343 (1979).

Klein, C., "Semiconductor Particle Detectors: A Reassessment of the Fano Factor Situation," *IEEE Trans. Nucl. Sci.* **15**, 214 (1968).

Knoll, G.F., Radiation Detection and Measurement, New York: J. Wiley & Sons, 1989.

Kondo, I., *et al.*, "Interface Structure and Adhesion of Sputtered Metal Films on Silicon: The Influence of Si Surface Condition," *J. Vac. Sci. Tech. A* **11**, 319 (1993).

Kraus, H., *et al.*, "Quasiparticle Trapping in a Superconductive Detector System Exhibiting High Energy and Position Resolution," *Phys. Lett. B* **231**, 195 (1989a).

Kraus, H. "Quasiteilchen-Einfang in Supraleitenden Tunneldioden," Ph.D. Thesis, Technischen Universitat Munchen, 1989b.

Kraus, H. "Superconducting Tunnel Junctions," presentation given at Yale Univ., summer 1991.

Kraus, H. "X-Ray Detection with Superconducting Tunnel Junctions," presentation given at Yale Univ., summer 1993.

Kraus, H., Lecture given at the Workshop on Superconducting Particle Detectors, Toledo, Spain, April 1994. Proceedings to be published by World Scientific.

Kurakado, M., "Possibility of High Resolution Detectors Using Superconducting Tunnel Junctions," *Nucl. Inst. Meth.* **196**, 275 (1982).

Kurakado, M., "Developments in Superconducting Tunnel Junction Detectors," *Nucl. Inst. Meth.* **A314**, 252 (1992).

Kurakado, M., *et al.*, "X-Ray Detection wih a Nb-Based Junction and Investigation of Series-Junction Detectors," *Proc. SPIE* **1743**, (1992b).

Labov, S., and Young, B.A., *Proc. 5th Intl. Workshop on Low Temp. Detectors,* in *J. Low Temp. Phys.* **93**, Nos. 3/4, 185 (1993).

Laegreid, N., and Wehner, G.K., "Sputtering Yields of Metals for Ar+ and Ne+ Ions with Energies from 50 to 600 eV," *J. Appl. Phys.* **32**, 365 (1961).

Larrea, A., *et al.*, "On Superconducting Superheated Granules (SSG) Devices as Double Beta Decay Detectors," p. 161 in G. Waysand And G. Chardin, eds., Superconducting and Low Temperature Particle Detectors, New York: Elsevier Science Publishers, 1989.

le Grand, J.B., *et al.*, "Superconductive Junctions with Trappinglayers for the Detection of X-rays," *J. Low Temp. Phys.* **93**, 573 (1993).

le Grand, J.B., *et al.*, "X-Ray Response of Superconducting Nb/Al and Nb/Ta Tunneljunctions," Presented at conference on Superconducting Particle Detectors, Toledo, Spain, 1994.

Lemke, S., *et al.*, "Superconducting Nb/AlOx/Nb Tunnel Junctions on Micromachined Silicon Substrates," *J. Low Temp. Phys.* **93**, 617 (1993).

Lesyna, L., *et al.*, "Advanced X-Ray Detectors for the Analysis of Materials," *J. Low Temp. Phys.* **93**, 779 (1993).

Long, A.R., "The Attenuation of High Frequency Phonons in Metals," *J. Phys. F: Metal Phys.* **3**, 2023 (1973).

Manfredi, P.F., and Ragusa, F., "Low Noise Electronics in Elementary Particle Physics," *Nucl. Inst. Meth.* **A235**, 345 (1985).

Matisoo, J., "Josephson-Type Superconductive Tunnel Junctions and Applications," *IEEE Trans. Mag.* **5**, 848 (1969).

Matisoo, J., "Overview of Josephson Technology Logic and Memory," *IBM J. Res. Dev.* **24**, 113 (1980).

Mattox, D.P., IP Industries, personal communication, December, 1992.

Mayer, B., *et al.*, "Imaging of One- and Two-Dimensional Fiske Modes in Josephson Tunnel Junctions," *Phys. Rev. B* **44**, 12463 (1991).

McCammon, D., *et al.*, "Thermal Detection of X-Rays," p. 213 in L. Brogiato *et al.*, ed., Low Temperature Detectors for Neutrinos and Dark Matter III, Gif-sur-Yvette Cedex, France: Editions Frontieres, 1990.

McMillan, W.L., "Theory of Superconductor-Normal-Metal Interfaces," *Phys. Rev.* **175**, 559 (1968), and McMillan, W.L., "Tunneling Model of the Superconducting Proximity Effect," *Phys. Rev.* **175**, 537 (1968)

Mears, C.A., Labov, S.E., and Barfknecht, A.T., "Energy-Resolving Superconducting X-Ray Detectors with Charge Amplification due to Multiple Quasiparticle Tunneling," *Appl. Phys. Lett.* **63**, 2961 (1993). also, Mears, C.A., Labov, S.E., and Barfknecht, A.T., "High Resolution Superconducting X-Ray Detectors with Two Aluminum Trapping Layers," *J. Low Temp. Phys.* **93**, 561 (1993).

Meier, D.L., Przybysz, J.X., and Kang, J., "Fabrication of an All-Refractory Circuit Using Lift-Off with Image-Reversal Photoresist," *IEEE Trans. Mag.* **27**, 3121 (1991).

Miller, S.L., *et al.*, "Critical Currents of Cross-Type Superconducting-Normal-Superconducting Junctions in Perpendicular Magnetic Fields," *Phys. Rev. B* **31**, 2684 (1985).

Moseley, S.H., *et al.*, "Advances Toward High Spectral Resolution Quantum X-Ray Calorimetry," *IEEE Trans. Nucl. Sci.* **35**, 59 (1988).

Nahum, M., Martinis, J.M., and Castles, S., "Hot-Electron Microcalorimeters for X-Ray and Phonon Detection," *J. Low Temp. Phys.* **93**, 733 (1993).

Narayanamurti, V. *et al.*, "Quasiparticle and Phonon Propagation in Bulk, Superconducting Lead," *Phys. Rev. B* **18**, 6041 (1978).

Nerenberg, M.A.H., Forsyth, P.A., Jr., and Blackburn, J.A., "Excitation of Cavity Modes in Rectangular Josephson Junctions," *J. Appl. Phys.* **47**, 4148 (1976).

Parker, W.H., "Modified Heating Theory of Nonequilibrium Superconductors," *Phys. Rev. B* **12**, 3667 (1975).

Peterreins, Th., *et al.*, "A New Detector of Nuclear Radiation Based on Ballistic Phonon Propagation in Single Crystals at Low Temperatures," *Phys. Lett. B* **202**, 161 (1988).

Peterson, R.L., "Sidelobe Suppression in Small Josephson Junctions," *Cryogenics* **31**, 132 (1991).

Powell, C., "Inconstant Cosmos," *Sci. Am.* **268**, 110 (May, 1993).

Probst, F., *et al.*, "Recent Developments in Detector Research," *Nucl. Inst. Meth.* **A280**, 251 (1989).

Przybysz, J.X., "Process Improvements for Fabrication of Josephson Shift Registers," *Extended Abstracts of the 1989 International Superconductivity Conference, Tokyo*, 267 (1989).

Rando, N., *et al.*, "The Properties of Niobium Superconducting Tunneling Junctions as X-Ray Detectors," *Nucl. Inst. Meth.* **A313**, 173 (1992).

Rando, N., *et al.*, "Highly Collimated Photon Detection Using Strongly Coupled Superconducting Tunnel Junctions," *IEEE Trans. Appl. Superconductivity* **3**, 2080 (1993).

Read, M.H., and Altman, C., "A New Structure in Tantalum Thin Films," *Appl. Phys. Lett.* **7**, 51 (1965).

Reed, T.B., Free Energy of Formation of Bianry Compounds, Ch. 8; Cambridge, MA: The MIT Press, 1971.

Rothwarf, A., and Taylor, B.N., "Measurement of Recombination Lifetimes in Superconductors," *Phys. Rev. Lett.* **19**, 27 (1967).

Santhanam, P., and Prober, D.E., "Inelastic Electron Scattering Mechanisms in Clean Aluminum Films," *Phys. Rev. B* **29**, 3733 (1984).

Sato, S., "Nucleation Properties of Magnetron-Sputtered Tantalum," *Thin Solid Films* **94**, 321 (1982).

Schoenlein, R.W., *et al.*, "Femtosecond Studies of Nonequilibrium Electronic Processes in Metals," *Phys. Rev. Lett.* **58**, 1680 (1987).

Seidel, W., *et al.*, "Munich Dark Matter Search," *J. Low Temp. Phys.* **93**, 797 (1993).

Shiota, T., Imamura, T., and Hasuo, S., "Fabrication of High Quality Nb/AlOx-Al/ Nb Josephson Junctions: III -- Annealing Stability of AlOx Tunneling Barriers," *IEEE Trans. Appl. Superconductivity* **2**, 222 (1992).

Stahle, C.K., "The Development of High Resolution Calorimetric X-Ray Detectors for Compton Scattering Experiments," Ph.D. Thesis, Stanford Univ., 1991.

Stahle, C.K., personal communication (1992).

Swihart, J.C., "Field Solution for a Thin-Film Superconducting Strip Transmission Line,"*J. Appl. Phys.* **32**, 461 (1961).

Thornton, J.A., "Influence of Substrate Temperature and Deposition Rate on Structure of Thick Sputtered Cu Coatings," *J. Vac. Sci. Tech.* **12**, 830 (1975).

Thornton, J.A., "The Microstructure of Sputter-Deposited Coatings," *J. Vac. Sci.*

Tech. A **4**, 3059 (1986).

Twerenbold, D., "Giaever-Type Superconducting Tunnelling Junctions as High-Resolution X-Ray Detectors," PhD Thesis, Swiss Fed. Inst. of Tech., 1986.

Twerenbold, D., "Nonequilibrium Model of the Superconducting Tunneling Junction X-Ray Detector," *Phys. Rev. B* **34**, 7748 (1986b).

Twerenbold, D., and Zehnder, A., "Superconducting Sn/Sn-Oxide/Sn Tunneling Junctions as High-Resolution X-Ray Detectors," *J. Appl. Phys.* **61**, 1 (1987).

Uchida, N., *et al.*, "Flux Trapping in Josephson Tunnel Junctions," *J. Appl. Phys.* **54**, 5287 (1983).

Van Duzer, T., and Turner, C.W., Principles of Superconductive Devices and Circuits, New York: Elsevier, 1981.

Van Vechten, D., and Wood, K.S., "Probability of Quasiparticle Self-Trapping due to Localized Energy Deposition in Nonequilibrium Tunnel-Junction Detectors," *Phys. Rev. B* **43**, 12852 (1991).

Videler, P., *et al.*, "Spatial Variations in the X-Ray Performance of High Quality Superconducting Tunnel Junctions," *J. Low Temp. Phys.* **93**, 587 (1993).

Warburton, P.A., and Blamire, M.G., "Quasiparticle Trapping in Distributed Three-Terminal Double Tunnel Devices," *IEEE Trans. Appl. Superconductivity* **3**, 2066 (1993).

Waysand, G., and Chardin, G., Superconducting and Low-Temperature Particle Detectors, New York: Elsevier, 1989.

Yin, G.Z., and Jillie, D.W., "Orthogonal Design for Process Optimization and its Application in Plasma Etching," *Sol. St. Tech.* **May**, 127 (1987).

Yoshihara, T., and Suzuki, K., "Variation of Internal Stresses in Sputtered Ta Films," *J. Vac. Sci. Tech. B* **11**, 301 (1993).

Young, B.A., Cabrera, B., and Lee, A.T., "Observation of Ballistic Phonons in Silicon Crystals Induced by α Particles," *Phys. Rev. Lett.* **64**, 2795 (1990).

Young, B.A., *et al.*, "Detection of Elementary Particles Using Silicon Crystal Acoustic Detectors with Titanium Transition Edge Phonon Sensors," *Nucl. Inst. Meth.* **A311**, 195 (1992).

Zacher, R.A., *et al.*, "Nb/Al/AlOx/Nb Superconducting Tunnel Junctions as X-ray Detectors," *J. Low Temp. Phys.* **93**, 581 (1993).

Zehnder, A., personal communication, April, 1994.